Titre: Title:	Towards the Development of a 3D ex Vivo Platform for the Evaluation of Micro-Damage, Strain Fields and Mechanical Properties in Trabecular Bone
Auteur: Author:	Rodrigue Caron
Date:	2022
Type:	Mémoire ou thèse / Dissertation or Thesis
Référence: Citation:	Caron, R. (2022). Towards the Development of a 3D ex Vivo Platform for the Evaluation of Micro-Damage, Strain Fields and Mechanical Properties in Trabecular Bone [Master's thesis, Polytechnique Montréal]. PolyPublie. https://publications.polymtl.ca/10382/

Document en libre accès dans PolyPublie
Open Access document in PolyPublie

URL de PolyPublie: PolyPublie URL:	https://publications.polymtl.ca/10382/
Directeurs de recherche: Advisors:	Isabelle Villemure, & Lama Séoud
Programme: Program:	Génie biomédical

POLYTECHNIQUE MONTRÉAL

affiliée à l'Université de Montréal

Towards the development of a 3D *ex vivo* platform for the evaluation of micro-damage, strain fields and mechanical properties in trabecular bone

RODRIGUE CARON

Institut de génie biomédical

Mémoire présenté en vue de l'obtention du diplôme de *Maîtrise ès sciences appliquées*

Génie biomédical

Juin 2022

POLYTECHNIQUE MONTRÉAL

affiliée à l'Université de Montréal

Ce mémoire intitulé :

Towards the development of a 3D *ex vivo* platform for the evaluation of micro-damage, strain fields and mechanical properties in trabecular bone

présenté par **Rodrigue CARON**

en vue de l'obtention du diplôme de *Maîtrise ès sciences appliquées*

a été dûment accepté par le jury d'examen constitué de :

Carl-Éric AUBIN, président

Isabelle VILEMURE, membre et directrice de recherche

Lama SÉOUD, membre et codirectrice de recherche

Farida CHERIET, membre

ACKNOWLEDGEMENTS

RÉSUMÉ

L'ostéoporose est une pathologie affectant la densité minérale osseuse. L'absence de symptômes fait en sorte que le diagnostic des patients est très difficile avant les stades avancés de la maladie. Des études visant à comprendre la biomécanique et le remodelage osseux sont ainsi développées pour mieux comprendre la maladie. Différentes approches sont utilisées pour mesurer les propriétés mécaniques des échantillons osseux et ce, dans des conditions *ex vivo* ou encore dans des conditions *in vivo*. Une de ces approches consiste en un chargement mécanique d'échantillons osseux combiné à des techniques d'imagerie médicale, comme le microCT, pour étudier les structures internes à un niveau microscopique. La quantité de microdommage accumulée et les patrons de déformation 3D peuvent par la suite être évalués à l'aide d'algorithmes à partir des images microCT. Ce projet présente deux études expérimentales présentant le développement d'une plateforme *ex vivo* pour étudier les propriétés d'échantillons d'os trabéculaire en 3D.

Une première étude a investigué le potentiel de l'apprentissage profond pour la segmentation des microdommages osseux dans l'os trabéculaire. Six cylindres d'os bovin trabéculaire ont subi une compression jusqu'à la contrainte ultime et ont ensuite été imagés avec un microCT à une résolution de 1,95 um. Deux de ces échantillons (échantillons 1 et 2) ont ensuite été colorés à l'aide d'un agent de contraste, le sulfate de baryum ($BaSO_4$), et imagés à nouveau. Les échantillons non colorés (échantillons 3 à 6) ont été utilisés pour entrainer deux réseaux de neurones, YOLOv4 pour détecter les régions présentant du microdommage à l'aide de boites englobantes, et Unet pour segmenter les pixels composant le microdommage dans les zones détectées. Quatre versions différentes de YOLOv4 ont été comparées à l'aide de la moyenne de l'intersection sur l'union (IoU) et de la moyenne de la précision moyenne (mAP). La performance de Unet a également été mesurée à l'aide de deux mesures de segmentation, le Dice Score et l'Intersection sur Union (IoU). Une comparaison qualitative a finalement été faite entre les approches d'apprentissage profond et d'agent de contraste.

Les résultats de cette première étude ont montré le potentiel et les limites d'utiliser l'apprentissage profond pour la segmentation du microdommage osseux. De toutes les versions de YOLOv4, YOLOv4p5 a obtenu les meilleurs résultats avec une IoU moyenne de 45,32 % et 51,12 % et un mAP de 28,79 % et 46,22 %, pour les échantillons 1 et 2 respectivement. Pour Unet appliqué avec les boîtes englobantes de référence, l'IoU et le DICE score ont respectivement atteint 50,11 % et

66,77 % pour l'échantillon 1 et 70,73 % et 82,85 % pour l'échantillon 2. Lorsque Unet a été appliqué avec les résultats YOLOv4p5, l'IoU et le DICE score ont respectivement indiqué 26,04 % et 41,34 % pour l'échantillon 1 et 58,21 % et 73,58 % pour l'échantillon 2. La performance plus basse de l'échantillon 1 peut s'expliquer à l'aide du ratio contraste bruit (CNR). En effet, l'échantillon 1 a montré un CNR plus bas (7,96) que l'échantillon 2 (10.08). Finalement, la comparaison qualitative entre l'agent de contraste et la segmentation par l'apprentissage profond du microdommage a montré que des régions différentes étaient segmentées par les deux techniques. L'apprentissage profond segmente la région à l'intérieur des fissures tandis que l'agent de contraste segmente la région l'entourant ou même les régions sans dommage visible.

Une deuxième étude a exploré la relation entre les patrons de déformation 3D mesurés par la corrélation de volume numérique (DVC) et les microfissures dans l'os trabéculaire. L'étude a également testé la segmentation du microdommage à l'aide du réseau de neurones de la première étude. Un échantillon d'os trabéculaire bovin a été déformé à une vitesse quasi-statique en plusieurs incréments à l'aide du système d'essais *in situ* Deben combiné au système microCT. L'échantillon a été déformé à 6 % puis à 10 % de déformation, ou jusqu'à ce que la courbe s'approche de la contrainte ultime (pente nulle). L'échantillon a été imagé à une résolution de 2,09 um avant le premier chargement et après chaque incrément de chargement. Ensuite, le réseau YOLOv4p5, entrainé dans la première étude, a été appliqué au volume imagé après la deuxième déformation. Après avoir appliqué le réseau de neurones, l'ensemble de données a été sous-échantillonné par un facteur de quatre pour être traité à l'aide d'un algorithme DVC.

La détection du microdommage à l'aide de l'apprentissage profond n'a pas donné de bons résultats. Cette faible performance pourrait être expliquée par le fait que les images de cette seconde étude avaient un CNR bien inférieur (1.8) comparé aux images de la première étude (7.96 à 10.08). La région de grande déformation mesurée par l'algorithme DVC a été colocalisée avec la région contenant plus de microdommage, selon l'axe des z (parallèle à l'axe de chargement). Cependant, pour les images analysées dans le plan XY , les résultats ne sont pas assez précis pour colocaliser avec confiance les régions de microdommage avec les régions de haute déformation.

Ce projet a permis de développer une procédure expérimentale *ex vivo* pour l'étude du microdommage dans l'os trabéculaire en 3D. Le projet démontre la possibilité d'utiliser la segmentation par apprentissage profond pour détecter et évaluer le microdommage dans un

échantillon d'os trabéculaire à l'aide d'images obtenues par un microCT à rayons X hautes résolutions. Même si le modèle d'apprentissage profond discuté dans cette étude n'apparait pas encore optimal, le développement d'un ensemble de données plus varié, combiné à des réseaux de neurones modifiés pour la détection de microfissures dans l'os trabéculaire, permettrait d'améliorer les résultats. De plus, la colocalisation entre les régions de microfissures et les régions de forte déformation le long de l'axe de chargement, mesuré à l'aide d'un algorithme DVC, a montré l'importance d'inclure la corrélation de volume numérique pour mieux comprendre le mécanisme de fracture. Ce projet ouvre des avenues pour de futurs travaux qui utiliseront ce système de test mécanique *in situ* combiné à un scanner microCT pour étudier simultanément les propriétés mécaniques, les patrons de déformation et le microdommages en 3D. Ces connaissances sont indispensables pour le développement de nouvelles techniques pour le diagnostic de pathologie osseuses, comme l'ostéoporose.

ABSTRACT

Osteoporosis is a pathology affecting bone mineral density. Lack of symptoms makes it hard to diagnose the patients before bone fracture. Studies aiming at understanding bone biomechanics and remodeling are developed to better understand the disease. Different approaches are used to measure the mechanical properties and behavior of bone samples. One of them consists of mechanical loading of bone samples combined with medical imaging techniques (Xray microCT) to investigate the internal structures at a microscopic level. Microdamage volume and strain patterns can be computed using post imaging algorithms. This project shows two experimental studies aimed to develop an *ex vivo* platform to study trabecular bone samples components in 3D.

A first study aimed to investigate the potential of deep learning for the segmentation of bone microdamage in trabecular bone. Six trabecular bovine bone cylinders underwent compression until ultimate stress and were subsequently imaged with a microCT at a resolution of 1.95 um. Two of these samples (samples 1 and 2) were then stained using barium sulfate ($BaSO_4$) and imaged again. The unstained samples (samples 3-6) were used to train two neural networks, YOLOv4 to detect regions with microdamage further combined with Unet to segment the microdamage at the pixel level in the detected regions. Four different versions of YOLOv4 model were compared using the average Intersection over Union (IoU) and the mean average precision (mAP). The performance of Unet was also measured using two segmentation metrics, the Dice Score and the Intersection over Union (IoU). A qualitative comparison was finally done between the deep learning and the contrast agent approaches.

Among the four versions of YOLOv4, the YOLOv4p5 model resulted in the best performance with an average IoU of 45,32% and 51,12% and a mAP of 28.79% and 46.22%, respectively for samples 1 and 2. The segmentation performance of Unet provided better IoU and DICE score on sample 2 compared to sample 1. The poorer performance of the test on sample 1 could be explained by its poorer contrast to noise ratio (CNR). Indeed, sample 1 resulted in a CNR of 7,96, which was worse than the average CNR in the training samples, while sample 2 resulted in a CNR of 10,08. The qualitative comparison between the contrast agent and the deep learning segmentation showed that different regions were segmented by the two techniques. Deep learning is segmenting the region inside the cracks while the contrast agent segments the region around it or even regions with no visible damage.

A second study investigated the relationship between 3D strain maps measured by digital volume correlation (DVC) and micro-cracks localization. The complementary study also tested the deep learning models for microcracks segmentation from the first study. One trabecular bone sample was extracted from a bovine tail vertebra. It was then deformed at a quasi-static rate in multiple increments using the Deben *in situ* testing system inside the microCT scanner. The sample was deformed at 6% and then 10% strain or until it approached the ultimate stress (zero slope). The sample was imaged at a resolution of 2.09 um before the first loading and after every loading increment. Afterwards, the YOLOv4p5 neural network, which was trained in the first study, was applied to the volume imaged after the second deformation. The dataset was then downsampled by a factor of four to process with a DVC algorithm.

In this second study, the detection of microdamage using deep learning did not provide good results. This could be explained by the dataset having a CNR much lower (1.8) than the CNR of the dataset used in the first study to train the neural network (range from 7.96 to 10.08). This strengthened the result from the first study, where training images should be diversified during training to avoid overfitting. Regions of high displacements measured by the DVC algorithm were correlated to regions of damage along the z-axis (parallel to the loading axis). However, for images in the XY plane, visualization was not precise enough to colocalize microdamage with regions of high strain.

This project allowed to develop an *ex vivo* experimental procedure for the evaluation of micro-damage in 3D in trabecular bone. It showed the feasibility of using deep learning segmentation to detect and segment microdamage in trabecular bone samples using high-resolution Xray microCT images. Even though the deep learning model discussed in this work was not optimal, the development of a more diverse dataset with improvement in the current neural networks could make it more performant and relevant for future work. Also, correlation between region of microcracks and region of high strain along the loading axis, using DVC and an *in situ* compression system, showed the importance of including DVC to have a better understanding of fracture mechanics. This project opens avenues for future future studies using the *in situ* Deben system inside the microCT scanner to simultaneously study mechanical properties, D strain patterns, and microdamage in 3D. This knowledge is essential for the development of new diagnosis techniques for bone pathologies, such as osteoporosis.

TABLE OF CONTENTS

LIST OF TABLES

LIST OF FIGURES

Figure 2-13: Biological neuron (left): the dendrite receiving several input signals and the cell body processing the signal. If the sum of the inputs reaches the threshold, the cell body sends an action potential through the axon towards the synapses [126]. Artificial neuron (right): several inputs x_i

LIST OF SYMBOLS AND ABBREVIATIONS

ANN	artificial neural network
AP	Average precision
BB	Bounding box
CNR	Contrast to noise ratio
CNN	Convolutional neural network
DIC	Digital image correlation
DVC	Digital volume correlation
EM	Electromagnetic
eV	Electronvolt
FCNN	Fully convolutional neural network
FN	False negative
FP	False positive
IoU	Intersection over Union
mAP	Mean average precision
microCT	Micro computed tomography
NN	Neural networks
SO	Specific objectif
TN	True negative
TP	True positive
Z	Atomic number
Z_{eff}	Effective atomic number
ε_{el}	Elastic strain

μm   Micrometer

I_p Polar moment of inertia

ε   Strain

σ   Stress

E   Young's modulus

Φ   Twist angle

CHAPTER 1   INTRODUCTION

Osteoporosis affects over 200 million people in the world, including 1 in 5 men during their lifetime and 1 in 3 women over 50 years old [1]. In North America, an estimated 10% of the population over 50 years old is affected [2] [3]. The disease is characterized by the reduction in bone density due to changes in bone remodeling, a process that happens normally throughout your life. However, in osteoporosis, bone reabsorption becomes faster than bone formation. Hence, the bone microarchitecture is affected and the risk of fracture increases [4]. The major problem with osteoporosis is the lack of symptom before fractures, making it hard to prevent severe accidents [5]. Current investigations aim at improving our understanding of bone by inferring on its mechanical and physical properties. Some of the current practices include the study of microfracture, mechanical properties and strain patterns.

2D imaging is the oldest method used to evaluate microdamage in bones, but it requires the destruction of the sample, making it impossible to gather information about the sample before mechanical loading. The obtained information is also limited to one plane whereas microdamage is a 3D structure. Hence, 3D techniques, like microCT imaging, have been developed to retrieve a more complete evaluation of damaged bone structures. The gold standard is currently to use contrast agents to easily quantify the microdamage during image analysis. A contrast agent is a high-density substance that absorbs more Xray radiation than bone tissue and will also precipitate inside microcracks. However, it does not segment the absolute damage volume since it can also precipitate in any voids, like lacunae. It can also encounter problems segmenting damage developing deeper into the tissue. With the improvement of imaging techniques, new segmentation approaches using high-resolution images could make it possible to segment damage without a contrast agent [6-8].

In addition to damage quantification, bone mechanical properties can be measured from mechanical testing. One can then establish relationships between mechanical parameters, such as Young's modulus, and physical parameters, including microdamage volume [9]. Another way to study bone properties is to deform the sample in multiple steps and measure the 3D strain inside the bone sample, using digital volume correlation (DVC), which allows locating areas of high

strains in 3D. Indeed, DVC provides a lot more information than only using the relative 2D strain of the sample [10].

Currently, there is no study including the 3D measurement of bone microdamage, mechanical properties and 3D strain patterns using only one procedure. Hence, this project will focus on developing such a platform by conducting two studies. In a first study, trabecular bone cylinders were deformed at a quasi-static rate until ultimate stress is achieved and then imaged at high resolution. The images are used to train and test two neural networks, YOLOv4 and Unet, for the detection and segmentation of bone microdamage. Afterward, in a complementary study, a trabecular bone sample is deformed in 2 incremental steps combined with high resolution imaging before and after every loading step. The 3D volumes are then used to measure the 3D displacement maps using a DVC software. In both studies, the procedure for mechanical test and imaging were designed to include mechanical properties and physical properties measurement when required. This way a complete 3D ex vivo procedure can be derived from both study and include microdamage segmentation, 3D strains maps measurement and mechanical properties of bone tissue.

CHAPTER 2   LITERATURE REVIEW

2.1   Bone Tissue Composition and Function

The human skeleton is a complex system composed of about 270 bones at birth, which will fuse to a total of 206 to 213 bones for an adult [11]. It might seem to be an unfunctional system at first glance, but it serves multiple important functions [12, 13]. First of all, it serves as support and protection for the rest of the human tissues, such as lungs and heart. It is also used by muscles, tendons, and ligaments to induce movements or control the body's ranges of motion. Moreover, it serves as a storage to regulate the body's minerals. The bone marrow, found in trabecular bone and inside the diaphysis of long bones, is responsible for the production of different types of blood cells.

The bone has the capacity to adapt to its surrounding environmental changes [12], referring to two important processes, bone modeling and remodeling. The first is the growth of the bone to adapt to outside forces by changing its shape or by adding mass. The second is the constant absorption and creation of bone matrix to replace damaged bone structures with new bone while maintaining or even decreasing mass. Both processes are similar, but modeling implies either absorption or formation of bone tissue separately and remodeling implies an alternation of both mechanisms together [14].

Bones can be categorized into five groups [15]: long bones, short bones, flat bones, irregular bones and sesamoid bones. Long bones are cylindrical and have a greater length-to-width ratio than other bone types. This last characteristic provides them with the ability to transmit a great amount of force, by acting as a lever, during muscles contraction. Their internal structure is practical for the visualization of the different parts of the bone micro architecture, since it includes most of them [16]. Long bones can be separated into three zones, each with specific characteristics: epiphysis, diaphysis and metaphysis (Figure 2-1). The epiphyses are located at each end of the bone. The diaphysis is located at the center of the bone and its hollow center is called the medullary cavity, which is full of yellow bone marrow. The diaphysis and epiphyses are separated by the metaphyses, which have a conical shape and include the epiphyseal line (or growth plate).

Bone tissue is a highly specialized connective tissue composed of a mineralized bone matrix and bone cells. The bone matrix is made from an organic part that links to an inorganic component. The inorganic part is made of minerals, composed principally of calcium hydroxyapatite crystals, and is responsible for the hardness and durability of the material. The organic fraction is made of 90% collagen and 10% non-collagen protein [17].
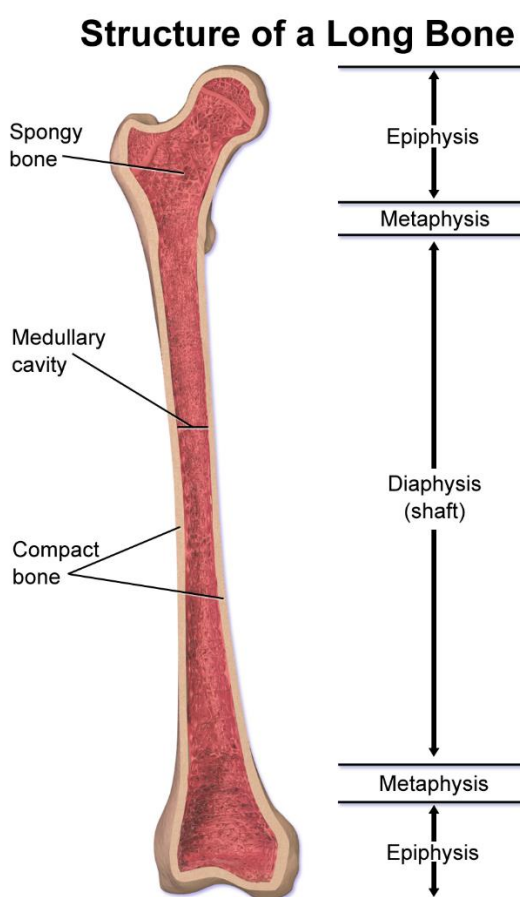
Figure 2-1: Typical long bone structure with its epiphysis, metaphysi, and diaphysis zones [18]

There are four types of cells in bone tissue, which all have different roles during the bone remodeling process. Osteoblasts are responsible of bone formation while osteoclasts are responsible of bone resorption. The bone lining cells do not show signs of bone formation or resorption. They would play a role in stopping the osteoclast from resorbing bone when they should not [19]. Another theory would imply a role in synchronizing bone resorption and formation [20, 21]. Lastly, osteocytes have been shown to act as mechanosensory guiding the bone remodeling process [19].

2.1.1 Trabecular Bone and Cortical Bone

Bone tissue can be separated into two structural categories : cortical and trabecular bone (Figure 2-2)[22]. Cortical bone is a layer on the outside of the bone, its thickness varies depending on the skeleton location. Cortical bone is dense and has a low surface area, which is primarily due to the surface inside of osteons, a microscopic cylindrical structure parallel to the bone axis. Osteons have a hole in their center, called the Haversian canal, through which blood vessels and nerves can pass to supply the bone in nutriments and communicate with the different subsystem insides [23].
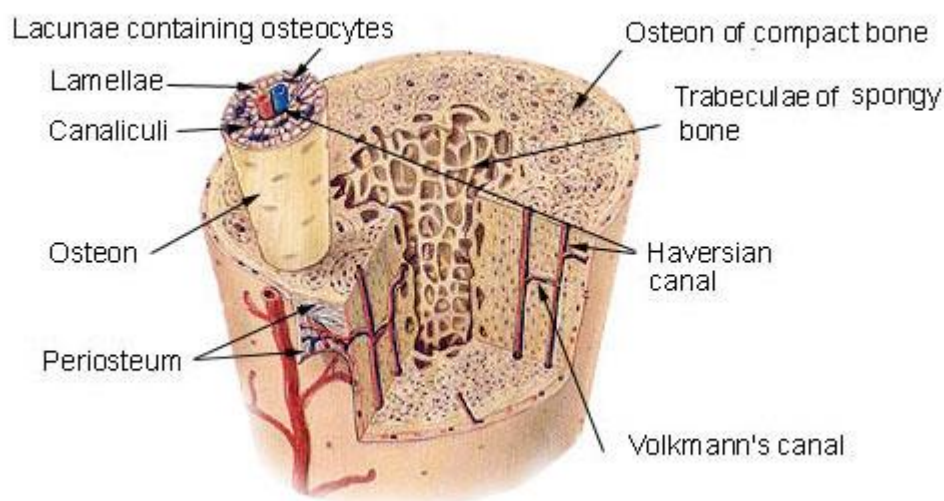
Figure 2-2: Cross-section of a bone showing the trabecular (spongy) and cortical bone(compact bone) including the osteon anatomy [24].

Trabecular bone has a greater surface area and lower density [22]. It is located in the center of flat bones, vertebrae, and long bones. It has a complex architecture made of interconnecting rods and plates called trabeculae. These are composed of layers made of mineralized collagen. The arrangement of the lamellae could be compared to the osteons in cortical bones. However, they are parallel to the trabeculae axis instead of the bone axis [25].

About 80% of the human skeleton's bone is made of cortical bone. However, the ratio of cortical to trabecular is dependent on the location in the skeleton [22]. Trabecular bone is predominant in regions like the vertebrae, the epiphysis, and metaphysis of the long bones [26], whereas cortical bone is thicker and predominant in the diaphysis of long bones and the femoral neck [27].

2.1.2 Bone Tissue Properties

Bone tissue can be characterized by its physical and mechanical properties, which will vary between trabecular and cortical bones and therefore reflect their roles. There are also strong correlations between some mechanical properties and some physical properties during mechanical testing [9].

2.1.2.1 Physical properties

The physical configuration of bones can vary a lot from species to species and also from one individual to the other. It depends on the role the specific bone has to play and the condition under which it is living [28].

2.1.2.1.1 Micro-architecture

Bone histomorphometry is useful for the evaluation of bone remodeling, metabolism, and micro-architecture [29]. Some examples of the micro-architecture parameters are the trabecular thickness (Tb.Th, mm), trabecular separation(Tb.Sp, mm), trabecular number (Tb.N), bone volume over tissue volume (BV/TV), and cortical thickness (Cort.Th, mm) [30].

The **Tb.Th** and **Tb.Sp** are the average thickness of the trabeculae and the average separation between the edges of two trabeculae, respectively. Both parameters are expressed in millimeters. The cortical bone also has a parameter similar to the Tb.Th, the **Cort.Th**, which refers to the mean thickness of the cortical bone in millimeters. **BV/TV** is the percentage of bone volume over the total amount of tissue in the sample. **Tb.N** is given in mm^{-1} and is representative of the number of trabeculae per unit of length [31-33].

2.1.2.1.2 Porosity

The porosity in bone, just like any other material, is characterized by the ratio of void over the sample volume, and can range from 0 to 100%. Trabecular bone porosities vary from 30 to 90%, while more compact cortical bone has a porosity varying from 5 to 30% [34]. Trabecular bone porosity varies more because it has a much higher surface area exposed to marrow and blood flow, giving it faster bone remodeling and adaptability [35]. It will adapt depending on the loading a specific region in the skeleton will undergo during its host life.

2.1.2.2 Mechanical Properties

Bone's mechanical properties describe its ability to sustain the different loads the body must support or produce during its life. For example, the forces be used to induce movements or the force from the impact with another object. Bone mechanical behavior does not follow a simple linear relationship. On the contrary, it is a complicated structure that includes multiple variables. Indeed, it is said to be an anisotropic viscoelastic material [36]. Bone mechanical properties vary greatly between cortical and trabecular bone tissues [37]. The difference between both bone types can be characterized by their respective mechanical properties, such as the Young's modulus, the ultimate forces/stresses, and the Poisson's ratio. These parameters can be determined by mechanical tests on bone samples. Some of the common tests include the three or four-points bending tests, torsion test, the uniaxial tensile test, and the uniaxial compression test [38-40].

In engineering, the strength of a specific material can be measured using the relationship between the loading force and the displacement during mechanical testing. The graph of this relationship results in the force-displacement curve. This curve depends on the dimension of the sample used for the test. The corresponding stress-strain curve can be derived by normalizing this graph to the sample geometry, now representing intrinsic properties of the material. In most mechanical test, the force is divided by the sample cross-section area to provide the stress:

$$\sigma = \frac{F}{A} \quad (1)$$

and the displacement is divided by the sample initial length to provide the strain [41, 42]:

$$\varepsilon = \frac{l}{L} \quad (2)$$

Figure 2-3 shows a typical stress-strain curve obtained from a mechanical test on a bone sample. It includes two regions that define different stages of the deformation: the elastic zone and the plastic (or permanently deformed) zone [43]. Even if biological tissues are more complex than the typical engineering material, their intrinsic properties can be extracted from these curves to characterize bone. Properties may however exhibit greater standard deviations depending on the origin and location of the bone in the body [44, 45].
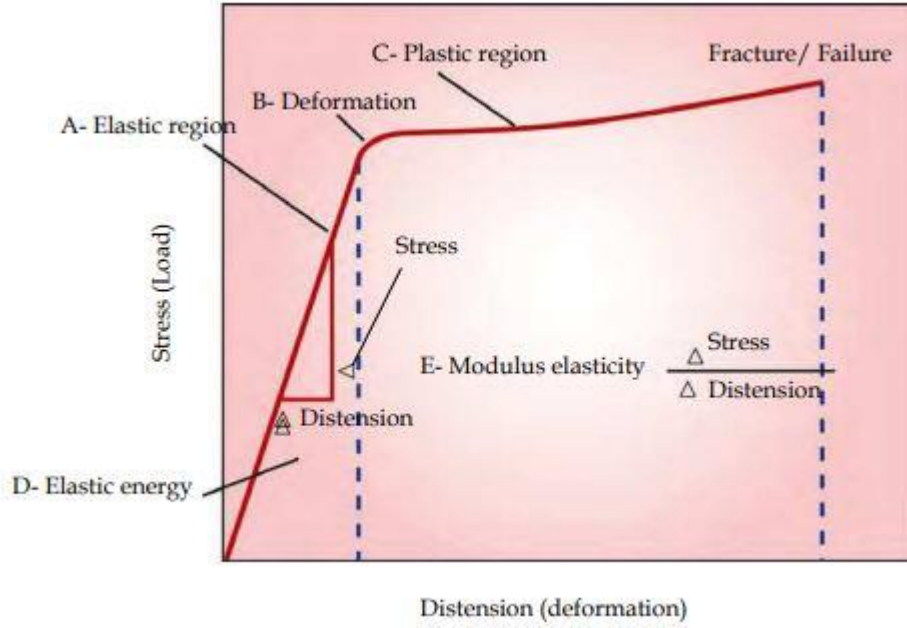
Figure 2-3: Stress-Distension curve (also called stress-strain) showing the different regions of the mechanical deformation of an engineering sample. A) linear region representing the elastic region of the deformation with a slope equal to the Modulus of elasticity (E) and the energy of the elastic deformation is the area under the curve(D). B) is the yield point, announcing the beginning of the plastic region (C) [43]

The behavior of the perfect elastic material, usually represented by a spring, is described by Hooke's law. It can be used for the elastic region of any material, since the material is assumed to be a perfectly elastic material before the plastic (permanent) region [46]. The law describes the deformation like a linear function between the stress and the strain in the material:

$$\sigma = E\varepsilon_{el} \qquad (3)$$

where E is the **Young's modulus** in MPa, σ is the **stress** in MPa and ε_{el} is the **strain** in mm/mm. During the linear deformation, the material does not undergo permanent damage/deformation. Therefore, if the load is released during the elastic deformation, the sample should regain its initial shape. Point B in Figure 2-3 illustrates the yield stress (σ_y) and the yield strain (ε_y), which indicate the threshold where the material enters its plastic region. In the plastic region of the curve, the bone tissue starts to yield and a plastic flow can occur in the amorphous part of both the mineral and organic phase of the bone [47, 48]. During the plastic deformation, energy is used and ejected by the system, which is given by the area under the plastic curve. This results in permanent damage to the bone sample. If the load is removed, the sample will try to regain its initial shape but will be permanently deformed proportionally to the energy spent in the plastic zone [49, 50]. The size of

the permanent damage is represented by $\varepsilon_{plastic}$ in Figure 2-4. The end of the plastic zone is marked by the failure of the sample.
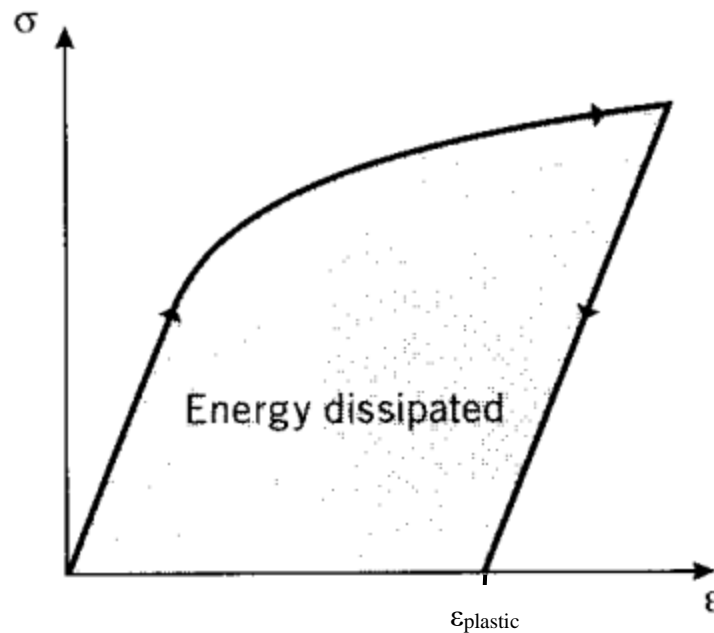
Figure 2-4: Stress strain curve showing the energy lost during plastic deformation and the resulting permanent deformation [51]

An important characteristic of the mechanical properties of bone tissue is the difference in the response depending on the loading conditions. From Figure 2-5, we can observe a difference in elastic modulus between the longitudinal and transverse loading. S. Li observed an average Young's modulus for longitudinal loading of 20.22±3.12 GPa and 19.09±2.84 GPa in tension and compression respectively. On the other hand, transverse loading averaged 12.43±2.37 GPa and 11.62±2.4 GPa in tension and compression, respectively [52]. Other studies showed similar results [53].

Even if the elastic moduli are quite similar between tension and compression in cortical bone, the load sustained by bone under tension is much lower than the load sustained under compression. Both failure of the sample and yeilding happen at much higher stresses in compression, meaning that bone is much tougher under compression than tension. Moreover, when the sample is under tension, it seems to be able to undergo more deformation in the longitudinal direction than in the transverse direction, before the failure of the sample.
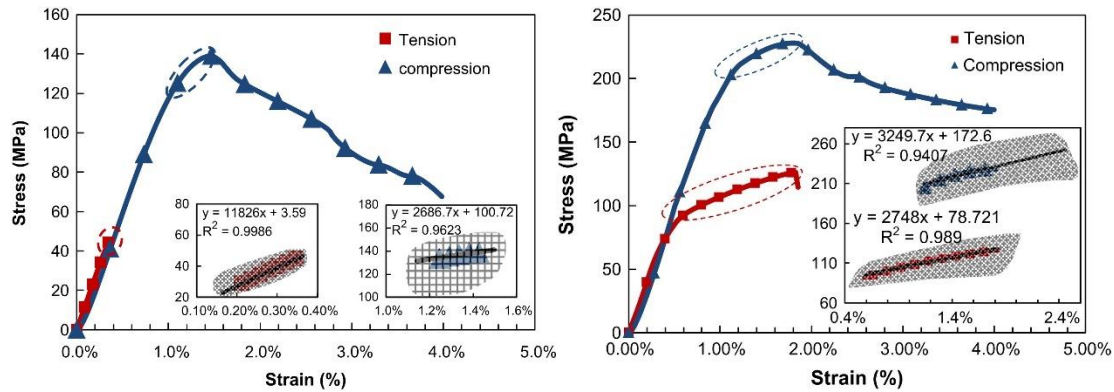
Figure 2-5: Stress and strain curve for the mechanical loading of a cortical bone sample (A) in the transverse direction and (B) in the longitudinal direction [52].

2.1.2.2.1 Viscoelasticity

Bone is considered a viscoelastic material, which implies that its mechanical properties will vary depending on the strain rate used during mechanical testing (Figure 2-6). The literature clearly shows that as the strain rate increases, the bone gets stiffer and sustains a higher load. However, since bone has a mineral inorganic part, the variation will not be as great as it would be with soft tissues like tendons and ligaments [54, 55]. Moreover, this behavior was further proven true by studying its stress relaxation after loading [56], which is a reduction in stress over time at a constant strain. This means that even if the displacement is kept constant at the end of the test (the load is not removed from the sample), the bone should still undergo a reduction in stress [57].
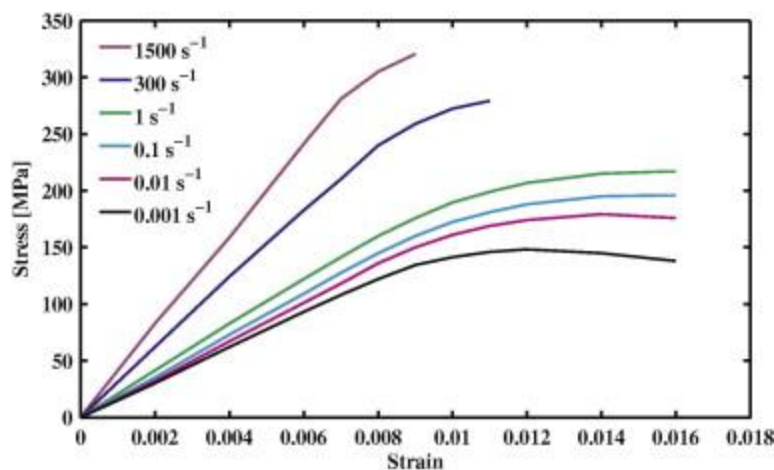
Figure 2-6: Compressive stress-strain curves for human femoral cortical bone as a function of strain rate [58]

2.1.3 Ex vivo Mechanical Testing

In order to obtain bone mechanical properties, different mechanical testing configurational can be used. Generally, the mechanical test done on bone tissue will be similar to a more typical engineering material. However, because of its complex structure, composed of an inorganic and organic part, the evaluation of said properties is challenging. The tissue can be studied from a macro level, whole bone or compact/spongy bone, to its sub-nano levels, collagen molecules[59]. This literature review will focus on tests done on sample size in the order of the bone macrostructure.

Testing methods include monotonic, quasi-static loading (tension, compression, torsion, bending) [60-62] and dynamic loading(impact test and fatigue test) [61, 63, 64]. Some of the most common techniques are discussed below. Usually, the samples are prepared using a diamond tool, saw, or core drill bit, under constant irrigation to reduce the amount of damage induced by the cut and heat created by friction and are conserved below freezing, generally -20 degrees Celsius, and thawed out before mechanical testing [65-68].

2.1.3.1 Compression and Tension

Both compression and tension testing have a sample subjected to a uniaxial loading, which is a force applied along the primary axis of the sample. The samples are generally loaded until failure at a constant strain rate, with the test being controlled by force or displacement. Then the stress-strain curve is computed from the force displacement-curve using the stress and strain equation (1) and (2) previously discussed.

Compression testing and sample preparation.

In the case of compression, the specimens are generally cylindrical or cubic samples. It is important to have an height less than twice the width of the sample to avoid any buckling [69]. To ensure parallelism of each end of the sample, some authors will glue each end of the sample to a brass end-cap, others will use an ultra-fine polisher to assure parallelism [66, 70, 71]. This way the load is ensure to be mostly applied along the principal axis of the sample.

Tensile testing and sample preparation.

For tensile testing, the samples are attached at both ends using screws and mounting plates. The ideal shape is a dumble, also called dog-bone (Figure 2-7), where each end is larger than the center since they will have holes for the screws to be attached and have a higher surface for the test setup to grip and pull the sample. The dumble ends gradually reduce to the center width using a circular/rounded junction to reduce the stress concentration factor. The highest stress region is then assumed to be in the center of the sample. Hence the precise dimension of where the failure happens can be used to compute the stress-strain curve. Moreover, in the case of 3D imaging, the scanner can focus in the middle section of the sample [72-74].
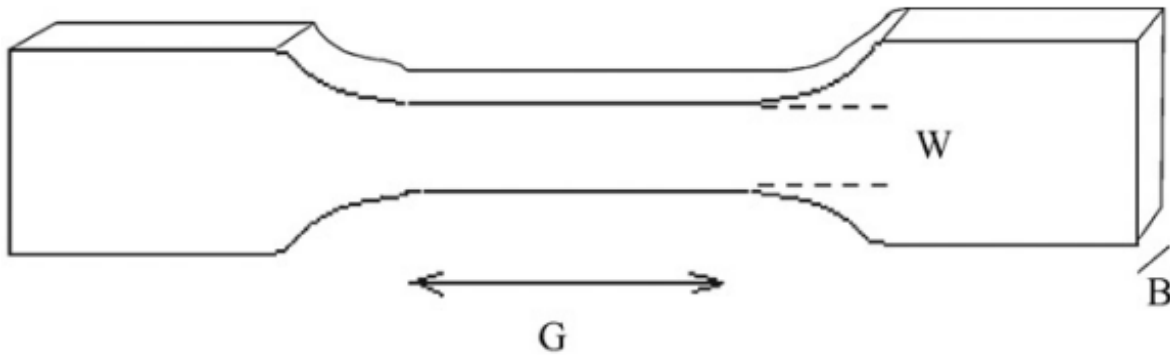
Figure 2-7: Dumbell shape where G is the test length, W the width, and B the thickness [75].

2.1.3.2 Bending

Bending tests are generally set up following two different configurations: the three-points and the four-points bending test (Figure 2-8). The sample is either a whole long bone or shaped as a prismatic beam. Both configurations have two supports at the bottom of the samples, one at each end of the testing zone. The difference is that the three-points bending has one loading point directly in the center of the specimen, while the four-points bending has two loading points equally separated on each side of the center point. In an experiment including 3D imaging of the fracture zone, a notched can be done in the middle of the sample to help focusing the imaging zone if the sample is too big [76-78].

For three-points bending, the bending stress for a rectangular and annular cross section is determined by the equations (4) and (5) below:

$$\sigma_{rect.} = \frac{3FL}{2wh^2} \quad (4), \qquad \sigma_{annul.} = \frac{3FL}{\pi(R^3-r^3)} \quad (5)$$

where F region is the load, L is the length between the two bottom supports, w the width and h the height of the rectangular sample and R the outside radius and r the inside radius of the annular sample.

For four-points bending, the bending stress for a rectangular and annular cross section is determined by the equations (6) and (7) below:

$$\sigma_{rect.} = \frac{3F(L-a)}{2wh^2} \quad (6), \quad \sigma_{annul.} = \frac{3F(L-a)}{\pi(R^3-r^3)} \quad (7)$$

where a is the distance between the two applied load[79-82].
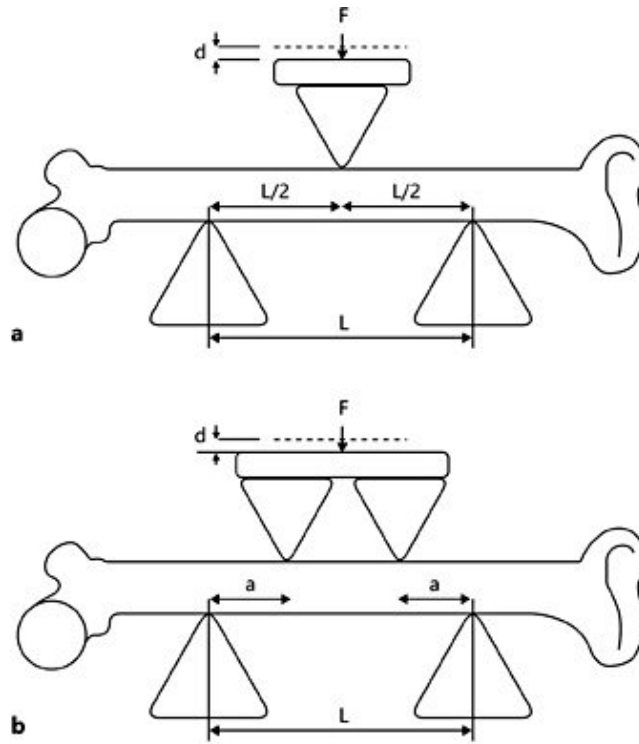
Figure 2-8: A) three points bending configuration B)four points bending configuration[83]

2.1.3.3   Torsion

Bone samples are tested under torsion when we want to investigate the shear properties of the biological material. The samples are generally cylindrical or annular cylinders. Both ends of the sample are fixed inside a chunk or other clamping system on the testing setup. Usually, only one

end of the system is rotating, and the other is fixed. Once the sample is mounted onto the test apparatus, the experiment is controlled by applying constant angular displacement until failure. The shear stress(τ) and shear strain(γ) can respectfully be computed using the following equations (8) and (9):

$$\tau = \frac{Tr}{I_P} \ (8), \qquad \gamma = \frac{\phi r}{L} \qquad (9)$$

where T is the torque, I_P is the polar moment of inertia, r is the gage radius, L is the gage length, and ϕ is the twist angle. Like other loading configurations, a stress-strain curve can be obtained and the shear modulus (G) can be computed from the slope of the elastic region [84, 85].

2.1.3.4   *Fatigue loading*

All the loading configurations can be used to investigate the fatigue properties of bone tissue. The sample preparation should be the same as quasi-static loaded samples. The difference comes from how the load is applied. While quasi-static loading has a load consistently applied until failure. Fatigue loading uses a dynamic load, which is a cyclic repetitive application of a load on the specimen. The controlled parameters are generally the mean stress, the maximum stress, and the number of cycles the sample goes through. Then the result can be graphed using an S-N diagram, where S represents the constant amplitude stress level and N represents the number of cycles to failure. Since the tests are generally much longer than quasi-static loading tests, the sample temperature and hydration should be maintained to keep the result as close as possible to *in vivo* setting [86, 87].

2.1.4 Osteoporosis

Osteoporosis causes a reduction in bone density and affects the integrity of bone micro-architecture, hence increasing the risk of fractures [4]. It is also considered a silent disease due to the lack of symptoms before fracture [5]. Moreover, osteoporosis can have severe consequences in older patients [88], because of the frequent fracture in important bone like hips and the spine [89]. While studying osteoporosis, it is important to know the importance of the bone turnover rate in both trabecular and cortical bone. Bone loss in trabecular bone is going to be more important in the early stages of the disease because of its high surface area. However, since trabecular bone only accounts for a limited percentage of the total bone mass (20%) and because cortical bone pores

will grow bigger (because of bone resorption) as the disease progresses. The bone turnover in cortical bone gets more important in the later stages of osteoporosis because of its increasing surface area [90, 91].

2.2   MicroCT Imagery

Microscopic computed tomography is a popular imaging technique for the identification and quantification of microdamage. It has the advantage of being non-destructive, allowing studying bone samples over time. It also has the advantage of showing the microdamage in 3D, giving more information on the damage configuration perpendicular to the usual 2D plane.

2.2.1 Xrays

Having energy from 200eV to one MeV, Xrays are electromagnetic radiation with high energy. On the electromagnetic spectrum, they are located between gamma and ultraviolet rays [92]. In clinical imaging, they are generated from a device called the Xray tube, showed in Figure 2-9. Electrons are accelerated from a cathode to an anode by heating a filament, generally made of tungsten, to about 2400 K [93].
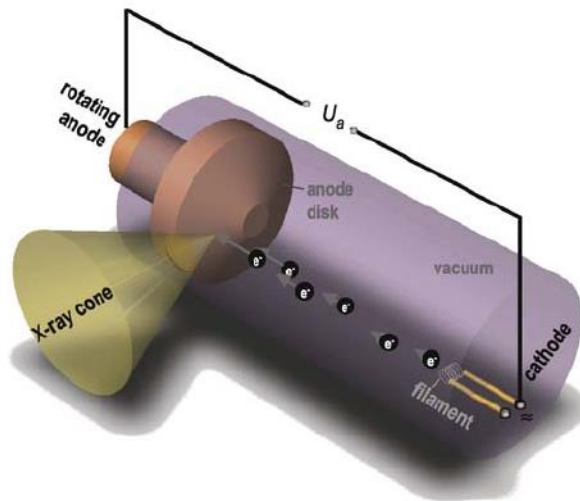
Figure 2-9: Schematic of an Xray tube where electrons are accelerated from the cathode to the anode to generate an X-ray cone [93]

Incident electrons can interact and transfer their energy with other atoms in two ways: collisional transfer and radiative transfer [94]. Collision is the most common energy transfer in Xray imaging.

The incoming electron transfers its energy to the absorbing atom's electron and a fraction of the kinetic energy of the incident electron is transferred to the absorbing electron during the collision. The electron that now has a high level of energy, will return to its original state by emitting infrared radiation, creating high heat in the anode disk. The incident electron might be deviated by the collision and even though its energy is diminished it can still have more interactions with other atoms, collisional or radiative [94]. Sometimes, a new electron can be accelerated by the collision, if the energy is high enough, creating a delta ray, which is another electron in movement with the possibility of forming collisional and radiative energy transfer [94, 95].

Radiative transfer of energy is responsible for the generation of Xrays and there are two types: characteristic radiation and bremsstrahlung radiation. The first happens when an incident electron collides with the electrons in the shell closer to the nucleus, often the K-shell in imaging [94, 96]. Then, an electron of a shell further from the nucleus replaces it. Since the binding energy of the inner layers is higher than the binding energy of the outer layers, the electron will lose energy as Xrays. It is called characteristic radiation because the energy difference between two nuclear layers is always constant (Figure 2-10), therefore the Xray energy will have a constant value for each electron transfer between the same two layers [94, 97]. Bremsstrahlung radiation results from the deceleration of an incident electron by the nucleus (Figure 2-10). Indeed, sometimes the accelerated electrons will penetrate the atoms without colliding with any electron, but the charge of the nucleus will attract the incident electron and change its direction and decelerate it at the same time. The energy lost during this deceleration will result in the formation of an Xray. Unlike characteristic radiation, the Xray energy resulting from this deceleration is not constant because the initial speed of the electron and the distance from the nucleus is highly variable. It has a large range of values that depends on the source kV [94, 98].

Another type of interaction in Xray imaging is the electromagnetic (EM) radiation [94]. This type of energy transfer involves the interaction of an Xray photon with an atom instead of an electron (a particle). Two EM radiation mechanisms are the photoelectric effect and Compton scatter. The first one consists in the complete absorption of a photon by the atom, the absorption of this energy provokes the ejection of an electron, usually on the K layer, which is called a photoelectron. Like in characteristic radiation, its replacement by an outer layer electron generates a characteristic Xray. The photoelectric effect is the principal source of contrast in medical imaging. The

probability of photoelectric effect is proportional to the effective (or average) atomic number (Z_{eff}) of a material to the power 4. Therefore, a material like bone, a mineralized tissue, has higher Xray absorption than soft tissue [93, 94, 99].
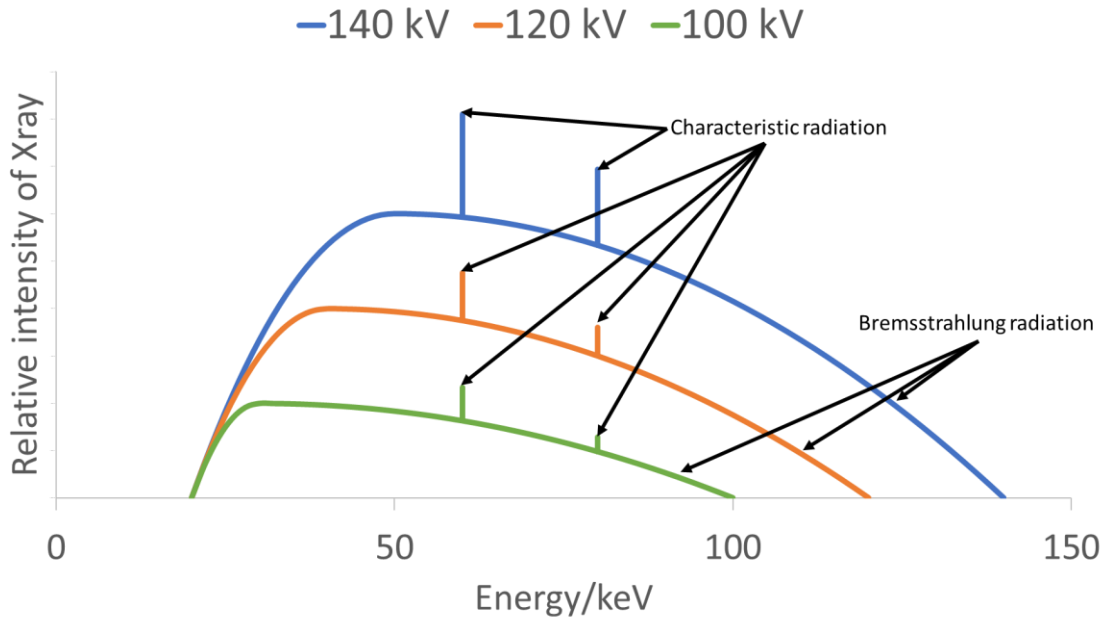
Figure 2-10: Graphical representation of the Bremsstrahlung radiation intensity and the peaks of each characteristic radiation, and this for different source energy [94]

The second EM radiation mechanism does not involve the complete absorption of the Xray photon energy. It interacts with a peripheral electron, which is then ejected from the atom, while the photon is redirected with less energy. The ejected electron is then called the Compton electron. The redirected photon can still interact with other atoms, which induces more radiation to unwanted regions inside the material, which can create poor contrast or noise in the image [93, 94, 100].

2.2.2 Xray Imaging and Micro Computed Tomography

The previous sections discussed the several forms of radiation created by an Xray tube. Now this section will discuss how an image is formed using those Xrays.

 When going through a bone sample, radiation will be absorbed by all the atoms present inside the volume. The atoms in air, bone and marrow having different density (or Z_{eff}), will absorb Xrays to a different degree [94]. Then the Xrays that went through the sample will be converted to visible light by a scintillator and the visible light will be recorded by a photodetector [101]. For every

continuous exposition to an Xray beam, one 2D image can be formed. Xray imaging uses a grey color scale to represent Xrays absorption: white being a dense material that absorbs a lot of Xrays, and black being a low density material that absorbs little Xrays. Therefore, the contrast between different tissue in the sample will depend on their density [94].

Micro-computed tomography (microCT) is an imaging technique used to recreate a 3D image of a specimen using Xrays. Thanks to this relatively new technique, it is possible to see the internal structure of a sample without its destruction and some apparatus can reach a resolution lower than a micrometer [101]. The technique uses several 2D scans to make a 3D reconstruction of the sample (Figure 2-11). This way, multiple scans can be taken of the specimen under different conditions, for example, after several steps of mechanical loading [102].
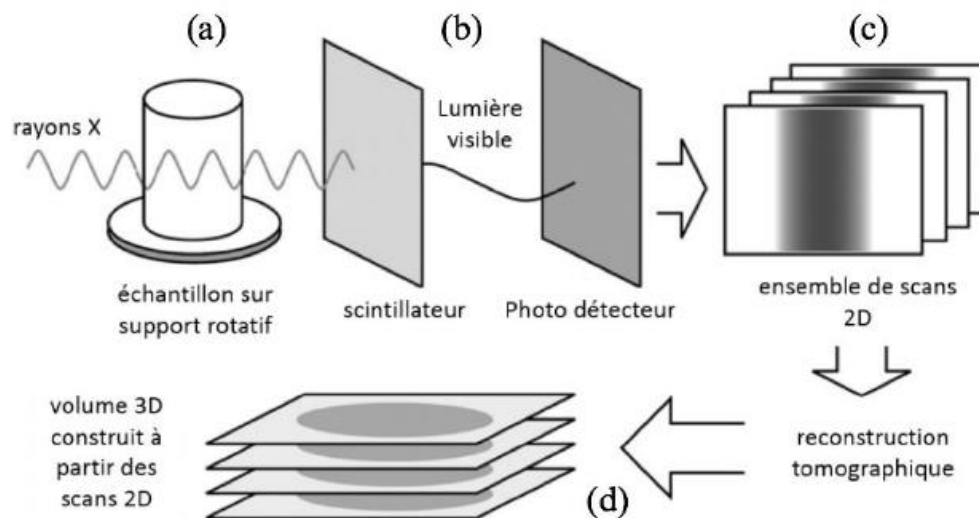
Figure 2-11: Different steps included in the Xray tomography process. From the Xray scanning of the rotating sample to the 3D reconstruction made from multiple 2D scans [101].

2.2.3 Contrast Agent

A contrast agent is a substance used to enhance the contrast of a specific tissue from the other living tissues. Contrast agents used for the microCT scanning of bone tissue consist of a material able to absorb more Xrays than bone. On a greyscale, the colored structure would be of a bright white, hence creating a different contrast between bone and targeted structure (white on grey) than the one between bone and background (grey on black). To be able to absorb more Xrays than bone,

the agent must have a high atomic number [103], which means that it will most likely be heavy metals. Therefore, contrast agents are toxic and must be properly disposed of.

The contrast agents used in recent studies for microCT scanning of bone microdamage are barium sulfate ($BaSO_4$) and lead uranyl acetate [104]. The contrast agent is typically applied after the last mechanical loading of the sample, in which the bone marrow has been washed out for better penetration of the substance. The literature does not seem to agree on one specific staining duration when it comes to bulk staining of bone sample, but it usually goes from 2 full days to several weeks for the proper penetration of the agent [66, 105-107].

2.3 Bone Microdamage

Bone like any other material is subject to physical damage. Some damage is not visible to the human eye, called microdamage, but it is believed to play a role in fracture mechanism and bone remodeling [108]. Therefore, microdamage is studied by using mechanical testing to induce microdamage in a trabecular or cortical bone sample, and then by scanning the sample using different techniques to visualize the microdamage.

2.3.1 Types of Microdamage

Microdamage can be separated into two categories: linear microcracks and diffuse damage [109]. Microcracks are characterized as sharp cracks with a length of about 50-100um. They tend to accumulate, because of fatigue, during normal human activities like walking and running. Non-organic engineering material would normally fail under excessive fatigue loading. However, bone microcracks have been shown to interact with the osteocytes and therefore have an important role in the bone remodeling process [108, 110]. It is also believed that there is a correlation between multiple mechanical properties and the formation and quantity of bone microcracks [110].

Diffuse damage is an agglomeration of sublamellar sized cracks (submicron sized) [108, 110, 111]. Diffuse damage was also shown to correlate with bone fragility [112-114]. More specifically, in studies by Diab and Vashishth [112-114], it was shown that donors with more diffuse damage had a longer fatigue life compared to the ones forming more microcracks. Therefore, it was concluded that diffuse damage has an important role in the mechanical properties of bone tissue. Moreover,

they showed that younger donors tend to form more diffuse damage and that the older ones tend to form more microcracks [112-114].

2.3.2 Evaluation Techniques

There are multiple techniques used to identify, characterize and quantify bone microdamage. They can be separated into two main categories: 2D and 3D techniques. They are both used to give qualitative and/or quantitative characteristics of the damage.

2.3.2.1 2D Methods

2D imaging techniques are generally destructive techniques that do not allow analyzing a complete sample volume. Indeed, thin slices of bone samples must be cut off and then imaged. This means that these techniques cannot be used in a longitudinal study to investigate the same sample under different conditions, such as incremental loading steps. Popular techniques include light microscopy, scanning electron microscopy, laser scanning confocal microscopy, and atomic force microscopy, used in early bone microdamage studies [104].

The simplest and most common way to quantify micro-damage in 2D is to evaluate the **crack density** (#/mm^2) of bone including linear microcracks or/and diffuse damage. This represents the density of cracks normalized by a bone area [107]. More parameters like the crack number, crack length, and crack surface density can also be measured.

2.3.2.2 3D Methods

Even though 2D methods were used for an extended period and are still used today, 3D methods have obvious advantages over 2D methods. First, 3D methods do not require the destruction of the bone sample, the whole volume is scanned using 3D imaging technique like Xray microCT. This opens new possibilities, like scanning the sample before and after mechanical testing or it can even undergo multiple deformations and multiple intermediate scans to see the progress of the internal structure [115]. Secondly, a volume can be visualized instead of an area. This means that the information of microcracks perpendicular to the typical 2D plane discussed in the previous section is now available. This gives complementary information on the development and characteristics of microdamage and allows quantifying a volume instead of an area.

A popular technique to quantify microdamage is to use a contrast agent with microCT. It helps identifying and locating linear microcracks and diffuse damage. Moreover, the quantification of microdamage, while using a contrast agent, can be done using an image processing software. A thresholding segmentation is used to create a volume of interest (VoI) for the bone tissue and the stained microdamage since they have different grey intensities. The ratio of damage volume to bone volume (DV/BV) is often used to measure the amount of damage in bone, which is simply a ratio of the two segmented VoI. Other characteristics like crack density, damage surface (DS), and average crack dimension can still be extracted with 3D techniques [104, 116, 117].

While the use of a contrast agent makes it possible to visualize the area of micro-cracks and diffuse damage, which would normally be hard to see at the image resolution, it also has its drawback. Since the sample is not cut into a thin slice, sometimes the contrast agent will not be able to penetrate micro-cracks that are not connected to the surface area of the bone [118]. Moreover, the bulk staining period can be long, up to 2 to 3 weeks, and since it uses heavy metals. It can also be toxic to human and aquatic life [119]. The last disadvantage is that sometimes the agent will stain more than the microdamage itself. Indeed, it can also penetrate bone microstructure like lacuna and mark them as micro damage [107, 120].

2.3.2.2.1 Without Contrast Agent

The improvement in microCT resolution and computer hardware are opening new possibilities for the quantification of microdamage without a contrast agent. Some have developed an algorithm that uses different types of filters to automatically segment microdamage [6-8].

A first technique, based on mathematical morphology, applies a sequence of morphological dilations and erosions, on a binary segmentation of the image, to fill the area inside the cracks with pixels (Figure 2-12) [6]. First, a dilation kernel is applied. Its size and the number of times it is applied will determine the biggest possible crack detected by the method. Afterward, an erosion kernel of the same size and shape is applied the same number of times plus one, to retrieve a binary mask of the same size or slightly smaller than the initial segmentation and to close the cracks at its extremity. Although its simplicity, this technique does not discriminate crack-like features and often results in false positive cracks segmentation.
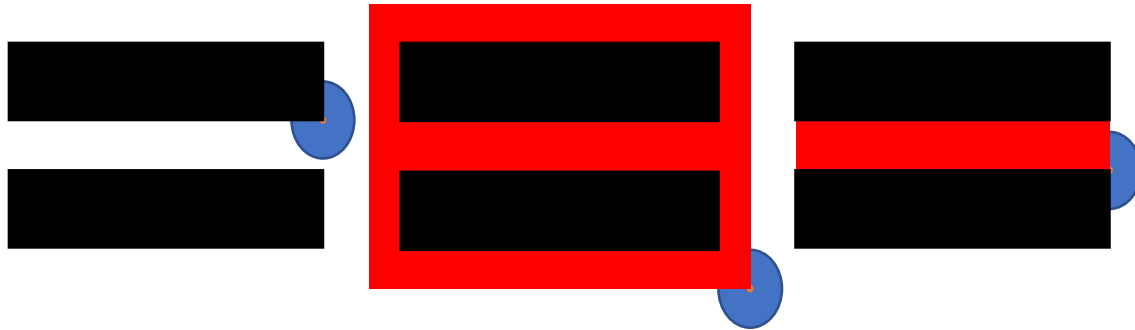
Figure 2-12 : A sequence example of a single dilation and erosion to close the space between two black rectangle (which represent the bone on each side of a crack). The blue circle represents a kernel of circle shape and the red is the area created by the morphological operations. On the left is the initial binary image. In the middle is the image following the dilation operation.On the right is the image following the erosion operation

Another technique consists of using the advantages of having a 3D information about the cracks. Microcracks being planar structures, a steerable filter is used to extract the relevant information [121], which is a filter that will result in high intensity around planar features. Combining the grey pixel intensity of the initial image to the steerable filter response using a nonlinear operation, they are then able to segment microcracks using thresholding. Lastly, cracks are separated from accidently segmented non-cracks features, like lacunae, using two thresholds: one on the anisotropy of the detected structures, and one on the ratio of the bounding box volume to the actual structure volume. By combining both thresholds, they can avoid rejecting long and curved cracks that would be rejected if only one of the two criteria was used [7, 8]. Both studies using this method were using Synchrotron radiation microCT as imaging modality which is expensive and not readily available. Moreover, it still made mistakes if microcracks were connected to pores, it would segment the entire pores as microcracks [7, 8].

2.4 Deep learning

With the recent improvement of microCT scanners now reaching a spatial resolution of less than a micrometer and presenting a noise level sufficiently low, this imaging modality becomes more interesting for microdamage detection and analysis. This opens new opportunities for automatic segmentation without contrast agents. In contrast to classical segmentation techniques requiring empirical parameter tuning, supervised machine learning algorithms have the ability to learn a particular task (here segmentation) from an annotated set of images, called a training dataset. Currently, the state-of-the art in machine learning is deep learning, which is a subfield of machine

learning, it consists of multiple hidden layers of artificial neurons trying to simulate the capacity of the human brain to interpret different data types, like images [122, 123].

Artificial neural networks (ANN) or neural networks (NN) are algorithms based on the biological neurological system. A biological neuron receives an input at its cell body. If this input signal is above a certain threshold, the neuron will send a signal through its axon to the terminal synapses. Therefore, neurons are either sending or not sending a signal, no in between [124]. Similarly, an artificial neuron gets a series of inputs and depending on its activation function and the weights attributed to each input it computes an output value [125]. While biological neurons' output is binary, artificial neurons can output a continuous numerical value. The inspiration from a biological neuron can be observed in Figure 2-13.
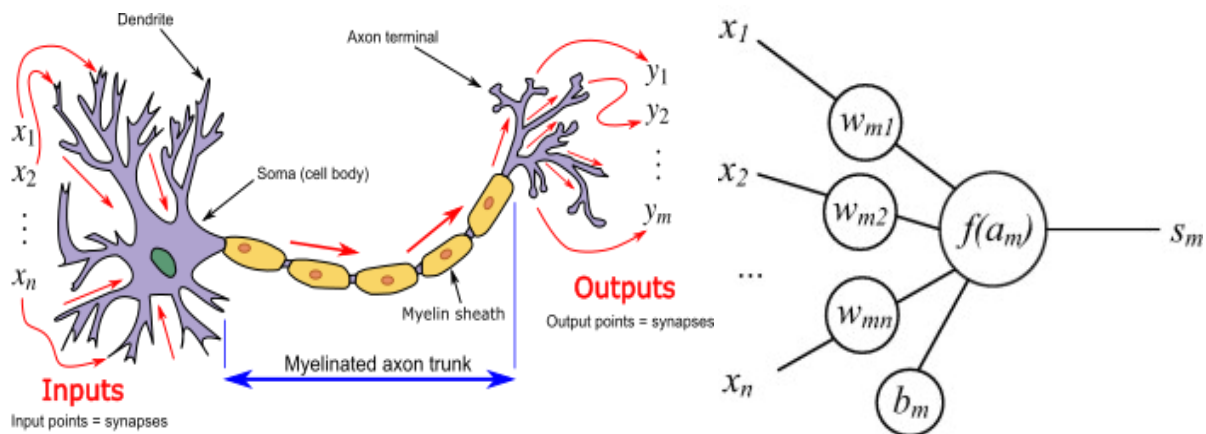
Figure 2-13: Biological neuron (left): the dendrite receiving several input signals and the cell body processing the signal. If the sum of the inputs reaches the threshold, the cell body sends an action potential through the axon towards the synapses [126]. Artificial neuron (right): several inputs x_i are received and are attributed a weight w_{mi}. Then the neuron computes an output value s_m using its programmed activation function f [125].

A NN is composed of multiple connected artificial neurons, which can get input and pass away outputs from neurons to neurons. Generally, these networks are arranged in layers. From a simple system composed of one input layer, one hidden layer and an output layer to more complex systems composed of several hidden layers, which are called deep layers neural networks and are the types of NN used in deep learning [127].

To train themselves, NN will go through their layers forward and backward. This process is called forward and backward propagation. During forward propagation, the network uses the current weights and activation functions to go from left to right, from the input training data to generate corresponding outputs. The latter are then compared to reference values associated to the training

data, using a loss function to be optimized. Then, the backward propagation is the process of computing the gradient of the loss function, and propagating it from right to left adjusting the neurons' weights [128].

2.4.1 Fully convolutional neural network

One type of ANN used in image analysis is the convolutional neural network (CNN) (Figure 2-14). This network is generally composed of a succession of several convolution layers, pooling layers, and fully connected layers [129]. A convolutional layer is a series of image filters, also called kernels, that are applied to the input to extract its feature maps, which are extracted information about the image.
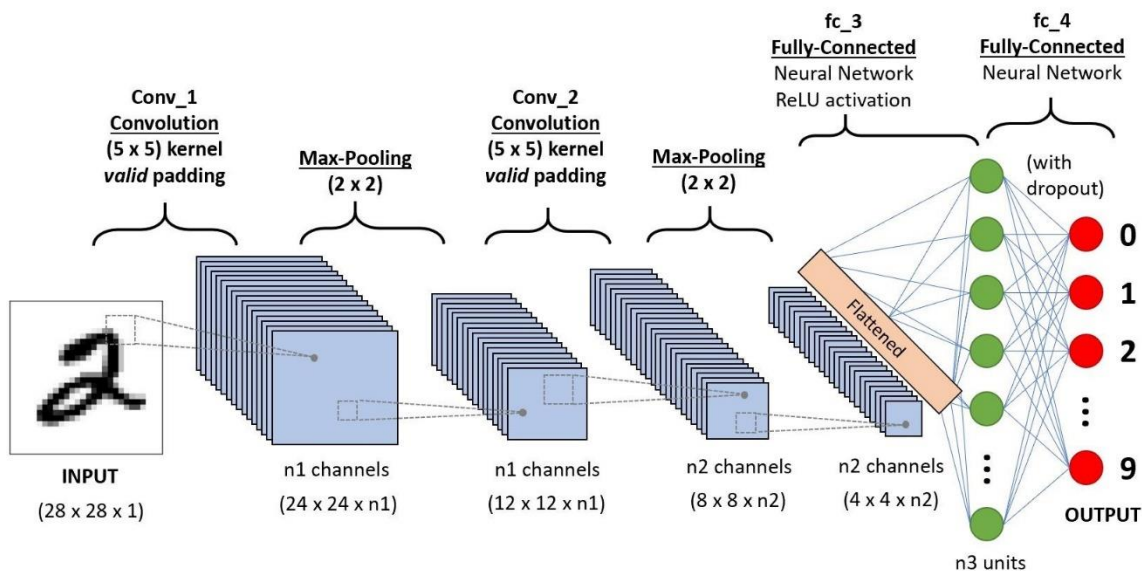
Figure 2-14: CNN architecture from the input on the left to the classification output on the right [130].

The center of the filter is applied to every pixel of the input and the mathematical result is one single value for every pixel the kernel is aligned with(Figure 2-15) [131]. The values inside the kernels are the convolutional layers' weights, which can be modified during training. Depending on the number of convolution filters used, it can results in many feature maps. Therefore, to counter this expansion in terms of features information, the resolution of each feature maps must be decrease. Hence why pooling layers are useful.
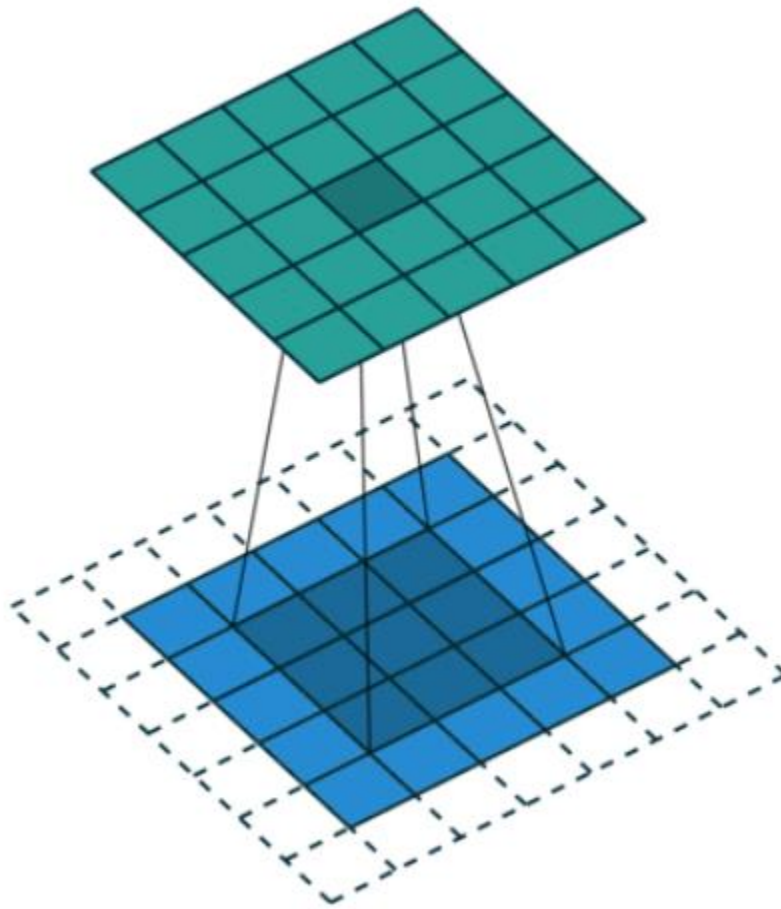
Figure 2-15: Application of a 3x3x1 kernel on a 5x5x1 input with padding to keep the same size at the output. Darken squares represent the pixels involved in the current convolution. The input image is in blue and the output feature map is in green [130].

The process of pooling layers, also called downsampling, is a way to reduce the dimension of the feature maps. To do so, a kernel similar to the convolutional layers is used. However, it does not have any weight. Instead, it uses an aggregate function to populate a smaller size output. The most popular filters are max pooling and average pooling. Max pooling outputs the pixel with the biggest value inside the filter and average pooling outputs the average of all the pixel's value within the filter [131].

Fully connected layers are composed of neurons layers, where every neuron of one layer is connected to every neuron of the previous layer [131]. Fully connected layers are composed of nodes, which can only give one value at its output. Therefore, CNN outputs are generally only

giving global information about the image, like its class (is it an image of a cat or one of a dog ?), and not giving an image as its output [132]. If segmentation is desired, fully convolutional neural networks (FCNN or FCN) come into play, a network only composed of pooling, upsampling and convolutional layers [133]. Upsampling layers are a set of deconvolutions to increase the size of the feature maps by adding zeros as padding between the pixels value to ensure that the NN output is the same size as the input [134].

An example of a FCNN architecture is shown in Figure 2-16; this one is called the FCN32, which goes from the smaller feature map to the full-size output in only one upsampling layer. However, the result would only be a rough segmentation of the object learned by the FCN [135]. To improve the quality of the segmentation, a gradual upsampling can be done instead [136]. These models are called FCN16 and FCN8, and use multiple layers of upsampling to merge the features from earlier convolution layers to have a more refined segmentation [137].
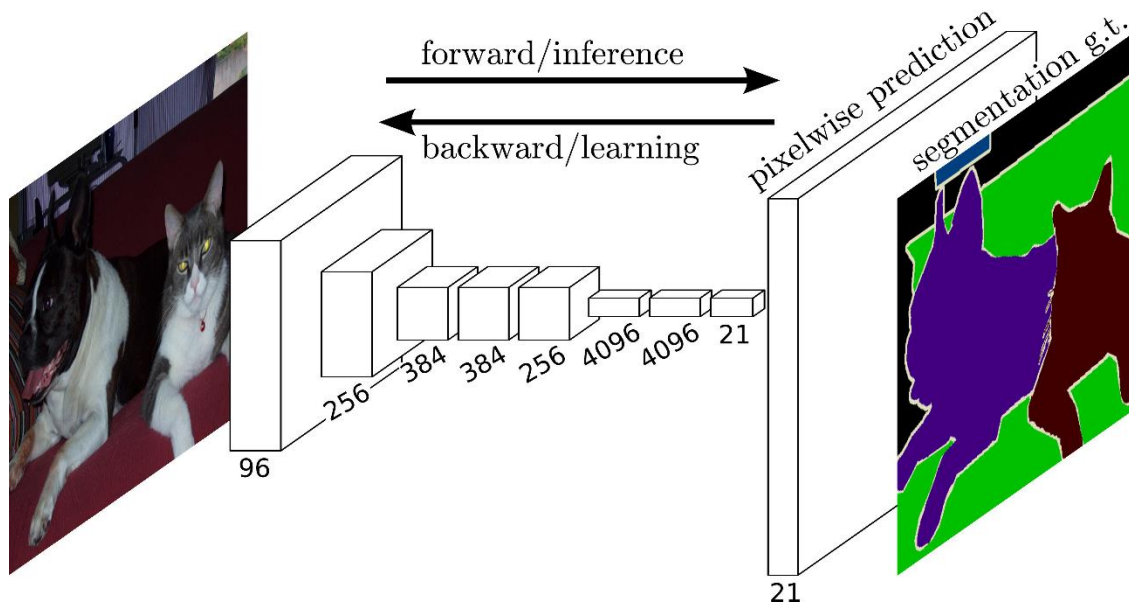
Figure 2-16: FCNN architecture showing process from input image (left) to the output semantic segmentation(right) [138].

Deep learning NN have shown impressive performance when they are trained on an important amount of data. An example of this are dataset trained using ImageNet, a set of thousand images of different classed with quality controlled and human annotated [139]. Several of the best models presently achieving an accuracy over 90 % using this ImageNet dataset. For example there is Model Soups with 90.94% [140] and DaViT-G with 90.4% [141] This why deep learning is consider the

state of the art for computer vision tasks it as shown remarkable performance for image classification and it is now extended to object detection and semantic segmentation.

2.4.2 CNN for object detection

Object detection is the combination of two common tasks in image analysis, object classification and object location. Indeed, given a list of class names and images with bounding boxes marked with the correct class identification for their training, the NN can learn to identify and mark the location of those objects in new images with high accuracy. The CNN is not limited to one class per training, it can be trained to detect a multitude of different classes [142]. There exist several architectures using different techniques for object detection, but generally, it works as follows. The network extracts the feature map using convolution layers and identifies the possible objects in the images. It then tries to classify what the object could be and gives its answer with a certain degree of confidence, going from 0 to 100%. The object is further localized using a bounding box. The bounding box information can be in different formats, but it is usually given with the following 4 values: the x,y coordinates of the center and width and height of the bounding box[143].

The performance of object detection models is commonly evaluated using average precision (AP) or the mean of the average precision (mAP). The AP is a common way to relate both precision and recall, which are two other performance metrics used in image processing that are based on the relevant information found (Figure 2-17). Precision describes how many segmented pixels are relevant to the application while recall describes how many relevant pixels are segmented. AP is the area under the precision-recall curve given by the integral in equation (10) [144]:

$$AP = \int_0^1 p(r)dr \qquad (10)$$

where p(r) is the precision expressed as a function of the dependent variable r, representing recall. The precision and recall are both computed from the numbers of true positive (TP), false positive (FP) and false negative (FN). A TP is a pixel of the reference object detected correctly as part of the object and a true negative (TN) is a pixel that is not part of the reference object and not detected as such by the NN. A FP is a pixel of the reference object detected incorrectly outside of the object and a FN is a pixel of the reference object that was not detected as such by the NN. With these

quantities, we can now measure precision and recall with the following equations (11) and (12)
[145]:

$$precision = \frac{TP}{TP+FP} \quad (11), \quad recall = \frac{TP}{TP+FN} \quad (12)$$
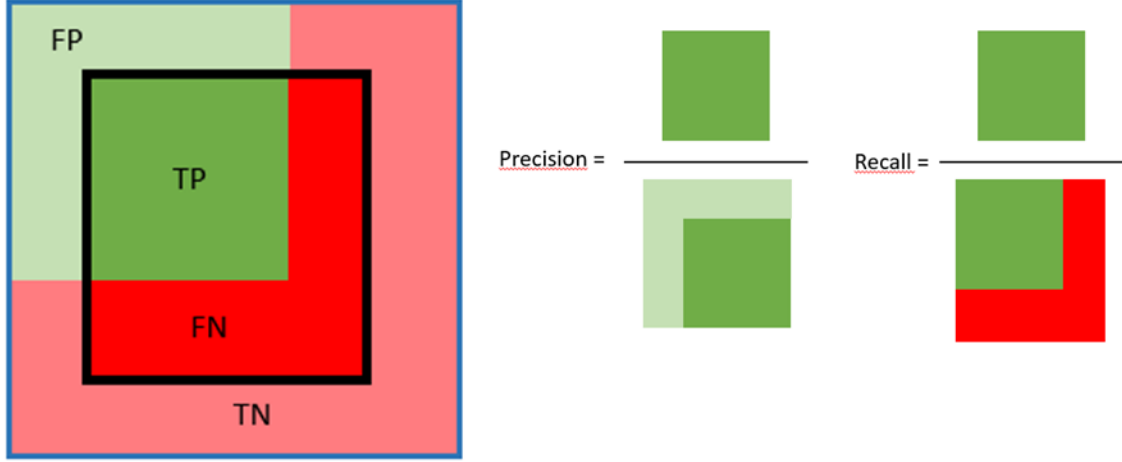
Figure 2-17: (left) outer blue rectangle is the frame of the full image and the inner black rectangle is the reference bounding box of the object to be detected in the image. The green shaded square corresponds to the bounding box actually detected by the model. TP are in dark green, FP in light green, FN are in dark red, and TN in pink. (right) fractions representing what precision and recall is computing.

However, the bounding box around an object can be subjective to the user. Thus, using metrics on a pixel-per-pixel basis is not necessarily adequate. Indeed, since two bounding boxes can be slightly shifted and still indicate the correct answer, another metric needs to be used: the intersection over union (IoU) (Figure 2-18) [143]. Like its name says, the IoU is the ratio of the intersection of the ground truth bounding box and the detected bounding box (corresponding to the number of TP pixels), to the union of both regions, (corresponding to the total number of TP, FN, and FP pixels) (equation 13):

$$IoU = \frac{TP}{TP+FN+FP} \quad (13)$$
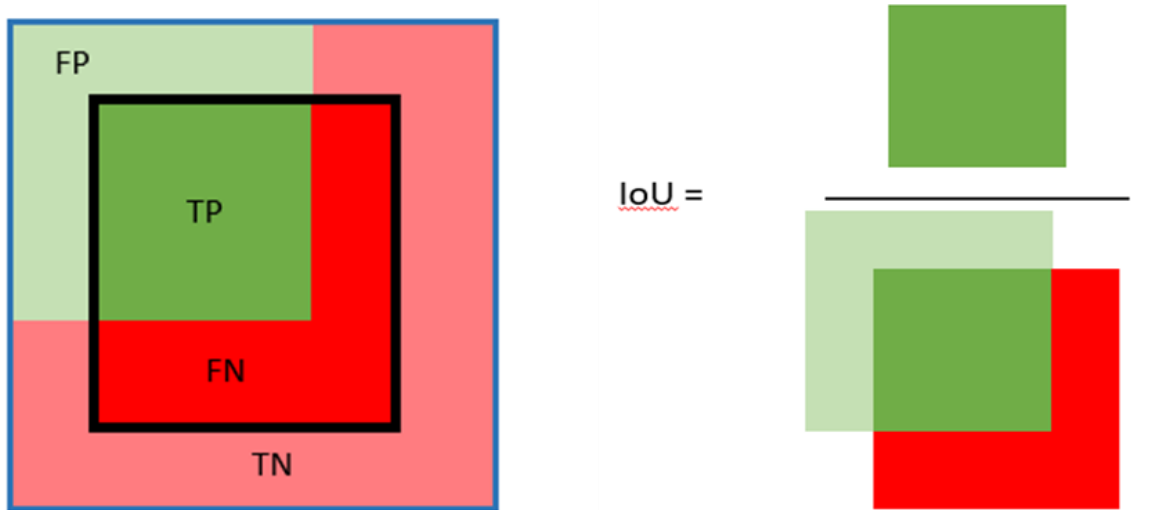
Figure 2-18: (left) outer blue rectangle is the frame of the full image and the inner black rectangle is the reference bounding box of the object to be detected in the image. The green shaded square corresponds to the bounding box actually detected by the model.. TP are in dark green, FP in light green, FN are in dark red, and TN in pink. (right) fraction representing what IoU is computing.

This metric ranges from zero to one, one being the perfect intersection between the two sections. Since the two bounding boxes might differ slightly and still be an excellent prediction, using an IoU threshold can be a relevant choice [146]. For example, if an IoU threshold is set to 0.5, only half the reference and detected bounding boxes need to intersect for the detected bounding box to be considered a TP detection. This way instead of comparing every pixel for the calculation of the precision and recall, every box can count as a TP, TN, FP, or FN detection, hence giving representation of the NN performance at the object level, instead of the pixel level.

Two major families of object detection algorithms are presently used: region-based CNN family and YOLO family. Region-based CNN can be split into 3 steps. First, there is the extraction of region proposals, which are around 2000 bounding boxes of potential objects. Second, the feature maps for the proposed regions are computed via convolution layers. Last, the regions are classified according to the list of possible objects learned [147]. This proposal process makes this CNN considerably slow. Therefore, it was improved into a faster-RCNN, which first computes the feature maps and then uses it to propose regions where there is possibly an object. This reduces considerably the number of proposals, therefore increasing the speed of the NN [148]. In contrast, CNN in the YOLO family works by first dividing the image into a grid with equally sized squares. Then, the cells are responsible for detecting an object and give a confidence score, which

determines how sure the NN is that there is an object inside. Moreover, the grid cells are also responsible to predict a class probability map, which is the probability of that region being part of a specific class given to the NN as input. Then, both are combined by multiplying the class probability and prediction confidence to give the class-specific confidence of the detected region [149]. The Yolo family has 3 major advantages over the R-CNN family. Firstly, the model is fast. Indeed, since the detection is processed as a regression problem, it performs bounding box prediction and object classification using a single convolution network. Secondly, it has a general vision of the image when making its predictions, which is not the case for region-based predictions. Lastly, YOLO is learning a more generalized representation of objects, therefore it does a better job when used in new domains, like micro-cracks detection [150].

2.4.3 FCNN for Semantic segmentation

Semantic segmentation is a much more complex process than object detection [151]. Instead of working on different regions of the image to detect the general location of objects, it provides a classification to every single pixel in the input image. Since the output has to be an image of the same size as the input, semantic segmentation has to be done by a FCNN [152].

Performance metrics for semantic segmentation are numerous. The most popular ones are accuracy (Figure 2-19), IoU, and Dice score (also called F1 score) (Figure 2-20). The pixel accuracy is the percentage of pixels correctly identified in the image (equation 14), where TP and TN rates are computed at the pixel level :

$$accuracy = \frac{TP}{TP+TN} \quad (14)$$
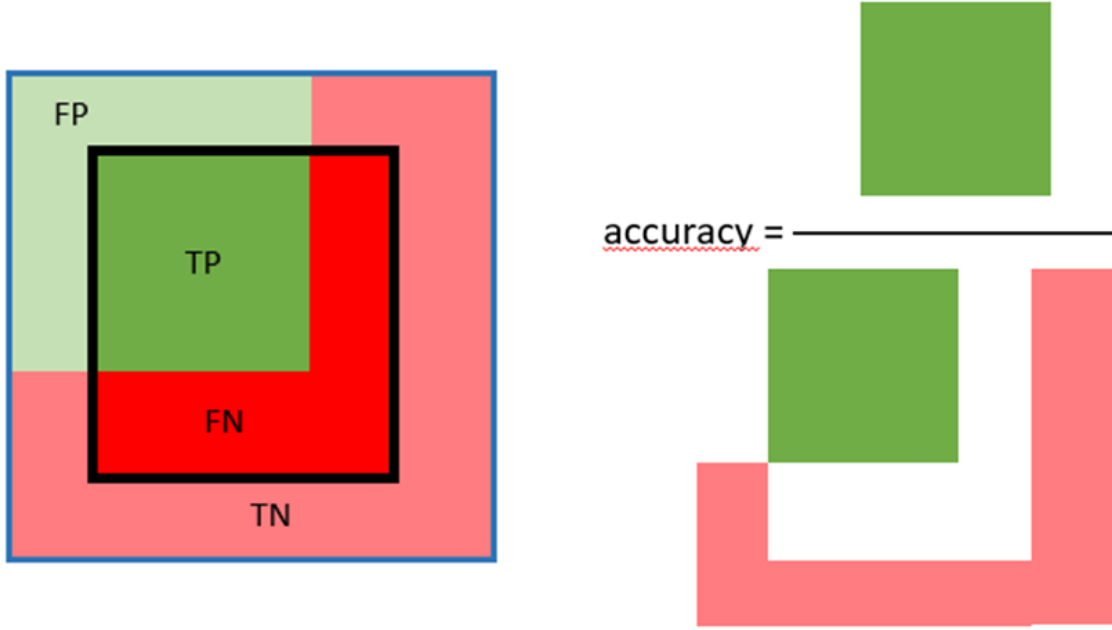
Figure 2-19: (left) outer blue rectangle is the frame of the full image and the inner black rectangle is the image to be segmented. TP are in dark green, FP in light green, FN are in dark red, and TN in pink. (right) fraction representing what accuracy is computing.

IoU was explained in the previous section as the percentage of intersection over union between two rectangular bounding boxes. In the context of semantic segmentation, there is no rectangular bounding boxes, the IoU is measured as the percentage of intersection per union of the reference segmentation and the segmentation provided by the NN. Dice score is another technique to measure the success of a segmentation (equation 15). However, while accuracy is used when the classes are balanced and when false negatives have not high impacts for the application, the Dice gives more importance to false negatives than accuracy [153].

$$Dice = \frac{2TP}{2TP+FP+FN} \quad (15)$$
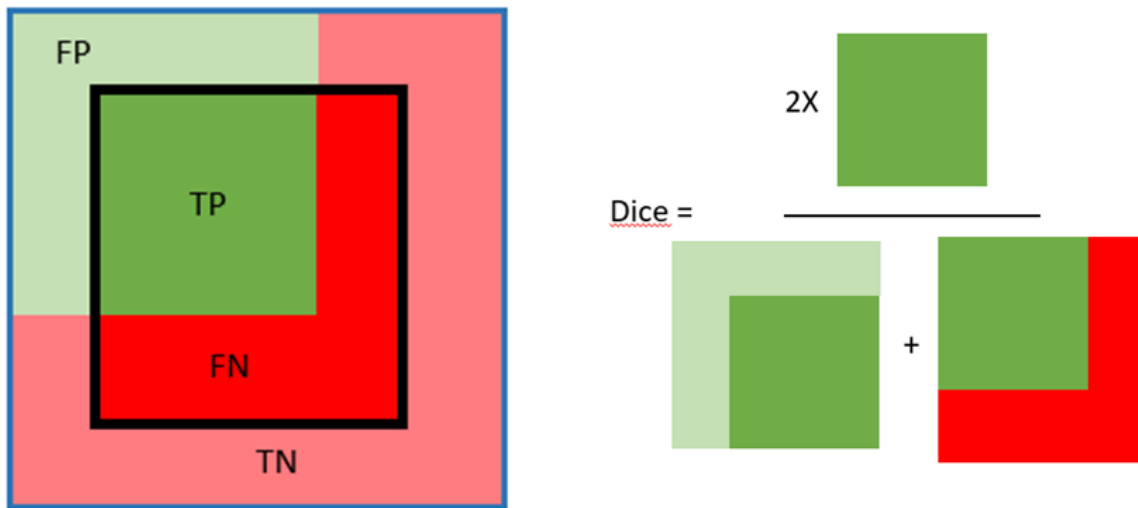
Figure 2-20 : (left) outer blue rectangle is the frame of the full image and the inner black rectangle is the image to be segmented. TP are in dark green, FP in light green, FN are in dark red, and TN in pink. (right) fraction representing what Dice score is computing.

The most commonly used FCN in biomedical applications is the Unet. It was proven to perform well even with small annotated datasets, which is often the case when working with biomedical images. The network gets its name from the shape of its architecture (Figure 2-21). The symmetric structure is composed of a contracting branch on the left and an expanding one on the right. The left path is like the typical CNN with a series of convolution and pooling layers. In contrast, the right path includes one deconvolution layer for every pooling layer in the contracting branch. Moreover, after every deconvolution, the feature maps from the contracting path are copied to avoid the loss of features [154]. The contracting branch allows the extraction of features, answering the questions "what's in the image", whereas the expanding branch allows for the localization of the features in the image, answering the question "where are these features present in the image".
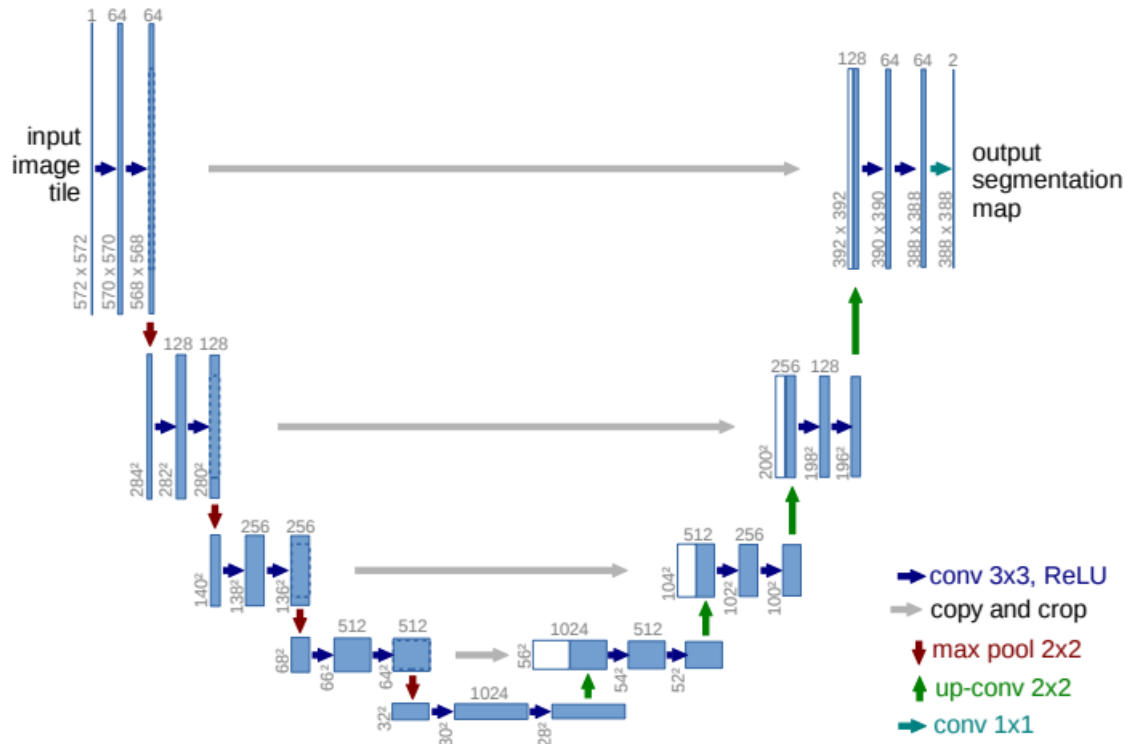
Figure 2-21: Unet architecture where each blue boxes are features map and whites boxes are copied feature maps. The arrows show the flow of the forward passing [154].

2.4.4 Application for damage segmentation

To our knowledge, deep learning semantic segmentation has never been applied to bone microdamage segmentation in microCT images. However, the topic is popular for infrastructure maintenance using drone pictures [155-159]. There are even examples of more typical engineering material, such as iron ore pellets, scanned in a microCT scanner [160].

Structures like roads and bridges have their pictures taken using different techniques, one of them using drones to reduce human labor. Then the pictures are used to train and test neural networks for the segmentation of cracks in concrete or asphalt [155, 156]. There is even an open source dataset to compare the performance of new deep learning models in the same conditions [161]. This kind of collaboration gives the opportunity to develop models specialized for damage segmentation, by either modifying existing models, like Unet [157-159], or by developing new custom networks [162, 163]. More recently, a two steps method was developed by combining object detection and semantic segmentation to improve the models both in accuracy and processing

time [164, 165]. These models have shown interesting results with the ability to differentiate between cracks and crack-like features (Figure 2-22).

Figure 2-22: region based object detection(left) and semantic segmentation focused inside the detection regions (right) [165]

In contrast, drone pictures are completely different from bone microCT images, which have different sources of noise and a different color spectrum. The studies using deep learning for damage segmentation in microCT images are more limited than pavement maintenance, but there are still some examples in the literature [166, 167]. One is even showing success in a porous material, more precisely iron ore pellets [160]. However, materials studied in these papers are still much less porous than trabecular bone and their structures are not as complex. Moreover, there is no trained NN or open-source dataset on which to train and test new NN for bone microdamage, making the application difficult to explore.

2.5   Digital Volume Correlation

Strain can be measured in 2D in one or multiple planes using strain gauges or extensometers. These techniques are however limited to surface strain and the overall strain of the sample. In a complex architecture like trabecular bone, in which the microarchitecture is anisotropic, the deformation is not equally distributed [168]. It is then impossible to measure the strain map inside the sample using these methods. This is why a method called digital image correlation (DIC) was developed in the early 1980, allowing to measure displacements of the internal structure [169, 170]. 2D images at different stages of the sample deformation can be compared to each other and groups of pixels

are tracked across them (Figure 2-23). To track subdivisions of pixels, different correlation functions are used[171], making it possible to track axial and shear strain separately[172]. Hence, the algorithm can measure the 2D vector field of displacement and strain inside the sample and map them[173]. The results are graphically represented using a colour legend, correlating displacement or strain magnitude to a colour. Generally, the region of high displacement will be represented by red pixel and the region of low displacement will be represented by blue pixel. However, it is not a strict rule and other colour legend can be used, as long as they have a range of colour big enough to give in detail the different displacement values in each subset.
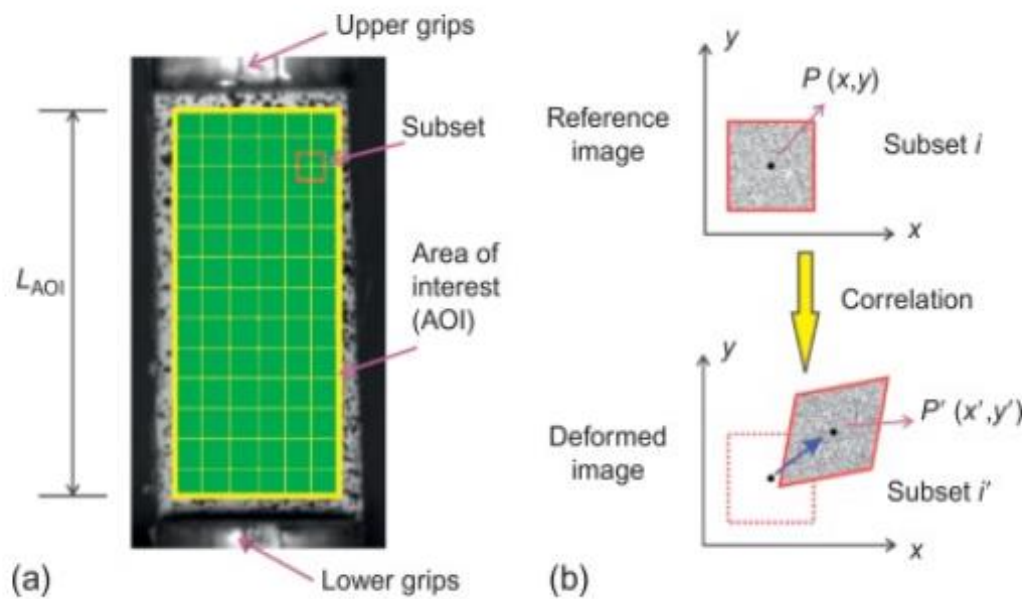
Figure 2-23: (a) RoI showed by the green area. Subsets of pixels separated by the yellow boxes. (b) Showing the correlation computation between a single subset of pixels between unloaded and loaded images[171].

DIC method has the limitation of being of 2D approach providing a limited evaluation of the displacement inside a sample volume. This is where digital volume correlation (DVC) comes into play. This technique is similar to DIC but works in 3D. The algorithm uses cubic subpixels groups instead of squared ones like in DIC and gives a 3D strain map(Figure 2-24)[102]. This relatively new technique opens new opportunities to study the fractures mechanisms and load distribution in the complex microarchitecture of the trabecular bone[10, 174-176].
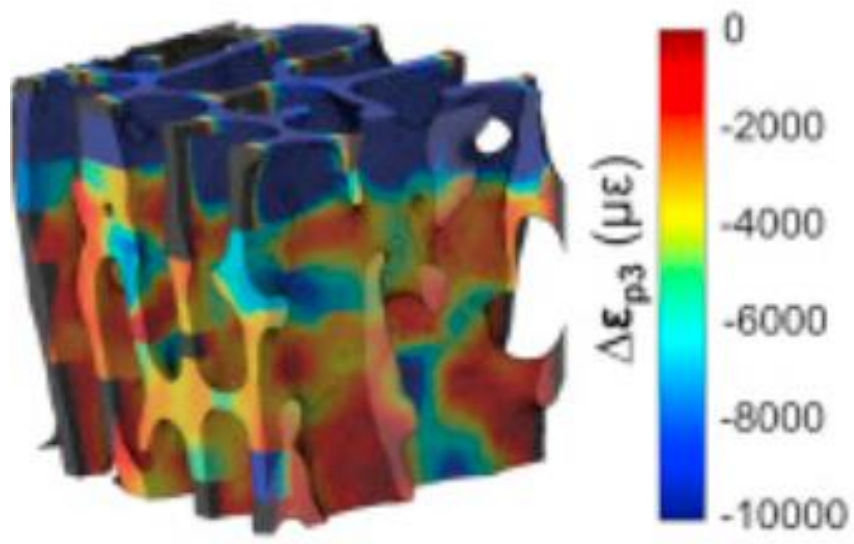
Figure 2-24: 3D strain map of a trabecular bone sample[177].

CHAPTER 3   PROJECT RATIONALE

Following the literature review, the project rationale can be summarized as follows:

- Osteoporosis affects bone differently depending on the stage of the disease. Being a silent disease, understanding the changes in mechanical properties in early stages of the disease could help diagnose symptoms early and prevent severe fractures. Since trabecular bone is more affected in early stages, it would be a logical choice to study its mechanical behavior for future diagnostic technology.

- Contrast agents are commonly used for bone microdamage evaluation. Generally, they only give an approximation of the microdamage volume, and they can also require a long staining process. Moreover, they often can be toxic since they use heavy metal for Xray absorption. Therefore, a replacement for contrast agent could make the process more accurate, less labor intensive and safer.

- Damage segmentation, using deep learning, is widely used in pavement maintenance using drone pictures and provides very good accuracy. While bone is a more porous material, cracks still have features different than other bone structures and can be differentiated from the other features.

- Damage accumulation could be tracked through increasing loading using deep learning and give the opportunity to track the damage accumulation through multiple loading.

- Bone mechanical properties, such as Young's modulus, can be characterized from mechanical testing.

- Digital volume correlation allows visualizing 3D strain maps inside the bone sample. To do so, several increments of displacement are applied to the sample and microCT imaging is completed at each increment. This method is used to investigate fracture mechanics in bone samples.

There is currently no study simultaneously combining damage quantification, mechanical properties, and 3D strain map. Therefore, current experimental procedures do not include all the information about the mechanical behavior of bone samples. Using this project to develop an ex vivo 3D experimental platform to study all three components could open the possibility to draw

new information about the bone mechanical behavior and help in the development of future diagnostic technologies. Moreover, using deep learning give the opportunity to track the damage accumulation through multiple loading and avoid the use of contrast agents.

3.1 Main objective

The main objective of this project was to develop a 3D *ex vivo* experimental platform to identify the relationship between microdamage, strain patterns and mechanical properties in trabecular bone samples under quasi-static compression loading.

3.2 Specific objectives (SO)

1. Develop an imaging procedure of trabecular bone samples using the Xray microCT scanner (Zeiss Xradia 520 versa).
2. Develop a sample preparation and mechanical testing procedure to be used inside the microCT scanner that can evaluate bone samples mechanical properties.
3. Develop a method for the evaluation of bone microdamage using a deep learning algorithm.
4. Develop a method to map the 3D internal displacement

3.3 Research Questions

This project aims to answer the following research questions:

- What is the potential of deep learning algorithms in the evaluation of bone microdamage in trabecular bone samples?
- What additional information can be drawn by including digital volume correlation in the study of bone microdamage quantification vs mechanical properties?

3.4 Thesis organization

This thesis is divided into seven chapters. It begins with an Introduction in Chapter 1, followed by a literature review of bone properties, Xray imaging, bone microdamage, deep learning and DVC in Chapter 2. Chapter 3 explains the project rationale as well as the main and specific objectives of the project. Chapter 4 includes a scientific article presenting the feasibility of deep learning for

bone damage quantification. Chapter 5 introduces a complementary study presenting the results of a DVC algorithm. Chapter 6 covers the general discussion. Lastly, Chapter 7 concludes on the key points of the project and explores future ideas for the continuation of this research.

CHAPTER 4   ARTICLE 1: SEGMENTATION OF TRABECULAR BONE MICRODAMAGE IN XRAY MICROCT IMAGES USING A TWO-STEP DEEP LEARNING METHOD

Authors

Rodrigue Caron[1,2], Irène Londono[2], Lama Seoud[2,3,4], Isabelle Villemure [1,2,3]

[1] Department of Mechanical Engineering, Polytechnique Montréal, Montréal, QC, Canada

[2] Centre de recherche du CHU Sainte Justine, CHU Sainte Justine, Montréal, QC, Canada

[3] Institut de génie biomédical, Montréal, QC, Canada

[4] Department of Computer Engineering and Software Engineering, Polytechnique Montréal, Montréal, QC, Canada

The article presented in this chapter shows the potential of using a two-steps segmentation tecniques for the evalution of bone microdamage in microCT images. This two-steps method involves YOLOv4, an object detection NN, and Unet, a semantic segmentation NN. This article answers the SO1 and SO3 presented in Chapter 3. The article was submitted on May 5th 2022 for the Journal of the Mechanical Behavior of Biomedical Materials.

Abstract

Introduction: One of the current approaches to improve our understanding of osteoporosis is to study the development of bone microdamage under mechanical loading. The current practice for evaluating bone microdamage is to quantify damage volume from images of bone samples stained with a contrast agent, often composed of toxic heavy metals and requiring long tissue preparation. This work aims to evaluate the potential of linear microcracks detection and segmentation in trabecular bone samples using well-known deep learning models, namely YOLOv4 and Unet, applied on microCT images.

Methods: Six trabecular bovine bone cylinders underwent compression until ultimate stress and were subsequently imaged with a microCT at a resolution of 1.95 um. Two of these samples (samples 1 and 2) were then stained using barium sulfate ($BaSO_4$) and imaged again. The unstained samples (samples 3-6) were used to train two neural networks YOLOv4 to detect regions with microdamage further combined with Unet to segment the microdamage at the pixel level in the detected regions. Four different model versions of YOLOv4 were compared using the average Intersection over Union (IoU) and the mean average precision (mAP). The performance of Unet was also measured using two segmentation metrics, the Dice Score and the Intersection over Union (IoU). A qualitative comparison was finally done between the deep learning and the contrast agent approaches.

Results: Among the four versions of YOLOv4, the YOLOv4p5 model resulted in the best performance with an average IoU of 45,32% and 51,12% and a mAP of 28.79% and 46.22%, respectively for samples 1 and 2. The segmentation perfomance of Unet provided better IoU and DICE score on sample 2 compared to sample 1. The poorer performance of the test on sample 1 could be explained by its poorer contrast to noise ratio (CNR). Indeed, sample 1 resulted in a CNR of 7,96, which was worse than the average CNR in the training samples, while sample 2 resulted in a CNR of 10,08. The qualitative comparison between the contrast agent and the deep learning segmentation showed that two different regions were segmented by the two techniques. Deep learning is segmenting the region inside the cracks while the contrast agent segments the region around it or even regions with no visible damage.

Conclusion: The combination of YOLOv4 for microdamage detection with Unet for damage segmentation showed a potential for the detection and segmentation of microdamage in trabecular bone. The accuracy of both neural networks achieved in this work is acceptable considering it is their first application in this specific field and the amount of data was limited. Even if the errors from both neural networks are accumulated, the two-steps approach is faster than the semantic segmentation of the whole volume.

4.1 Introduction

Over 200 million people in the world are affected by osteoporosis, including 33% women over 50 years old and 20% men during their lifetime (Sözen el al., 2017). In Canada, there were an estimated 2.2 million people over 40 years old suffering from osteoporosis in 2015-2016 (Canada, 2021) and an estimated 10.2 million people over 50 years old in the United States in 2010 (Wright et al., 2014). Both represent about 10% of their respective demographic. The pathology is characterized by a reduction in bone density and degradation in bone micro-architecture, leading to an increased risk of fracture for the diseased (Tu et al., 2018). Unfortunately, current knowledge does not allow the early detection of the disease. Indeed, because of the absence of symptoms before fracture, it is considered a silent disease (Lems & Raterman, 2017). Moreover, fractures can have catastrophic consequences in older patients (Gagnon & Lafrance, 2011). However, new research on bone tissue has led to a better understanding of the fracture mechanisms (Donahue & Galley, 2006; Presbítero et al., 2017).

Bone microdamage analysis can be used to infer on bone quality. The accumulation of microdamage in bone leads to the reduction of its mechanical properties, such as bone rigidity (Donahue & Galley, 2006). Studying the relationship between bone microdamage and mechanical properties helps advance knowledge on osteoporosis (Presbítero et al., 2017). Current practices often use mechanical loading to induce microdamage in bone samples and further study the relationship between different physical and mechanical properties, such as bone density, rigidity, bone morphological parameters and microdamage (Nagaraja et al., 2005; Tang & Vashishth, 2007; X. Wang et al., 2007). The presence of bone microcracks was first reported by Frost (Frost, 1960). Since then, two types of microdamage were identified: linear microcracks and diffuse damage. The first is similar to a typical engineer crack but at the micrometer level, and the latter is a cluster of very small cracks at a sub lamellar size (Seref-Ferlengez et al., 2015). They are believed to have different roles in bone mechanical properties and remodeling (Herman et al., 2010).

Several years after the discovery of microdamage, protocols were developed to study bone microdamage by staining samples with a contrast agent and imaging them using 2D imaging techniques (Burr & Stafford, 1990). However, they came with their set of limitations, since they only provided information about the microdamage structure in 2D and required samples destruction. More recently, imaging protocols using Xray microCT scanner have been developed

to study bone microdamage in 3D. These techniques allowed quantifying the accumulated damage volume using Xray absorbent contrast agent during *in vitro* or *ex vivo* loading (Turnbull et al., 2011; X. Wang et al., 2007; X. Zhang et al., 2018).

While the use of contrast agents makes it possible to visualize areas of microcracks and diffuse damage, which would normally be smaller than the image resolution, it also has its drawback. The microdamage can be internal to the bone tissue, preventing the contrast agent to penetrate microcracks that are not connected to the surface area of the bone. Moreover, the agent can stain more than the microdamage itself. Indeed, it can also penetrate bone microstructure, like lacunae, and mark them as microdamage (Landrigan et al., 2011; Leng et al., 2008). Also, in the case of cortical (or compact) bone samples, the agent might have more problems penetrating the sample (Presbitero et al., 2019). Lastly, the bulk staining period can be long and this method mostly use heavy metals, which can be toxic to human and aquatic life (Leng et al., 2006).

A recent technique to identify and quantify microdamage is semantic segmentation using deep learning (L. Zhang et al., 2016). Although deep learning is used for bone fracture detection in clinical settings (Lindsey et al., 2018), the literature does not show prior usage of semantic segmentation for bone microdamage. Deep learning is commonly used in construction and maintenance to optimize manual inspection. Structures made of concrete, asphalt or similar material, which require frequent maintenance, are photographed using drones and pictures are further analyzed using a deep learning model (Jiang et al., 2020; Munawar et al., 2022). Neural networks (NN) can even be specifically modeled for pavement crack segmentation (Y. Liu et al., 2019; A. Zhang et al., 2018) or they can be based on existing models, which can be optimized for crack segmentation (F. Liu & Wang, 2022; L. Wang et al., 2020; Lingxin Zhang et al., 2021). Crack segmentation using deep learning could be applied to the detection of bone microdamage. Indeed, with the improvement of microCT imaging to a resolution at a sub-micron level (Coulombe et al., 2022; T. Zhang et al.), there is a potential for the detection of microdamage using a deep learning model. The closest application of deep learning for microcracks in trabecular bone aimed at classifying cracks for fracture mechanics but not at segmentating them (Shen et al., 2021).

However, deep learning based segmentation comes with its own set of limitations for applications on trabecular bone microCT images. Firstly, in contrast with pavement drone pictures commonly used in deep learning segmentation, the background of trabecular bone is not uniform. Indeed,

pavement made of asphalt or concrete has little to no visible pores (Chen et al., 2021), making it easier to detect cracks compared to trabecular bone, a highly porous material with background of grey intensity similar to cracks (Toppets et al., 2004). Even though deep learning segmentation of cracks was done on microCT images of iron ore pellets, the pores were generally small and circular and did not compose most of the background like in trabecular bone (Bezerra et al., 2020). Secondly, microCT imaging at high resolution can be challenging by itself. Since it requires smaller objectives, a longer exposition time must be used to have a sufficiently low noise level in order to have proper contrast between bone and cracks (Alsamadony et al., 2021; Chen et al., 2021; Heyndrickx et al., 2020), making the process of collecting a sufficient amount of data expensive, both in scan time and image processing time. The performance of a convolutional NN is highly dependent on the amount of data used during training. In machine learning, there is normally an open-access dataset that can be used to train and benchmark a new NN (Lin et al., 2014; Shi et al., 2016). This is not the case for bone microdamage, making it difficult to have a performing NN with a small dataset. Because of the limitations listed above, a simple semantic segmentation would not be sufficient for bone micro damage, and a more robust approach should be developed to properly demonstrate the potential of deep learning segmentation. In the literature, a two-step deep learning approach for crack segmentation was developed to improve the performance (Chen et al., 2021; Feng et al., 2020; Huang et al., 2022; Kalfarisi et al., 2020; J. Liu et al., 2020; X. Zhang et al., 2019). The first step consists in detecting the region of interest containing the cracks with an object detection NN and the second is the semantic segmentation, classification of pixels, of the cracks inside the region of interest using a segmentation NN. The bounding boxes (first step) are used as masks for the second step, hence limiting the searching areas for the semantic segmentation NN. This two-step approach reduces errors associated with the step of segmentation NN. It also improves the detection speed and reduces the segmentation of crack-like features, which could be erroneously segmented using semantic segmentation only , since it is a much more complex process (J. Liu et al., 2020). In addition, a network like Unet is an excellent starting point for this work since it is designed to work in biomedical applications using imaging techniques like Xray or MRI. It uses integrated data augmentation to compensate for the smaller datasets (Ronneberger et al., 2015).

This work aims to evaluate the potential of linear microcracks detection and segmentation in trabecular bone samples using well-known deep learning models, namely YOLOv4 and Unet. More specifically, the work presented in this paper has the following contributions:

1. Two-step segmentation of linear microcracks using two consecutive CNN models: Darknet YOLOv4 for the detection of regions with cracks, each region being defined by a bounding box, and then a Unet for the segmentation of the cracks inside the pre-defined bounding boxes, as opposed to the whole image. This approach allows to increase the segmentation speed and to reduce the false segmentation of structures similar to microcracks.
2. Quantitative performance analysis of both models, taken individually and further combined.
3. Inter-user comparison of reference segmentation, to evaluate the impact of human error, and computation of the datasets as well as contrast to Noise ratio (CNR) analysis to evaluate impacts of image quality.
4. Qualitative comparison of the deep learning segmentation method with the contrast agent method, considered as the gold standard.

4.2   Dataset preparation

Deep learning, in its supervised form, requires a large amount of data to train a model. Usually publicly available very large datasets are used to this end. However, in the context of this study, deep learning is applied in a niche field where no domain-specific dataset exists. Therefore, the first step of this study was to build a dataset, i.e. bone samples with mechanically created microdamage, to train and test our models.

4.2.1 Sample preparation

Six trabecular bone cylinders of 8.3 mm in diameter were extracted from bovine tail vertebrae using a diamond core drill (Diamon Production, Canada) mounted on a drill press. The core drill was kept under constant irrigation with distilled water to reduce the heat created by the cut (Kogawa et al., 2018). The six samples were cut at a length of 7 mm using an isoMet 1000 (Buehler, Illinois) at a speed of 250 rpm. Obtained cylindrical samples had their bone marrow removed in two steps. First, most of the marrow was removed using a Waterpik flosser (Waterpik, Colorado) while samples were submerged in distilled water. Secondly, the remaining marrow was removed using a 15 minutes ultrasonic bath at 20 kHz, while kept on ice to avoid reaching high temperature. Samples were further stored in saline solution and frozen at -20 C^o until mechanical loading (Belda et al., 2020; Green et al., 2011).

4.2.2 Mechanical test

Quasi-static compression loading was carried out on each bone cylinder. To do so, the sample was thawed out overnight at 4 °C the day before mechanical testing. The sample was then fixed inside a Deben micro tensile testing system (Deben, UK), following measurement of its thickness and diameter. Following a preload of 20 N, the samples were loaded at a rate of 0,5 mm/min until the force-displacement curve reached the ultimate stress, before the failure of the sample. The procedure ensured enough damage for image analysis without the complete failure of the bone microarchitecture. After loading, the samples were removed from the testing system and rested for at least 30 minutes before being imaged (Nagaraja et al., 2005; Tang & Vashishth, 2007; X. Wang et al., 2007).

4.2.3 Contrast agent and imaging

The samples were split into two groups: the testing group (samples 1 and 2) and the training group (samples 3 to 6). Both groups were initially imaged with a microCT scanner (Xradia 520 Versa, Zeiss, Germany) at a resolution of 1.95 μm with a FOV of 3.95 mm^3. The source was set at a voltage of 60kV and a power of 5W, giving a current of 83.9 uA. Imaging was done on 3201 rotations with an exposition time of 4 seconds. The two testing samples were subsequently stained with barium sulfate following the procedure given by Wang (X. Wang et al., 2007). To do so, samples were submerged under vacuum for 48 hours in a solution of 0.5M $BaCl_2$ then switched to a solution of 0.5M $NaSO_4$ for 48 hours under vacuum. After staining, these two samples were imaged again with the same microCT parameters. The zone where the first images were taken was relocated using the image analysis software Dragonfly (Object research systems, Canada) and the coordinates were imported in the Zeiss software for the microCT scanner.

For all samples, a sub-group of images were randomly selected in the plane transverse to the loading axis (plane xz), corresponding to about 10% of the images in that plane. The number of images extracted per sample varied depending on the amount of damage accumulated in the sample volume. Images with and without damage were included in the dataset. The training dataset was composed of all the images extracted from the four training samples (735 images), and the testing dataset was composed of all the images extracted from the two testing samples (349 images).

4.3 Methods

4.3.1 Data annotation

All images were manually annotated by one trained operator (user 1) at two levels (Figure 4-1). At the global level the bounding boxes were identified for YOLOv4 (Figure 4-1A). For each image, a text file containing the information about the bounding boxes was saved, with each line containing the information of a bounding box. It included the corresponding class, center's x and y coordinates, box's width and height. At local level, DragonFLy was used for the manual segmentation of the linear microcracks' pixels, inside the bounding boxes, for Unet (Figure 4-1B). Three classes were considered in the segmentation: background, bone and linear microcracks.

The annotations performed by user 1 were considered as the reference for training and testing the models. A second user (user 2) provided manual segmentations at the pixel level for the images in the testing sub-group. This second set of annotations was not used to train nor to test the models, but to evaluate the inter-operator variability in terms of Intersection of Union (IoU) and Dice score:

$$IoU = \frac{|A \cap B|}{|A \cup B|} \qquad Dice\ score = \frac{2*|A \cap B|}{|A|+|B|},$$

where A and B are two different segmented regions.
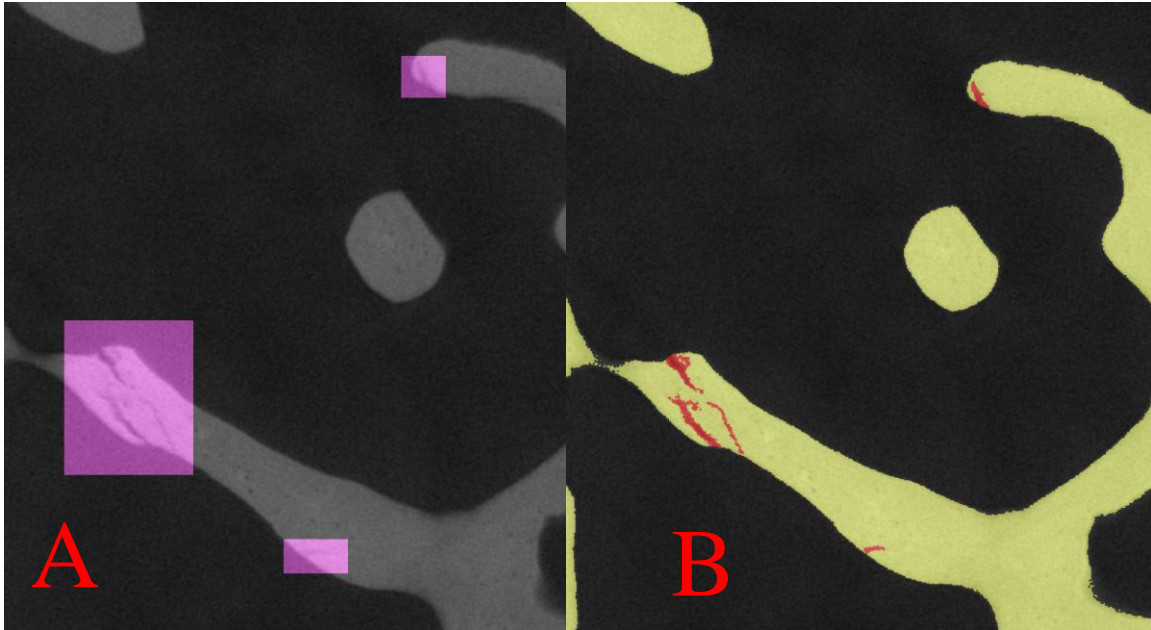
Figure 4-1 : Reference segmentation for both NN models. (A) Bounding boxes (in pink) englobing regions with micro-cracks and (B) segmentation of pixels inside the cracks themselves (in red).

4.3.2 Training and testing

The computer used in this study was equipped with a Geforce RTX 2070 super-8GB of VRAM,32 GB of RAM and a ryzen 7 2700x. YOLOv4 and Unet were trained and tested on two different platforms.

YOLOv4 implemented with the Darknet framework is an open-source code using primarily C and CUDA with a python interface (Bochkovski et al., 2020). The NN can do both image classification and detection. In this study, it was used for the detection of objects. To counter the disadvantages of having a small training dataset, data augmentation strategy was used as an artificial way to enlarge the training set by slightly modifying the images (Shorten & Khoshgoftaar, 2019). Saturation, brightness, hue, Gaussian noise and mosaic data augmentation were more precisely used for the training of the detection model. In addition, four versions of YOLOv4 were tested: the base model, a slightly modified model for smaller object detection, the base model with additional geometric data augmentation using an open-source python library called imgaug and a scaled model with bigger resolution and more layers. For training, a batch size of 64 was used with a maximum number of batch set at 6000, as recommended by the creator of the model for a data set with only one class (Bochkovskiy et al., 2020). The scaled model used was more precisely

YOLOv4-p5, since bigger models were too expensive on video RAM for this study. As for the test metric, average IoU and mean average precision (mAP) were used to evaluate the performance.

Unet was trained using DragonFly implementation of the model. In both training and testing, the YOLO reference bounding boxes were used as a mask for the training and testing of Unet, making the process much faster and giving the opportunity to use more data augmentation. Unet tests were evaluated using the Dice score and IoU metrics, which were computed using the image processing software DragonFly (ORS, Montreal, Canada).

The combination of YOLOV4 and Unet was also evaluated using DragonFly. The YOLOv4 output bounding boxes were used as a mask for the Unet evaluation test. Once again, the Dice score and IoU were used as metrics. Figure 4-2 shows a schematic of the different results evaluated during the testing phase of this study.
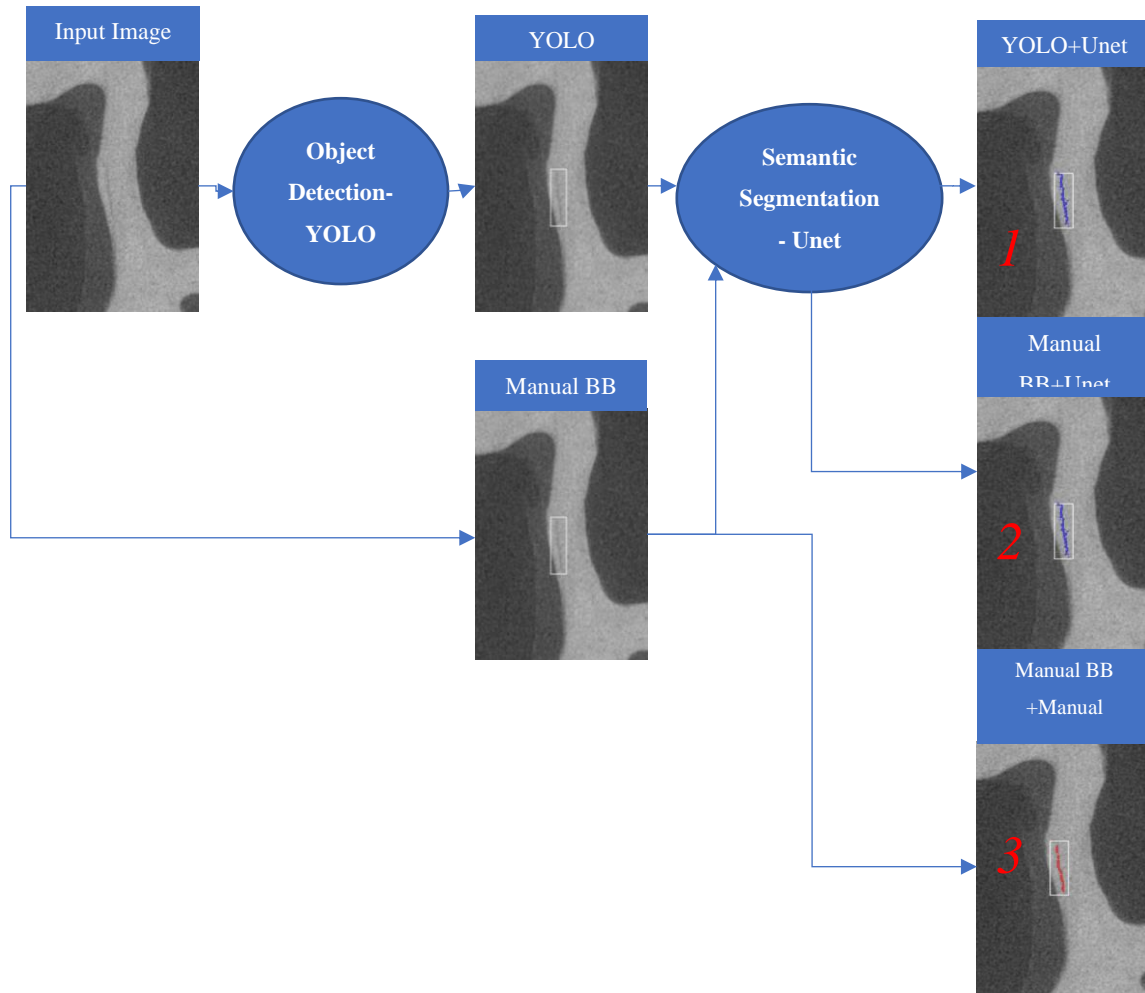
Figure 4-2: Schematic of the all the results related to NN training and testing included in this study. The input image is going through three paths: 1) the fully automatic path: YOLO detects the cracks using bounding boxes and then this output is used as an input for Unet to segment the pixels inside the crack; 2) the semi-automatic path: the cracks are manually segmented using bounding boxes (BB) and then this output is used as an input for Unet to segment the pixels inside the crack; 3) the fully manual path: the bounding boxes and the pixels are manually segmented. This third path is used to evaluate the two other methods.

4.4   Results

4.4.1 Microcracks detection

Table 1 summarizes the performance obtained with the four YOLOv4 models for the two testing samples using the two metrics. The best performance was obtained with YOLOv4p5, with an average IoU of 45,32 % and a mAP of 28.79% for Sample 1 and an average IoU of 51.12 % and a mAP of 46.22% for Sample 2.

Table 1: Performance of the different YoloV4 models, based on the resulting Average IoU and mAP. The bolded text shows the best result for each metric and each sample.

Model name	Test set	Average IoU (%)	mAP (%)
YOLOv4	Sample1	43,21	22,71
	Sample2	47,36	46,02
YOLOv4p5	Sample 1	**45,32**	**28,79**
	Sample 2	**51,12**	**46,22**
YOLOv4 with imgaug	Sample 1	37,62	23,01
	Sample 2	39,82	28,63
YOLOv4 for small obj.	Sample 1	42,49	25,11
	Sample 2	45,95	34,7

4.4.2 Microcracks segmentation

Table 2 shows the performance of Unet combined with manually annotated bounding boxes as a mask and of Unet combined with bounding boxes obtained from Yolov4-p5. There is an important reduction in both IoU and Dice for Unet used with YOLO compared to Unet used with manual BB, probably because of the accumulation of mistakes done by both NN.

Table 2: Performance of Unet using manually annotated bounding boxes as a mask and using the output of the detection model as a mask

Models	dataset	IoU (%)	DICE (%)
Manual BB + Unet	Sample 1	50,11	66,77
	Sample 2	70,73	82,85
Yolov4p5 + Unet	Sample 1	26,05	41,34
	Sample 2	58,21	73,58

4.4.3 Inter-operator variability in manual microcracks segmentation

Table 3 gives a comparison between the microcracks manual segmentations provided by user 1 and user 2 on the testing group. It shows that the difference between both users' segmentation is greater for Sample 1 than for Sample 2.

Table 3 : Inter-user comparison between the Unet's reference segmentation (user 1) used in this study and another user outside of this study (user 2). The scores are given as the performance of user 2 segmentation compared to user 1.

	IOU (%)	DICE (%)
Sample 1	47,47	64,38
Sample 2	69,18	81,79

Tables 1, 2 and 3 all showed a difference in performance between Sample 1 and Sample 2 in all metrics. Therefore, further investigation of image quality was completed. Table 4 shows the CNR of all samples for both the testing and training groups. It shows that the CNR of Sample 1 is lower than the ones of the other samples and that Sample 2 has a similar CNR to the ones from the training group (average of 9.63). Furthermore, Sample 2 has the highest CNR overall.

Table 4: Contrast to noise ratio (CNR) of every samples in both the training and testing groups.

	CNR
Testing group	
Sample 1	7,96
Sample 2	10,08
Training group	
Sample 3	9,97
Sample 4	9,81
Sample 5	9,06
Sample 6	9,66

4.4.4 Qualitative analysis

The qualitative analysis includes examples of good and poor segmentations (Figures 4-3 and 4-4). The white rectangles represent the bounding boxes detected by YOLOv4p5 as containing cracks.

The blue pixels correspond to cracks automatically segmented by the Unet model while the red pixels correspond to manually annotated cracks. Purple pixels are simply the overlapping regions between both segmentations. Figure 4-3 is an example of a good segmentation (in Sample 2) with mostly purple pixels.
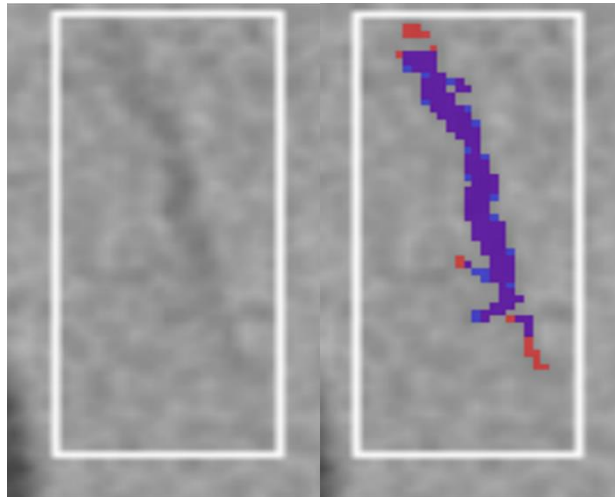
Figure 4-3: (Left) Results from Yolov4p5 before applying Unet on the images. (Right) Results from the two-step technique tested on Sample 2: The white box is YOLOv5 resulting bounding box, blue pixels are the Unet segmentation, red pixels are the manual reference and purple pixels are the overlapping regions between both colours.

Figure 4-4 shows an example of a poor segmentation (in Sample 1). In this example, the white bounding box detected by YOLOv4 does not include the entire crack. This means that Unet cannot possibly match the reference segmentation, since it is limited to the region in the bounding box. Moreover, even inside the box, the blue segmentation provided by the Unet is missing a good portion of the annotated crack.
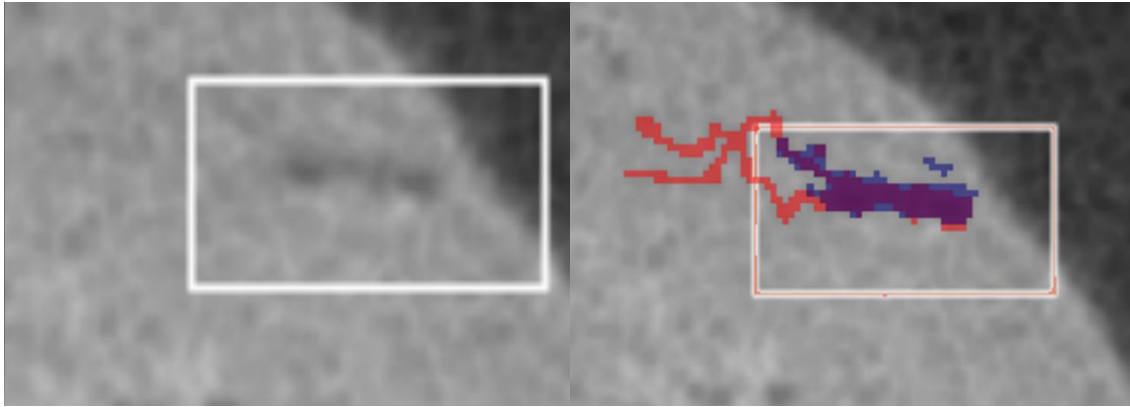
Figure 4-4: (Left) Result from Yolov4p5 before applying Unet on the images. (Right) Results example from the two-step technique tested on sample 1, where the white box is YOLOv5 resulting bounding box, blue is Unet segmentation , red pixels are the manual reference and purple is the overlapping region between both colours.

Poor segmentation can also be obtained when YOLOv4 falsely detects a very large region as containing a micro-crack. One such example is provided in Figure 4-5. In this case, the Unet has a larger search area and has a higher chance to detect pores as microdamage. Although, the Unet is still performant in differentiating between pores and cracks, there is some false positive in the boxes when the pores are not completely circular or a little bigger than average, as shown by the orange circles.
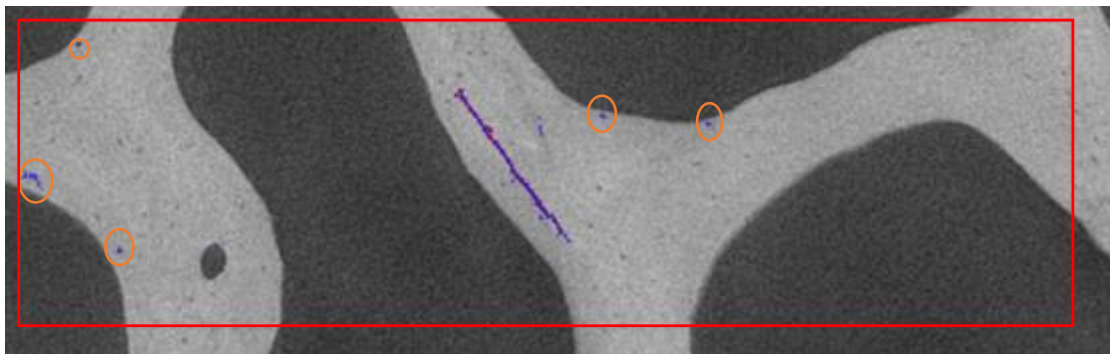
*Figure 4-5: Example of YOLOv4p5 results, where a red bounding box detects an exaggeratedly big region as a crack. However, Unet is capable of limiting the **mistake** by having little false positive, circled in orange, inside the bounding box. Blue is Unet segmentation , red pixels are the manual reference and purple is the overlapping region between both colours*

Another example of limitation is shown in Figure 4-6. In this case, the structure detected by YOLOv4 is not a crack but a natural structure of trabecular bone where the bone is connecting/splitting. Since the structure is not different enough from the linear micro-cracks, Unet will also segment it completely.
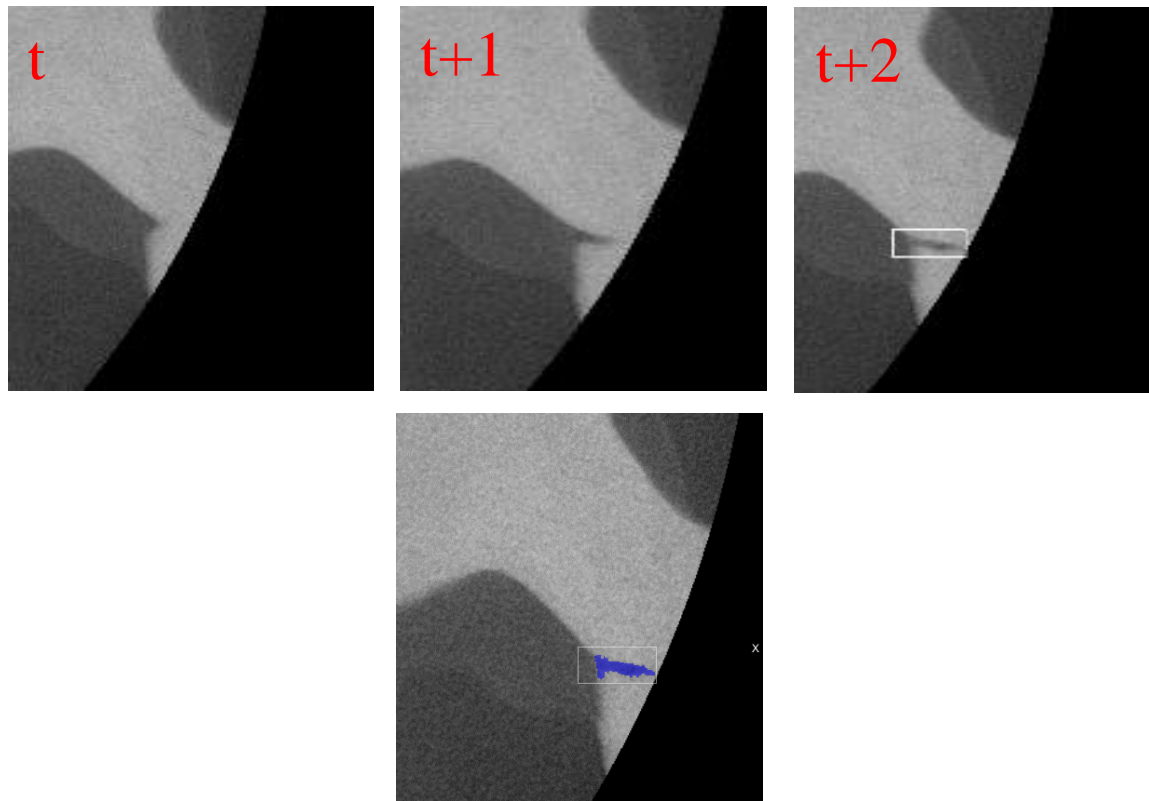
Figure 4-6 : Example of situation where crack-like feature is segmented by the two-step method. Top three images show the development of such a structure in the xz plane over multiple slices in the y axis. Where t is the first slice , t+1 the second slice and t+2 the third slice and the one containing Yolo false positive. Bottom image shows the false positive segmentation done by YOLO and Unet.

4.4.5 Comparison with contrast agent

This study compared the gold standard of microdamage identification, using the contrast agent, to the proposed deep learning approach. Figure 4-7 shows the differences in segmentation between contrast agent and deep learning methods. Generally, the contrast agent only marked the surface of the visible micro-cracks at the current resolution (2 microns), showed by red arrows. It also amplified some regions of the bone where there is no visible crack, showed by red circles. These regions could be showing possible damage at a size smaller than the image resolution. Figure 4-7 also shows that deep learning focuses on segmenting the linear micro-cracks visible at the image resolution, while the contrast agent amplifies some regions, but not necessarily fills in the region inside the cracks. This explains why no quantitative comparison was made between both techniques, since they visually mark different regions of the images. This is why the current gold standard could not be used as a validation method.
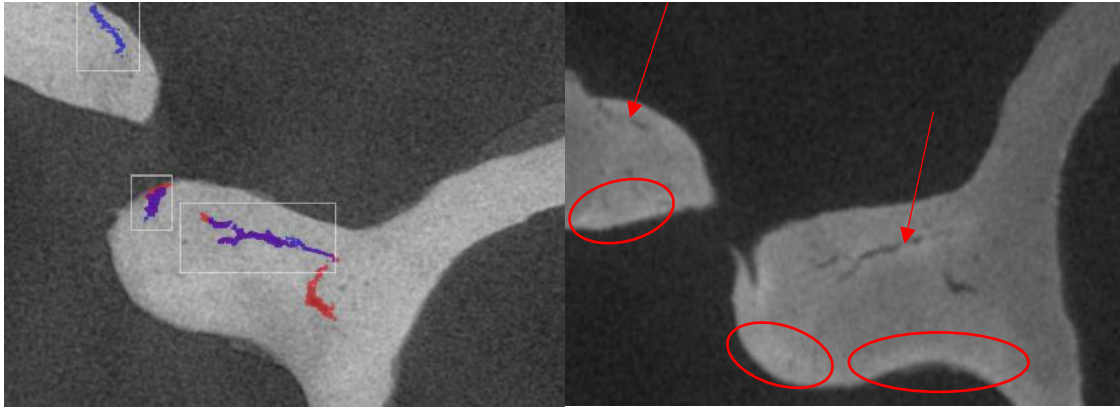
Figure 4-7: On the left there is a successful segmentation of microdamage done by Unet in blue, red is the reference segmentation and purple is the overlapping pixels and on the right there a microCT image with region enhanced with barium sulfate, seen as brighter white regions. We can see that Unet segments the area inside the microcracks, while the contrast agent seams to segment region around it (red arrow) and other regions of the trabeculae with no visible damage (red circles).

4.5 Discussion

The goal of this study was to use a two-step deep learning method using YOLOv4 and Unet to evaluate the feasibility to segment bone microdamage. Data was collected from six mechanically deformed bone cylinders using a microCT scanner at high resolution. Stacks of images were then randomly selected and segmented to train and test the deep learning models.

Deep learning has the potential to provide more accurate evaluation of bone microdamage than the contrast agent, considered as the gold standard. Indeed, Figure 4-7 shows that, with deep learning, the actual region inside the micro-cracks was segmented, whereas the barium sulfate highlights the region around the cracks and some other area that has no visible damage. This study supports the literature, which indicates that the contrast agent is mostly an approximation of the accumulated damage with increased loading and not an absolute segmentation of the damage volume (Leng et al., 2008). More investigation should be conducted to understand why the barium sulfate amplifies these regions specifically as opposed to filling the cracks. Concerning the crack being only segmented on the boundary, it might be because the contrast agent did not precipitate in larger region and only on the damage surface. As for the region without visible microcracks, it might be that smaller nonvisible damage was marked. A focus on these regions at higher resolution could indicated the nature of the segmentation.

Both YOLO and Unet neural networks performed relatively well during testing, even from a limited training data set. In this study, the number of training images was limited. This is partly due to the time-consuming and labor intensive manual annotation of cracks in the images. Furthermore, the collection for the first time of such a dataset of bone microdamage is expensive in terms of imaging facility. Nevertheless, the potential of the model was shown mostly in Sample 2 (Figure 4-3), with most of the pixels identified as purple, meaning that both the reference and Unet segmentations overlapped. In addition, results (Figure 4-5) showed that Unet allowed differentiating between background, pores and cracks, while all these structures are technically on the lower end of the intensity spectrum of the Xray images. Hence, even if Unet was not as performant at differentiating features as object detection NN (J. Liu et al., 2020), it was still able to segment with a good accuracy. While this study suggests that NN can learn from such a small dataset, future work could focus on improving the performance by increasing the size of training image data set.

The segmentation accuracy achieved by Unet is in the range of inter-user variability. When comparing the performance of the Unet segmentation combined to the manual bounding boxes (Table 2) with the performance of user 2 segmentation (Table 3), both IoU and Dice scores resulted in similar values. This result appears extremely positive for the Unet segmentation considering that the boundaries of bone micro-cracks are not always very sharp. At best, a neural network replicates the behavior it was trained to replicate. In this first study, we considered the annotations of only one user; any biases in the annotations, including systematic errors, can be transferred to the outcomes of the trained model ("Towards trustable machine learning", 2018). For this reason, more trustworthy annotations using at least three domain experts should be generated and considered for the training in future work.

The performance of the segmentation is related to the image quality. The performance of both models for sample 1 is considerably lower than for sample 2. Even for manual annotators, less agreement in the segmentation is observed for Sample 1. This can be explained first by a lower CNR for Sample 1 (Table 4). Second, the images used to train the model were almost homogeneous in terms of CNR, which could explain that the model generalizes more easily to unseen images of similar quality like in Sample 2, rather than to images of much worse CNR like in Sample 1. For

future work, it would be important to build a more diverse training set with a variety of CNR to avoid overfitting.

The crack detection achieved with YOLO allows a faster segmentation although there is an accumulation of errors. Indeed, results (Table 2) showed a decrease in both IoU and Dice scores when Unet was applied with the bounding boxes from YOLOv4p5, especially for sample 1. However, this difference was far from unexpected; as there are errors associated with both NNs tested individually, accumulated errors were anticipated when combining NNs. Conversely, there are advantages in combining NNs. Indeed, Unet is faster when combined with segmentation in BB only, instead of segmenting every single pixel in the whole image (J. Liu et al., 2020). Moreover, even if Yolov4p5 was shown to be more accurate than the YOLOv4 base model, it is not the deepest NN in the scaled-YOLOv4 family. The Darknet platform provides deeper YOLO models, such as the Yolov4-p6 model, which could possibly further increase the detection performance, but would also require more computational resources not available in this study. There is also the possibility of using a NN like mask-RCNN, that combines both object detection and semantic segmentation (He et al., 2017).

This study is associated with some limitations. First, it was limited by the image resolution, where it is impossible to detect microdamage smaller than the image resolution. Using higher resolution and longer scans to reduce noise or using synchrotron radiation micro-computed tomography could be investigated to achieve higher resolution at good image quality (Salomé et al., 1999; Seo & Kim, 2020). Secondly, this model was mainly trained for linear microcracks. Diffuse damage could not be segmented at the resolution used. In future work, evaluation of diffuse damage could provide a more complete analysis of bone microdamage, improve the comparison with contrast agents and make deep learning more compelling. Lastly, this model is limited by its application on 2D images, although microcracks are complex 3D structures (Ma et al., 2016). If the model was applied on a volume instead, it could use 3D information of microcracks to differentiate it from other bone features.

4.6   Conclusion

To our knowledge, this is the first study implementing a two-step deep learning model for the segmentation of bone microdamage. Even with a limited dataset, both YOLO and Unet models

could detect microdamage and differentiate it from other bone features with similar grey level. Even though accuracy was limited for Sample 1, the potential of this approach could be observed in Sample 2. Unet and Yolo not being specifically designed for bone microcracks detection, they could be further specialised for bone microdamage detection and segmentation. Moreover, working with 3D datasets could provide additional information to the neural network to learn microdamage features.

4.7 Acknowledgement

We thank Marie-Hélène Bernier for her help with the microCT and Christian-Charles Martel for his technical support. We also thank Nourine Omar for her help with the sensitivity study. This project was supported by the NSERC with the funding from the DISCOVERY and CREATE (OPSIDIAN) programs.

4.8 Declaration of competing interest

The authors declare that they have no known competing financial interests or personal relationships that could have appeared to influence the work reported in this paper.

4.9 References

Alsamadony, K. L., Yildirim, E. U., Glatz, G., Bin Waheed, U., & Hanafy, S. M. (2021). Deep Learning Driven Noise Reduction for Reduced Flux Computed Tomography. *Sensors, 21*(5),1921.doi: https://doi.org/10.48550/arXiv.2101.07376

Belda, R., Palomar, M., Peris-Serra, J. L., Vercher-Martínez, A., & Giner, E. (2020). Compression failure characterization of cancellous bone combining experimental testing, digital image correlation and finite element modeling. *International Journal of Mechanical Sciences, 165*, 105213. doi:https://doi.org/10.1016/j.ijmecsci.2019.105213 .

Bezerra, E. T. V., Augusto, K. S., & Paciornik, S. (2020). Discrimination of pores and cracks in iron ore pellets using deep learning neural networks. *REM-International Engineering Journal, 73*, 197-203.

Bochkovskiy, A., Wang, C.-Y., & Liao, H.-Y. M. (2020). Yolov4: Optimal speed and accuracy of object detection. *arXiv preprint arXiv:2004.10934*.

Burr, D. B., & Stafford, T. (1990). Validity of the bulk-staining technique to separate artifactual from in vivo bone microdamage. *Clinical Orthopaedics and Related Research*(260), 305-308.

Canada. (2021). Release notice - Osteoporosis and related fractures in Canada: Report from the Canadian Chronic Disease Surveillance System 2020. [Avis de publication - Rapport du Système canadien de surveillance des maladies chroniques : L'ostéoporose et les fractures

connexes au Canada, 2020]. *Health promotion and chronic disease prevention in Canada : research, policy and practice, 41*(2), 68-68. doi:10.24095/hpcdp.41.2.06

Chen, K., Reichard, G., Xu, X., & Akanmu, A. (2021). Automated crack segmentation in close-range building façade inspection images using deep learning techniques. *Journal of Building Engineering, 43*, 102913. doi:https://doi.org/10.1016/j.jobe.2021.102913

Coulombe, J. C., Mullen, Z. A., Weins, A. M., Fisher, L. E., Lynch, M. E., Stodieck, L. S., & Ferguson, V. L. (2022). Reduced local mechanical stimuli in spaceflight diminishes osteocyte lacunar morphometry and spatial heterogeneity in mouse cortical bone. *bioRxiv*, 2022.2001.2004.474962. doi:10.1101/2022.01.04.474962

Donahue, S. W., & Galley, S. A. (2006). Microdamage in bone: implications for fracture, repair, remodeling, and adaptation. *Crit Rev Biomed Eng, 34*(3), 215-271. doi:10.1615/critrevbiomedeng.v34.i3.20

Feng, X., Xiao, L., Li, W., Pei, L., Sun, Z., Ma, Z., Ju, H. (2020). Pavement Crack Detection and Segmentation Method Based on Improved Deep Learning Fusion Model. *Mathematical Problems in Engineering, 2020*, 8515213. doi:10.1155/2020/8515213

Frost, H. L. (1960). Presence of microscopic cracks in vivo in bone. *Henry Ford Hospital Medical Journal, 8*(1), 25-35. Available at:https://scholarlycommons.henryford.com/hfhmedjournal/vol8/iss1/4 .

Gagnon, C., & Lafrance, M. (2011). *Prévention des chutes auprès des personnes âgées vivant à domicile. Analyse des données scientifiques et recommandations préliminaires à l'élaboration d'un guide de pratique clinique*. Institut national de santé publique du Québec. Available at: http://www.inspq.qc.ca.

Green, J. O., Wang, J., Diab, T., Vidakovic, B., & Guldberg, R. E. (2011). Age-related differences in the morphology of microdamage propagation in trabecular bone. *J Biomech, 44*(15), 2659-2666. doi:10.1016/j.jbiomech.2011.08.006

He, K., Gkioxari, G., Dollár, P., & Girshick, R. (2017). *Mask r-cnn.* Paper presented at the Proceedings of the IEEE international conference on computer vision. *IEEE International Conference on Computer Vision (ICCV).* pp. 2980-2988, doi: 10.1109/ICCV.2017.322.

Herman, B. C., Cardoso, L., Majeska, R. J., Jepsen, K. J., & Schaffler, M. B. (2010). Activation of bone remodeling after fatigue: Differential response to linear microcracks and diffuse damage. *Bone, 47*(4), 766-772. doi:https://doi.org/10.1016/j.bone.2010.07.006

Heyndrickx, M., Bultreys, T., Goethals, W., Van Hoorebeke, L., & Boone, M. N. (2020). Improving image quality in fast, time-resolved micro-CT by weighted back projection. *Scientific Reports, 10*(1), 18029. doi:10.1038/s41598-020-74827-x

Huang, H., Zhao, S., Zhang, D., & Chen, J. (2022). Deep learning-based instance segmentation of cracks from shield tunnel lining images. *Structure and Infrastructure Engineering, 18*(2), 183-196. doi:10.1080/15732479.2020.1838559

Jiang, L., Xie, Y., & Ren, T. (2020). A deep neural networks approach for pixel-level runway pavement crack segmentation using drone-captured images. *arXiv preprint. doi:* https://doi.org/10.48550/arXiv.2001.03257

Kalfarisi, R., Wu, Z. Y., & Soh, K. (2020). Crack Detection and Segmentation Using Deep Learning with 3D Reality Mesh Model for Quantitative Assessment and Integrated Visualization.

Journal of Computing in Civil Engineering, 34(3), 04020010. doi:10.1061/(ASCE)CP.1943-5487.0000890

Kogawa, M., Khalid, K. A., Wijenayaka, A. R., Ormsby, R. T., Evdokiou, A., Anderson, P. H., . . . Atkins, G. J. (2018). Recombinant sclerostin antagonizes effects of ex vivo mechanical loading in trabecular bone and increases osteocyte lacunar size. *American journal of physiology. Cell physiology, 314*(1), C53-C61. doi:10.1152/ajpcell.00175.2017

Landrigan, M. D., Li, J., Turnbull, T. L., Burr, D. B., Niebur, G. L., & Roeder, R. K. (2011). Contrast-enhanced micro-computed tomography of fatigue microdamage accumulation in human cortical bone. *Bone, 48*(3), 443-450. doi:https://doi.org/10.1016/j.bone.2010.10.160

Lems, W. F., & Raterman, H. G. (2017). Critical issues and current challenges in osteoporosis and fracture prevention. An overview of unmet needs. *Ther Adv Musculoskelet Dis, 9*(12), 299-316. doi:10.1177/1759720x17732562

Leng, H., Wang, X., Niebur, G. L., & Roeder, R. K. (2006). Synthesis of a Barium Sulfate Nanoparticle Contrast Agent for Micro-Computed Tomography of Bone Microstructure. In *Ceramic Nanomaterials and Nanotechnology III* , 217-229.doi: 10.1002/9781118407158.ch24.

Leng, H., Wang, X., Ross, R. D., Niebur, G. L., & Roeder, R. K. (2008). Micro-computed tomography of fatigue microdamage in cortical bone using a barium sulfate contrast agent. *Journal of the mechanical behavior of biomedical materials, 1*(1), 68-75. doi: 10.1016/j.jmbbm.2007.06.002.

Lin, T.-Y., Maire, M., Belongie, S., Hays, J., Perona, P., Ramanan, D., Zitnick, C. L. (2014). *Microsoft coco: Common objects in context.* Paper presented at the European conference on computer vision.Spinger, Computer Vision-ECCV 2014, 740-755. doi: https://doi.org/10.1007/978-3-319-10602-1_48

Lindsey, R., Daluiski, A., Chopra, S., Lachapelle, A., Mozer, M., Sicular, S., . . . Potter, H. (2018). Deep neural network improves fracture detection by clinicians. *Proceedings of the National Academy of Sciences, 115*(45), 11591-11596. doi:10.1073/pnas.1806905115

Liu, F., & Wang, L. (2022). UNet-based model for crack detection integrating visual explanations. *Construction and Building Materials, 322*, 126265. doi:https://doi.org/10.1016/j.conbuildmat.2021.126265

Liu, J., Yang, X., Lau, S., Wang, X., Luo, S., Lee, V. C.-S., & Ding, L. (2020). Automated pavement crack detection and segmentation based on two-step convolutional neural network. *Computer-Aided Civil and Infrastructure Engineering, 35*(11), 1291-1305. doi:https://doi.org/10.1111/mice.12622

Liu, Y., Yao, J., Lu, X., Xie, R., & Li, L. (2019). DeepCrack: A deep hierarchical feature learning architecture for crack segmentation. *Neurocomputing, 338*, 139-153. doi:https://doi.org/10.1016/j.neucom.2019.01.036

Ma, S., Boughton, O., Karunaratne, A., Jin, A., Cobb, J., Hansen, U., & Abel, R. (2016). Synchrotron imaging assessment of bone quality. *Clinical Reviews in Bone and Mineral Metabolism, 14*(3), 150-160. doi: 10.1007/s12018-016-9223-3.

Munawar, H. S., Ullah, F., Heravi, A., Thaheem, M. J., & Maqsoom, A. (2022). Inspecting Buildings Using Drones and Computer Vision: A Machine Learning Approach to Detect Cracks and Damages. *Drones, 6*(1), 5. Retrieved from https://www.mdpi.com/2504-446X/6/1/5

Nagaraja, S., Couse, T. L., & Guldberg, R. E. (2005). Trabecular bone microdamage and microstructural stresses under uniaxial compression. *Journal of Biomechanics, 38*(4), 707-716. doi:https://doi.org/10.1016/j.jbiomech.2004.05.013

Presbítero, G., Gutiérrez, D., & Taylor, D. (2017). *Osteoporosis and Fatigue Fracture Prevention by Analysis of Bone Microdamage.* Paper presented at the TMS 2017 146th Annual Meeting & Exhibition Supplemental Proceedings, 319-330.doi: 10.1007/978-3-319-51493-2_30

Presbitero, G., Vopálenský, M., Kumpová, I., & Pithartova, K. (2019). Analysis of bone microdamage with X-ray microtomography towards fatigue fracture prevention. 9th Conference on Industrial Computed Tomography. available at : https://www.ndt.net/search/docs.php3?id=23704

Ronneberger, O., Fischer, P., & Brox, T. (2015). *U-net: Convolutional networks for biomedical image segmentation. Paper presented at the International Conference on Medical image computing and computer-assisted intervention. Medical Image Computing and Computer-Assisted Intervention – MICCAI 2015.*vol 9315. 234-241. doi: https://doi.org/10.48550/arXiv.1505.04597.

Salomé, M., Peyrin, F., Cloetens, P., Odet, C., Laval-Jeantet, A. M., Baruchel, J., & Spanne, P. (1999). A synchrotron radiation microtomography system for the analysis of trabecular bone samples. *Medical Physics, 26*(10), 2194-2204. doi: 10.1118/1.598736.

Seo, S.-J., & Kim, Y.-G. (2020). In-situ analysis of the hydration ability of bone graft material using a synchrotron radiation X-ray micro-CT. *Journal of Applied Biomaterials & Functional Materials, 18*. doi:10.1177/2280800020963476

Seref-Ferlengez, Z., Kennedy, O. D., & Schaffler, M. B. (2015). Bone microdamage, remodeling and bone fragility: how much damage is too much damage? *BoneKEy reports, 4*, 644-644. doi:10.1038/bonekey.2015.11

Shen, S. C.-y., Peña Fernández, M., Tozzi, G., & Buehler, M. J. (2021). Deep learning approach to assess damage mechanics of bone tissue. *Journal of the mechanical behavior of biomedical materials, 123*, 104761. doi:https://doi.org/10.1016/j.jmbbm.2021.104761

Shi, Y., Cui, L., Qi, Z., Meng, F., & Chen, Z. (2016). Automatic road crack detection using random structured forests. *IEEE Transactions on Intelligent Transportation Systems, 17*(12), 3434-3445. doi: 10.1109/TITS.2016.2552248

Shorten, C., & Khoshgoftaar, T. M. (2019). A survey on Image Data Augmentation for Deep Learning. *Journal of Big Data, 6*(1), 60. doi:10.1186/s40537-019-0197-0

Sözen, T., Özışık, L., & Başaran, N. Ç. (2017). An overview and management of osteoporosis. *European journal of rheumatology, 4*(1), 46-56. doi:10.5152/eurjrheum.2016.048

Tang, S. Y., & Vashishth, D. (2007). A non-invasive in vitro technique for the three-dimensional quantification of microdamage in trabecular bone. *Bone, 40*(5), 1259-1264. doi: "https://doi.org/10.1016/j.bone.2006.10.031"

Toppets, V., Pastoret, V., De Behr, V., Antoine, N., Dessy, C., & Gabriel, A. (2004). Morphologie, croissance et remaniement du tissu osseux. *Ann Med Vet, 148*, 1-13.

Towards trustable machine learning. (2018). *Nature biomedical engineering, 2*(10), 709-710. doi:10.1038/s41551-018-0315-x

Tu, K. N., Lie, J. D., Wan, C. K. V., Cameron, M., Austel, A. G., Nguyen, J. K., Hyun, D. (2018). Osteoporosis: A Review of Treatment Options. *P & T : a peer-reviewed journal for formulary management, 43*(2), 92-104. Retrieved from https://pubmed.ncbi.nlm.nih.gov/29386866

Turnbull, T. L., Gargac, J. A., Niebur, G. L., & Roeder, R. K. (2011). Detection of fatigue microdamage in whole rat femora using contrast-enhanced micro-computed tomography. *Journal of Biomechanics, 44*(13), 2395-2400. doi:https://doi.org/10.1016/j.jbiomech.2011.06.032

Wang, L., MA, X. h., & Ye, Y. (2020, 22-24 Aug. 2020). *Computer vision-based Road Crack Detection Using an Improved I-UNet Convolutional Networks.* Paper presented at the 2020 Chinese Control And Decision Conference (CCDC), 539-543. doi: 10.1109/CCDC49329.2020.9164476.

Wang, X., Masse, D. B., Leng, H., Hess, K. P., Ross, R. D., Roeder, R. K., & Niebur, G. L. (2007). Detection of trabecular bone microdamage by micro-computed tomography. *Journal of Biomechanics, 40*(15), 3397-3403. doi:https://doi.org/10.1016/j.jbiomech.2007.05.009

Wright, N. C., Looker, A. C., Saag, K. G., Curtis, J. R., Delzell, E. S., Randall, S., & Dawson-Hughes, B. (2014). The recent prevalence of osteoporosis and low bone mass in the United States based on bone mineral density at the femoral neck or lumbar spine. *J Bone Miner Res, 29*(11), 2520-2526. doi:10.1002/jbmr.2269

Zhang, A., Wang, K. C. P., Fei, Y., Liu, Y., Tao, S., Chen, C., Li, B. (2018). Deep Learning–Based Fully Automated Pavement Crack Detection on 3D Asphalt Surfaces with an Improved CrackNet. *Journal of Computing in Civil Engineering, 32*(5), 04018041. doi:10.1061/(ASCE)CP.1943-5487.0000775

Zhang, L., Shen, J., & Zhu, B. (2021). A research on an improved Unet-based concrete crack detection algorithm. *Structural Health Monitoring, 20*(4), 1864-1879. doi:10.1177/1475921720940068

Zhang, L., Yang, F., Zhang, Y. D., & Zhu, Y. J. (2016, 25-28 Sept. 2016). *Road crack detection using deep convolutional neural network.* Paper presented at the 2016 IEEE International Conference on Image Processing (ICIP), 3708-3712. doi: 10.1109/ICIP.2016.7533052.

Zhang, T., Li, S., Chen, Y., Xiao, H., Wang, L., Hu, J., Lu, H. Characterize the microstructure change after tendon enthesis injury using synchrotron radiation μCT. *Journal of Orthopaedic Research, n/a*(n/a). doi:https://doi.org/10.1002/jor.25289

Zhang, X., Liu, X., Yan, Z., Cai, J., Kang, F., Shan, S., Jing, D. (2018). Spatiotemporal characterization of microdamage accumulation in rat ulnae in response to uniaxial compressive fatigue loading. *Bone, 108*, 156-164. doi:https://doi.org/10.1016/j.bone.2018.01.011

Zhang, X., Rajan, D., & Story, B. (2019). Concrete crack detection using context-aware deep semantic segmentation network. *Computer-Aided Civil and Infrastructure Engineering, 34*(11), 951-971. doi:https://doi.org/10.1111/mice.12477

CHAPTER 5   COMPLEMENTARY ANALYSIS USING DIGITAL VOLUME CORRELATION.

5.1   General introduction

Digital image correlation (DIC) provides information on the internal strain and displacement patterns developing in a sample, which cannot be obtained from strain gauges and extensometers. DIC was developed in the early 1980s allowing for the measurement of strains from 2D images by correlating small subsets of images, before and after loading, using a variety of correlation functions [169, 170]. Digital volume correlation (DVC) was further developed to adapt the DIC technique to entire volume using cubic subsets instead of square subsets [102]. Since then, several studies have used DVC to investigate bone fracture mechanisms at the microscopic level using microCT images [10, 174-176]. For example, Marta Peña Fernández studied strain distributions in relation to newly formed bone in osteoinductive biomaterials [174]. G. Tozzi even correlated the region of high strains during mechanical loading of a full vertebra to its damaged area [178].

Performing DVC from combined mechanical testing and imaging can provide additional information about the development of bone microdamage *ex vivo*. This second study consists in an explanatory work for the continuation of this research. The goal of this study was to explore the relationship between regions of high displacement and regions of microdamage in bone trabecular samples. To do so, one bone sample was deformed under two compression steps and imaged before mechanical testing and after each loading step to investigate the application of DVC.

5.2   Material and method

Sample preparation

One trabecular bone cylinder of 8.3 mm in diameter was extracted from a bovine tail vertebra using a diamond core drill (Diamon Production, Canada) mounted on a drill press. The core drill was kept under constant irrigation with distilled water to reduce the heat created by the cut [179]. Afterward, the sample was cut at a height of 7mm using an isoMet 1000 (Buehler, Illinois) at a speed of 250 rpm.

Mechanical testing

Quasi-static compression loading along the height of the sample (or z-axis) and with multiple steps was carried out on the cylinder. First, the sample was thawed out overnight at a temperature of 4 °C the day before mechanical testing. The sample was installed inside the Deben *in situ* micro-tensile testing system (Deben, UK) after having its length and diameter measured. A preload of 20N was applied to ensure the stability of the setup. The sample was further loaded at a rate of 0,5 mm/min until 6% deformation and then until 10% or until the ultimate stress (where the slope of the plastic region approaches zero), but before the complete failure of the sample.

Imaging

The sample was imaged inside the Deben system, before the first displacement and after each displacement at a resolution of 2.09 μm, voltage of 110kV and 10W with 2001 rotations and an exposition time of 16 seconds.

Deep learning test

YOLOv4p5 NN (Chapter 4) was applied to this dataset to test its capacity to localize bone microcracks on images from a dataset scanned inside the Deben *in situ* testing stage.

DVC

After the deep learning test, the sample was down sampled by a factor of 4, because the dataset was too big for the hardware used for this study. Then using IDVC, a Matlab DVC algorithm made by FranckLab [180], the internal 3D strain map was computed using the local approach. The algorithm computes the 3D displacement map in the x directions, y directions, z directions and for the magnitude displacement vectors. This algorithm also claims to be designed for large deformations and provides deformations in voxels on a normalized scale [180].

5.3   Results

The second loading increment was stopped at 9% since the ultimate stress was reached (slope of the strain-stress curve approaching 0).

After imaging, the dataset had a volume of 2022 (y), 1978 (x) and 1984 (z) voxels. After down sampling, the resulting dataset had a resolution of 8.35 μm with a volume of 505 (y), X 494 (x) and 496 (z) voxels.

5.3.1 Deep learning

The YOLOv4p5 NN was unable to correctly locate the damage in the images obtained inside the Deben *in-situ* loading system, which was used for both mechanical test and imaging. Indeed, images had a CNR considerably lower (1,8) than the samples imaged in the previous study (Chapter 4), which CNR ranged from 7,96 to 10,08. This is probably due to the sample diameter being much smaller than the Deben system loading tube. Therefore, the Xray source had to be far from the sample compared to the previous study (Chapter 4) where the sample was imaged outside the Deben system and the source could be placed closer.

5.3.2 DVC

After the first loading step, reaching 6% strain, higher displacements in the z-direction and in 3D magnitude were observed in the lower region of the volume (along the z axis) (Figure 5-1C,D). Maximum displacements in the z-direction are larger (around 30 voxels) than in the x and y-directions (around 5 and 10 voxels respectively), which is expected since the sample was loaded along the z-axis.
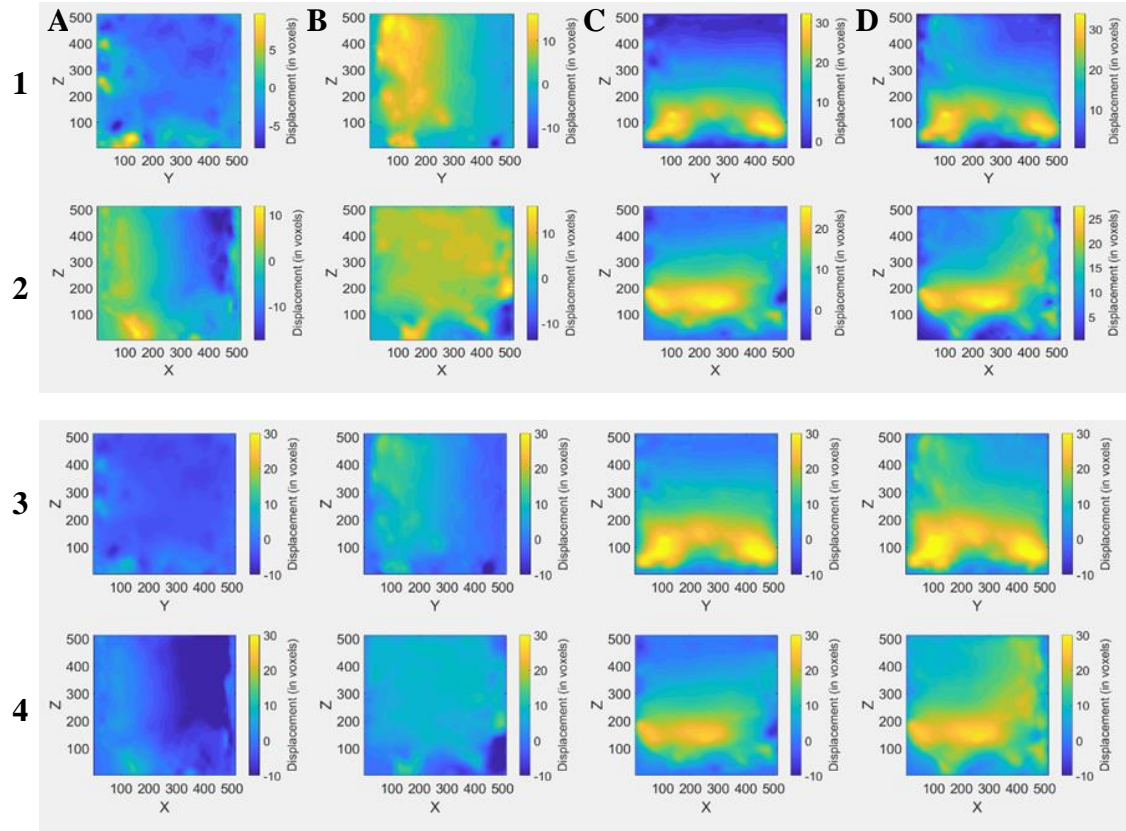
Figure 5-1: Each image represents a 2D sample of the 3D displacement field taken from the center of the sample after the first compression step (0-6% strain). 1)&2) The color map was adjusted for each image individually to better visualize the displacement gradient. 3)&4) The color map was adjusted to be on the same scale to compare displacement size. The displacements in the ZY plane are represented in 1)&3) and the displacements in the ZX plane are represented in the 2)&4). Columns with A) displacements in the x-direction B) displacements in the y-direction C) displacements in the z-direction and D) magnitude of the 3D displacements.

After the first deformation (0-6% strain), there was barely any damage present in the sample. Therefore, it was difficult to establish any relationship between microdamage and high displacements. However, the regions showing high displacement magnitude (in the lower region along the z axis) started to show some microdamage (Figure 5-2), while the regions located higher along the z axis showed no damage at all.
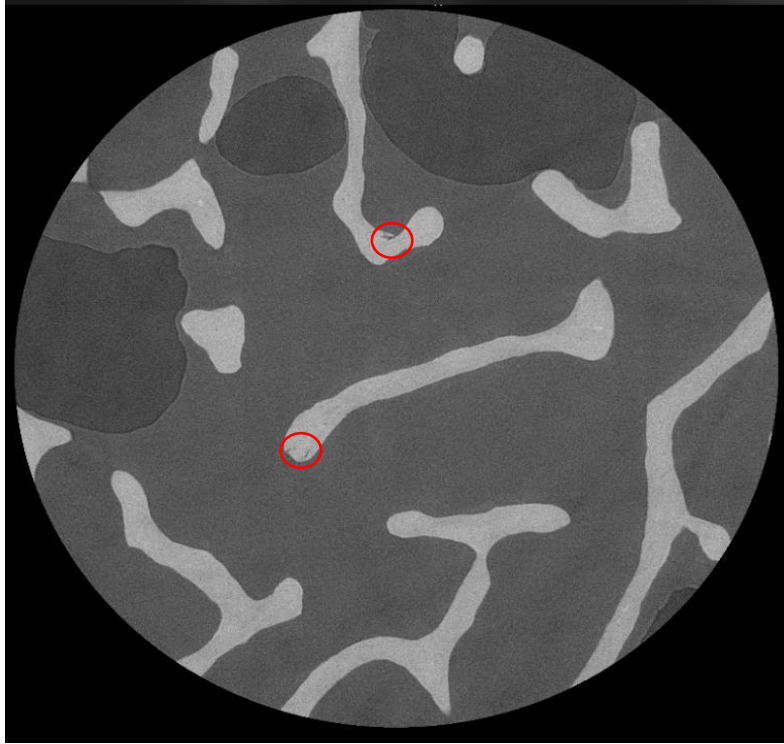
Figure 5-2: Slice 62 (XY plane)is shown after the first deformation (6% strain). A small amount of damage is show with red circles.

This behavior is even more apparent in Figure 5-3, which shows resulting displacement maps for the second loading step (6-9% strain). Displacement in x, y and z directions are at their maximum in the lower region along the z axis (Figure 5-3(A,B,C)), which is resulting in a maximum magnitude in the lower regions of the volume (Figure 5-3(D)).
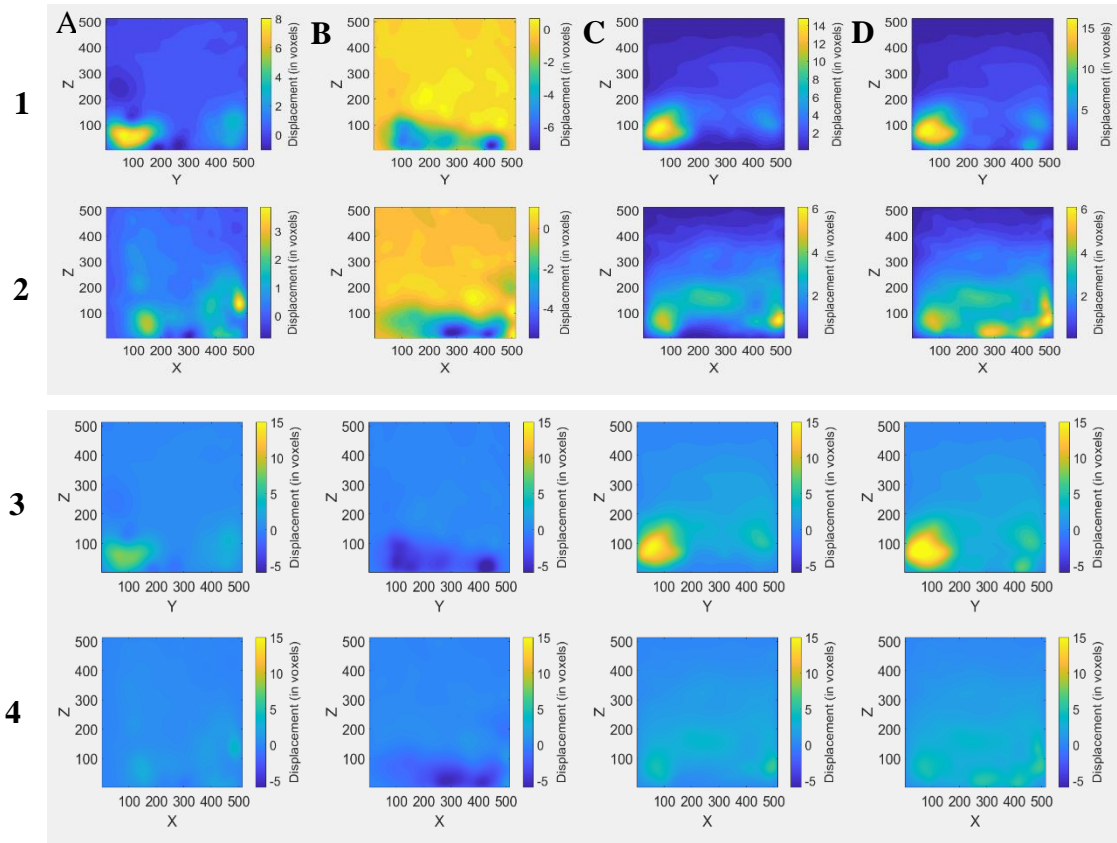
Figure 5-3 : Each image represents a 2D sample of the 3D displacement field taken from the center of the sample after the second compression step (6-9% strain). 1)&2) The color map was adjusted for each image individually to better visualize the displacement gradient. 3)&4) The color map was adjusted to be on the same scale to compare displacement size. The displacements in the ZY plane are represented in 1)&3) and the displacements in the ZX plane are represented in the 2)&4). Columns with A) the displacements in the x-direction B) displacements in the y-direction C) displacements in the z-direction and D) magnitude of the 3D displacements.

These regions of high strain are also the regions that have accumulated more microdamage. Figure 5-4(E) and Figure 5-5(E) confirm that statement. They are respectively showing slices 40 and 80 (of the XY plane), which both contain several zones with microdamage. Conversely, regions around slice 200 (XY plane), which is located further along the z-axis, only show negligible damage (Figure 5-6(E)), while regions around slice 300 show (XY plane) no damage at all (Figure 5-7(E)). Visualization in the XY plane also confirms that maximum displacement in the z direction are relatively more important in the lower slices (around 15 voxels) (Figure 5-4(C) and Figure 5-5(C)) than in the higher slices (around 2 to 5 voxels) (Figure 5-6(C) and Figure 5-7(C)).

Looking at Figure 5-4 A, B, C and D, there is a maximum displacement in the bottom left corner, which is an error associated to the DVC computation. This region is outside the bone cylinder and only composed of voids, and therefore cannot represent a real maximum displacement. Other

regions of high displacement can however be localized, and they are circled in red and black, with red circles being regions that also overlap with microdamage. In Figure 5-4(C, D), there are several regions of high displacement that also overlap with regions of microdamage. However, the region of high displacement circled in black does not seem to correspond to any microdamage. This indicates that the displacement-microdamage relationship might not be consistent in the XY plane.
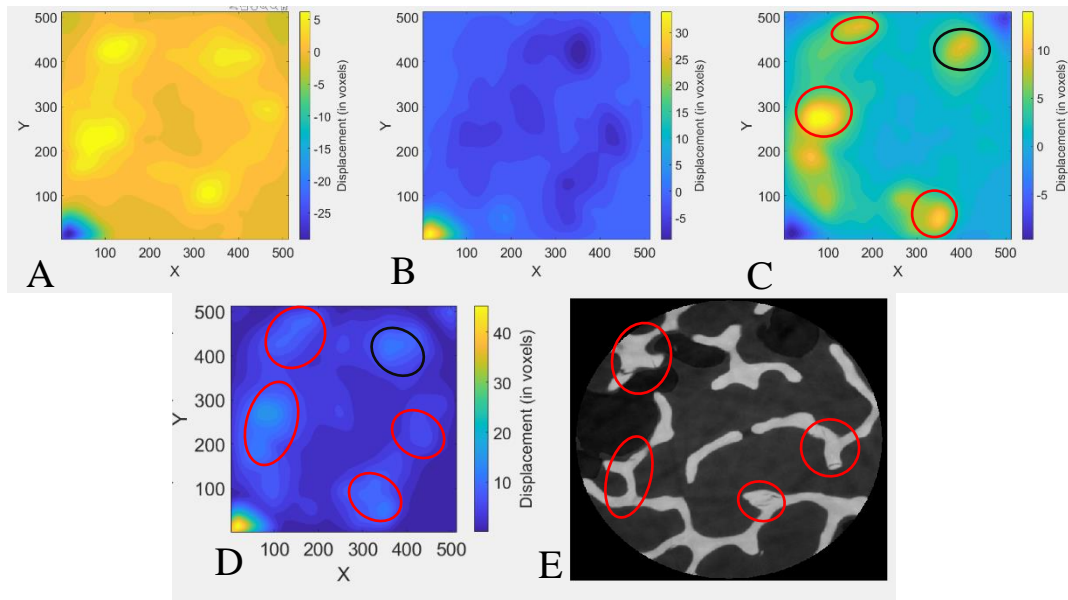
Figure 5-4: Representation of the displacement in the XY plane for slice 40 (along z-axis). The color map was adjusted for each image individually to better visualize the displacement gradient. A) displacements in the x-direction. B) displacements in the y-direction. C) displacements in the z-direction, the compression direction D) the magnitude of 3D displacements. Regions of high displacement are circled in red and black. E) Observed microdamage is delimited with red circles.

Additionally, looking at slice 80 (Figure 5-5(C, D, E)), those correlations are hardly present since only one small displacement region overlap with microdamage and the other regions of high displacement, circled in black, does not correspond to microdamage. Therefore, these relationships are not extremely strong, and it is hard to conclude that regions of high damage and high displacement in the XY plane can be correlated using this approach.
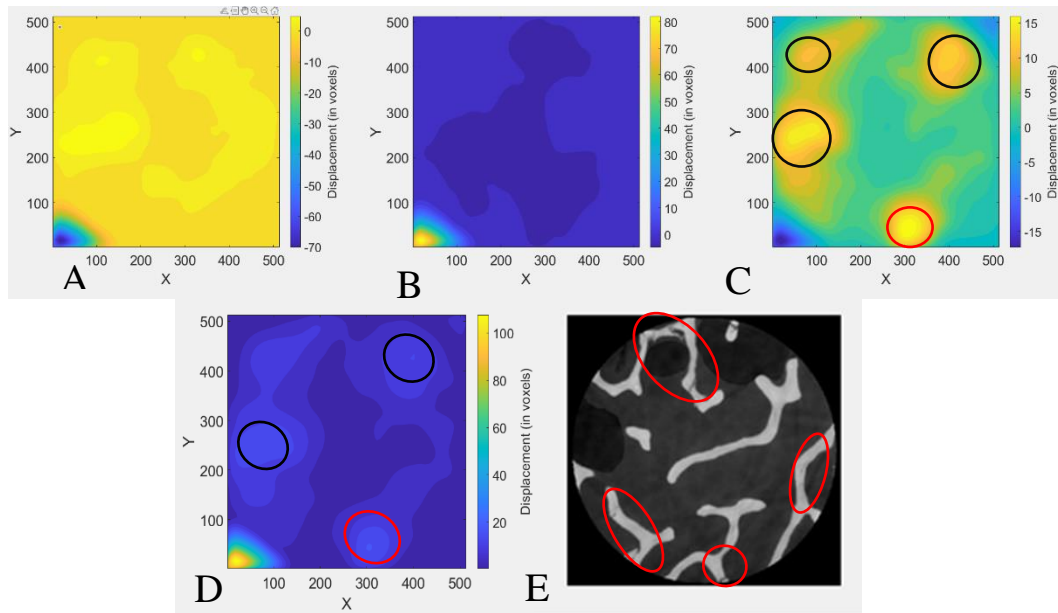
Figure 5-5: Representation of the displacement in the XY plane for slice 80 (along z-axis). The color map was adjusted for each image individually to better visualize the displacement gradient. A) displacements in the x-direction. B) displacements in the y-direction. C) displacements in the z-direction D) magnitude of all displacements. Regions of high displacement are circled in red and black. E) Observed microdamage is delimited with red circles.
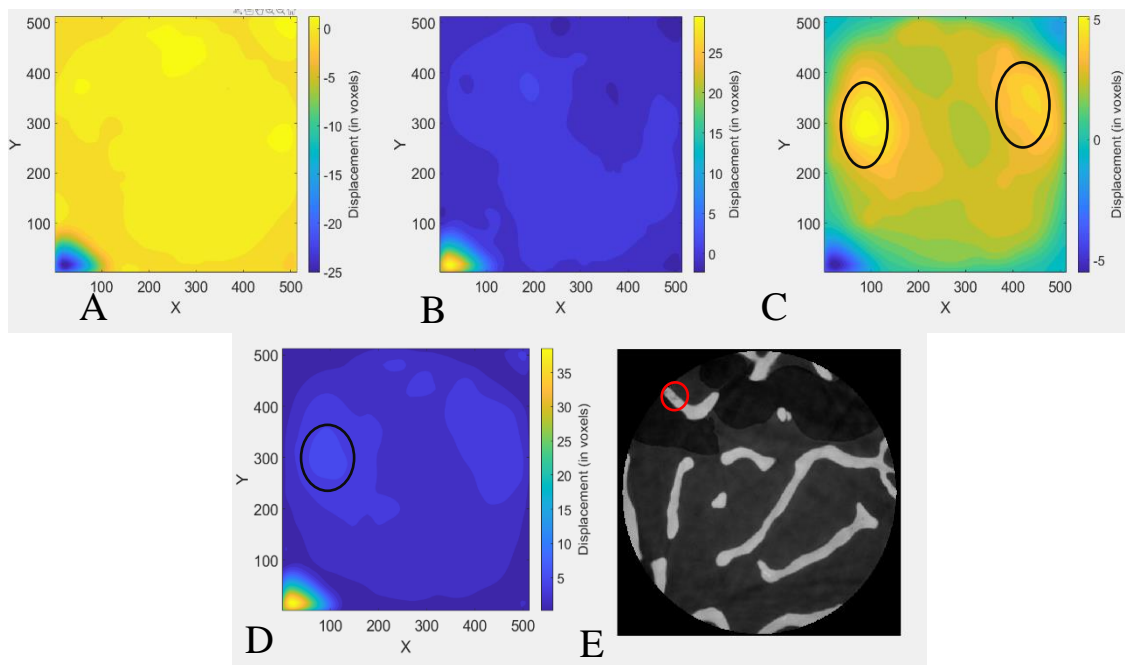
Figure 5-6 : Representation of the displacement in the XY plane for slice 200 (along z-axis). The color map was adjusted for each image individually to better visualize the displacement gradient. A) displacements in the x-direction. B) displacements in the y-direction. C) displacements in the z-direction, the compression direction D) the magnitude of 3D displacements. Regions of high displacement are circled in red and black. E) Observed microdamage is delimited with red circles.
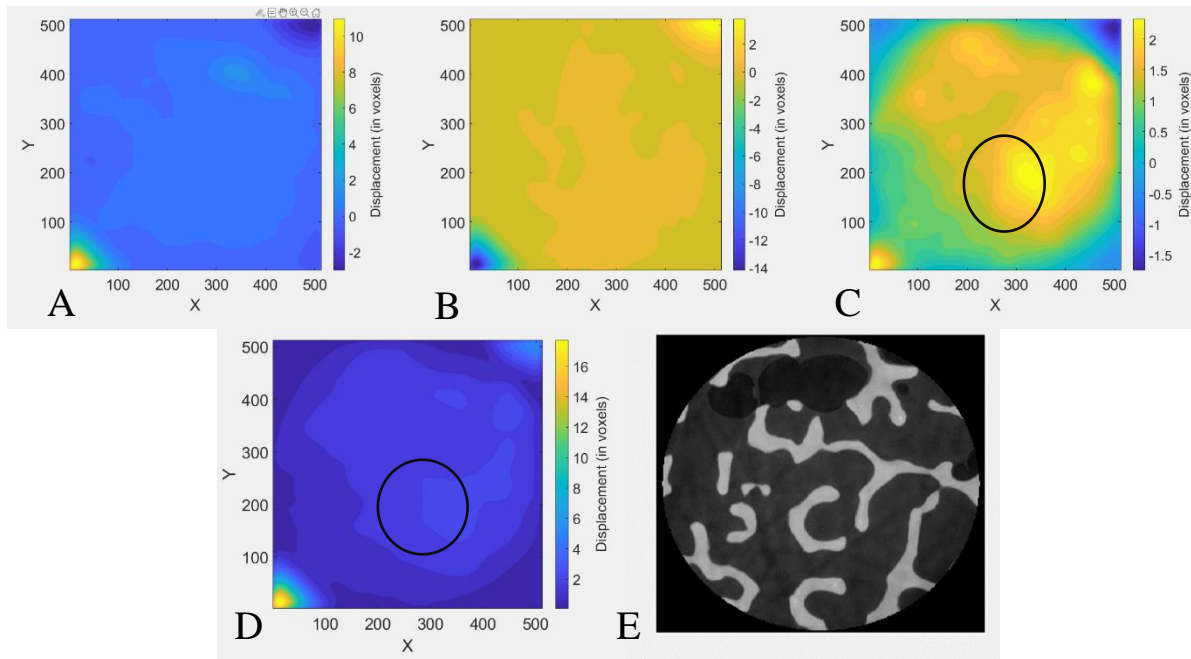
Figure 5-7 : Representation of the displacement in the XY plane for slice 300 (along z-axis). The color map was adjusted for each image individually to better visualize the displacement gradient. A) displacement in the x-direction. B) displacement in the y-direction. C) displacement in the z-direction, the compression direction D) the magnitude of 3D displacement. Regions of high displacement are circled black. E) No observed microdamage at slice 300.

5.4   Conclusion

In this complimentary study, an open-source Matlab code for a DVC algorithm (IDVC) was applied to image volumes of a trabecular bone sample after it was mechanically loaded under two strain increments with microCT imaging between each loading step. Displacement maps were then illustrated and examined to establish colocalization with damaged area.

This work comes with a major limitation, which is the number of sample. Since only one sample was studied in this work, no scientific conclusion can be drawn from this and the result should only be used to help developing the protocol for the next study. Another limitation is the use of a simple open source Matlab algorithm. Even if FranckLab has proven the efficiency of the algorithm [180], open source code like this one often has limitation in their application, since the lab often focus on their own work. Therefore, having a commercial license for a DVC software could greatly help develop a procedure in the future.

In conclusion, this complementary study explores the application of DVC to correlate regions of high strain to region of microdamage and test the application of YOLOv4p5 for microcracks

detection. This study showed some relationship between location of high strain along the z axis and location of microcracks. However, the strain was hardly correlated to damage in the xy plane. Moreover, this study showed the importance of having a diverse dataset for deep learning training, since the NN (presented in Chapter 4) was not able to detect any microcracks. In future work, a more robust algorithm using a mesh reconstruction of the bone tissue could be used to improve the result. It would make computation between subsection more precise, and it would exclude the marrow space from the final volume, hence making visualization easier. Moreover, having smaller strain increment between each scan could improve the precision of the displacement calculation.

CHAPTER 6   GENERAL DISCUSSION

This project allowed investigating trabecular bone biomechanics in a non-destructive way using *in vitro* mechanical testing and microCT imaging, combined with deep learning neural network for the automatic segmentation of microdamage in trabecular bone. The following points were drawn from the studies:

- Image quality, including resolution and noise level, is important for the adequate detection of micro damage, namely bone microcracks.
- Datasets with CNR lower than one used to train the deep learning models may show poor results compared to datasets with similar CNR.
- Deep learning models can be used to classify and segment linear microcracks. However, the resulting accuracy was lower compared to more common application (pavement cracks) since it used a small dataset with little variability between images and it was also the first time using deep learning for this specific application.
- General region of high strain can be colocalized with region of damage along the z axis.

Complementary discussion points are presented below.

6.1   Deep learning

The performance of YOLOV4 coupled with Unet could not be compared to the literature. To our knowledge, there is no other study performing deep learning segmentation of microdamage in trabecular bone samples. However, when comparing to NN applied to a different (but similar) application, the performance obtained in this study was worse. Indeed, Liu et al.[151] did the comparison between different models which were all applied to the CrackForest Dataset, which is an opensource dataset of annotated road cracks. The listed studies achieved an F1 score (Dice score) ranging from 45,70 for a model in 2010 [181] to 95,75 for their model proposed in 2020. Our segmentation resulted in a Dice score of 41,34 and 73,58 for Samples 1 and 2 of the test group, respectively. This is fairly lower compared to the current crack segmentation models in other applications. However, these models have a pre-annotated dataset to train and test on. They also have been modified and improved for generations for their specific application. If such a data base was implemented using microCT images of different noise, resolution, and size, for bone

microdamage, it could greatly improve the models performance [182]. Moreover, bone images can be more challenging since other structures, such as lacunae, have the same grey intensity as the cracks, like the marrow space and lacunae. This is where using 3D input could help, since cracks are planar structures and this information can be used to help the NN make decision [121].

Image resolution was a limiting factor in segmenting the ground truth. It was sometimes hard to evaluate if a small structure was noise, an artefact or if it was a really small linear microcracks. This made the segmentation tedious and could have influenced the results. The inter-user study showed that the data set with lower CNR was harder to segment more consistently than the one with higher CNR. However, only two users were compared using only two datasets. A study with more data and more users could be beneficial to provide a more complete analysis. In addition, small clusters of cracks were sometimes hard to segment since they were close to each other's.

YOLOv4p5 was not trained with proper geometric data augmentation. The data augmentation included in YOLO (Hue and intensity) was tested in a preliminary study using DragonFly YOLOv3 implementation and had poorer performance than geometric deformations for the detection of bone micro damage. In this study, the only geometric data augmentation tested was done before training the NN, using a python algorithm instead of having it integrated to the YOLO algorithm. This method showed poorer performance than without adding geometric data augmentation. Therefore, future work should include an algorithm that also includes geometric data augmentation inside its neural network instead of using an open-source python library.

When using deep learning, it is not necessary to remove the bone marrow from the sample. Every bone sample (Chapter 4) had their marrow removed to keep the experimental conditions constant for mechanical loading and imaging. It was more precisely required to remove bone marrow before bulk staining for the optimal penetration of contrast agent in the two test samples and further comparison with the deep learning segmentation. However, it should be noted that microdamage localization and segmentation with deep learning can be effectively done without removing bone marrow. Avoiding marrow removal reduces the risk of inducing damage during the cleaning process and keeps the sample closer to its *in vivo* conditions.

YOLOv4p5 was not able to annotate microcracks with the image quality when the sample is scanned inside the Deben (Chapter 5). After applying the NN to the high-resolution images scanned inside the Deben after the second deformation (6-9%), a qualitative observation showed

that no damage was annotated. This behavior reinforces that images with lower quality (lower CNR), and of quality different than the training set, will be difficult for the NN to treat. Therefore, having a range of different image qualities for training should be beneficial for the detection of bone microdamage.

6.2   Hardware

While training the deep learning NN, models were not always chosen for their performance but because of the 8GB of Video RAM available. Training a deep learning model is highly dependent on the amount of video RAM available. For example, YOLOv4P5 is not the biggest scaled YOLOv4 neural network available. YOLOv4P6 and YOLOv4p7 (with pyTorch) have better mAP than YOLOv4p5 but require more VRAM. Therefore, future work could use a GPU with more VRAM and a bigger scale YOLOv4 model to improve the performance.

6.3   Digital Volume Correlation

Regions of high displacement in the first deformation became relatively more important in the second deformation. Results show that if there was a region of maximum displacement in the lower region along the z-axis in the first deformation (Figure 5-3 (C,D) especially) it would generally stay the region of maximum displacement in the second deformation (Figure 5-6 (C,D)). Also, the region of low displacement became even smaller relative to the maximum displacement, often close to zero. It looks like the region of high displacement became a compression zone where the mechanical strength is lower and deforms more than the rest of the structure. This behavior agrees with a past study in the literature in which strain region became more concentrated to a specific location [178].

Strain increments used in this work were bigger than the increments used in the literature. DVC analysis normally uses small increments to be able to precisely measure the 3D strain map, lower than 2%   [174, 176, 183]. In this study, large deformations were used to ensure the development of microdamage, which started to be visible at 6-8 % strain in most samples. Preliminary test showed that trabecular bone sample extracted from bovine tails generally needed to be deformed between 10-14% to have enough microdamage accumulated for image analysis purposes at two microns. Therefore, large increments were adopted to limit the amount of scan,

since doing high resolution scan is time consuming and expensive. However, as shown in Chapter 5, high resolution scans are not required for DVC and are actually a disadvantage since they require a lot of RAM and processing power. Therefore, for future study, it would be recommended to have more strain increments but of smaller magnitude (1-2%). This way, there could be a series of low and high resolution scans, with scans for DVC purposes done with a lower resolution (around 8 microns) at every loading step. Additionally, at every increment of 5-6% strain, a high-resolution scan (0,5-2 microns) could be done to evaluate the microdamage using deep learning segmentation. This way it would be easier to track strain during the deformation and would still have multiple time during the deformation to study the progression of microdamage at high resolution.

High displacement regions and regions with more damage are both located in the lower regions along the z-axis. DVC results (Figure 5-3) showed that regions of high displacements in x,y,z after the second deformation was colocalized with area of microcracks in the lower z slices. Even after the first deformation, the little amount of damage accumulated in the sample was located in the lower half of the sample. This behavior agrees with a past experimental studies in which the trabecular bone crushed zone was aligned with the high strain region [178]. In contrast, no strong correlation was made with the current algorithm when looking at region of displacement and damage in the xy plane. This could be explained by: strain increments between each deformation are too large for precise calculation or, the algorithm is not robust enough to provide good visualization of the displacement map (DVC subset too big). Indeed, IDVC was developed for fast iterations and large deformations. However, the literature more often uses small deformations and the computation is rather long [180]. Moreover, having a graphic representation with only the area composed of bone tissue (removing the pixel composing the empty space) could greatly improve the visualization of the result, since it would be easier to see if the regions of high strain are in bone (and close to the damage).

CHAPTER 7   CONCLUSION AND RECOMMANDATIONS.

This research project led to the development of three components of a 3D *ex vivo* platform for the evaluation of bone micro damage, including two experimental studies. The first study showed the potential of deep learning to segment trabecular bone microdamage to eventually replace the approach based on contrast agents. Mechanical tests were performed to induce microdamage in trabecular bone samples. These samples were further imaged at high resolution and used to train and test YOLOv4 and Unet in a two-step segmentation process. The second study showed that strain maps obtained from a DVC software can allow colocalizing regions of high displacements with regions of high microdamage along the compression direction.

The first study on deep learning segmentation allowed answering the first research question («What is the potential of deep learning algorithms in the evaluation of bone microdamage in trabecular bone samples? ») by showing that bone microdamage can be evaluated using deep learning segmentation. This study also showed that a good accuracy can be obtained when the training and testing images have a similar quality, as measured by the CNR. Conversely, a low accuracy can result when the training and testing images have different quality. This is why having a dataset with a range of different image qualities could be useful for the NN to learn different conditions during training. The NNs were also used for the first time for this application of bone microdamage segmentation. With incremental change in the NN layers, the performance should greatly increase in future work.

The second study partially answered the second research question («What additional information can be drawn by including digital volume correlation in the study of bone microdamage quantification vs mechanical properties?») by showing that region of high displacements can also be regions with more microcracks. Additional work is however required to draw a more solid conclusion. In this study, a MATLAB algorithm called IDVC allowed measuring the 3D strain maps, which showed that regions of high displacements in the lower regions along the z axis were also regions of high microdamage. However, no consistent relationship between damage and strain could be drawn in the xy plane. As only one sample was tested, this research work should be pursued with more samples to infer on the relationship between bone microdamage and high displacement regions.

Listed below are recommendations for the continuation of this project, in order to improve the accuracy of the current model or bring additional information to the analysis:

- include the evaluation of bone density in the analyzes;
- compare Unet and YOLO to other NN models (RCNN, CrackNet, Mask-RCNN, etc.) to verify which one is the most performant;
- create a dataset of bone microcracks with a range of image qualities and with multiple user annotations;
- use a 3D image dataset to take advantage of the planar structure of microcracks;
- use a commercial DVC software that could be more precise than an open source DVC algorithm;
- use smaller increments in the compression steps for further DVC computation;
- investigate the relationships between bone mechanical properties and microdamage volume.

To our knowledge, this is the first study implementing a two-step deep learning model for the segmentation of bone microdamage. It is also the first *ex vivo* experiment to be design with the goal of analyzing the 3D components of bone and including mechanical properties, bone microdamage quantification and 3D strain maps all in one procedure. Future work should focus on using 3D datasets to quantify the damage volume in order to create correlation with mechanical properties. Moreover, including diffuse damage for the deep learning segmentation could be important since this type of damage might play a role in bone biomechanics and in osteoporosis fractures. Extending the *ex vivo* platform to cortical bone testing would then give information about both types of bone leading to an improved understanding of their respective roles in bone biomechanics and fracture mechanisms. Hopefully, the additional knowledge would lead to development of new diagnostic or treatment approaches.

REFERENCES

[1]   Sözen, T., Özışık, L., and Başaran, N.Ç.: 'An overview and management of osteoporosis', Eur J Rheumatol, 2017, 4, (1), pp. 46-56

[2]   Wright, N.C., Looker, A.C., Saag, K.G., Curtis, J.R., Delzell, E.S., Randall, S., and Dawson-Hughes, B.: 'The recent prevalence of osteoporosis and low bone mass in the United States based on bone mineral density at the femoral neck or lumbar spine', J Bone Miner Res, 2014, 29, (11), pp. 2520-2526

[3]   Canada, G.o.: '2009 Canadian Community Health Survey', in Editor (Ed.)^(Eds.): 'Book 2009 Canadian Community Health Survey' (2009, edn.), pp.

[4]   Tu, K.N., Lie, J.D., Wan, C.K.V., Cameron, M., Austel, A.G., Nguyen, J.K., Van, K., and Hyun, D.: 'Osteoporosis: A Review of Treatment Options', P & T : a peer-reviewed journal for formulary management, 2018, 43, (2), pp. 92-104

[5]   Lems, W.F., and Raterman, H.G.: 'Critical issues and current challenges in osteoporosis and fracture prevention. An overview of unmet needs', Ther Adv Musculoskelet Dis, 2017, 9, (12), pp. 299-316

[6]   Thurner, P.J., Wyss, P., Voide, R., Stauber, M., Stampanoni, M., Sennhauser, U., and Müller, R.: 'Time-lapsed investigation of three-dimensional failure and damage accumulation in trabecular bone using synchrotron light', Bone, 2006, 39, (2), pp. 289-299

[7]   Larrue, A., Rattner, A., Peter, Z.A., Olivier, C., Laroche, N., Vico, L., and Peyrin, F.: 'Synchrotron radiation micro-CT at the micrometer scale for the analysis of the three-dimensional morphology of microcracks in human trabecular bone', PLoS One, 2011, 6, (7), pp. e21297

[8]   Wolfram,U., Schwiedrzik, J.J., Mirzaali, M.J., Bürki, A., Varga, P., Olivier, C., Peyrin, F., and Zysset, P.K.: 'Characterizing microcrack orientation distribution functions in osteonal bone samples', Journal of Microscopy, 2016, 264, (3), pp. 268-281

[9]   Keller, T.S., Mao, Z., and Spengler, D.M.: 'Young's modulus, bending strength, and tissue physical properties of human compact bone', Journal of Orthopaedic Research, 1990, 8, (4), pp. 592-603

[10]   Roberts, B.C., Perilli, E., and Reynolds, K.J.: 'Application of the digital volume correlation technique for the measurement of displacement and strain fields in bone: A literature review', Journal of Biomechanics, 2014, 47, (5), pp. 923-934

[11]   Cowan, P.T., and Kahai, P.: 'Anatomy, Bones': 'StatPearls' (StatPearls Publishing Copyright © 2020, StatPearls Publishing LLC., 2020)

[12]   Clarke, B.: 'Normal bone anatomy and physiology', Clin J Am Soc Nephrol, 2008, 3 Suppl 3, (Suppl 3), pp. S131-139

[13]   Hartwig, W.C.: 'The anatomy and biology of the human skeleton by D. Gentry Steele and Claud A. Bramblett. Texas A & M University Press, College Station, 1988', Clinical Anatomy, 1990, 3, (2), pp. 151-153

[14]   Allen, M.R., and Burr, D.B.: 'Chapter 4 - Bone Modeling and Remodeling', in Burr, D.B., and Allen, M.R. (Eds.): 'Basic and Applied Bone Biology' (Academic Press, 2014), pp. 75-90

[15]   J. Gordon Betts, P.D., Eddie Johnson,Jody E. Johnson,Oksana Korol,Dean Kruse,Brandon Poe,James A. Wise ,Mark Womble,Kelly A. Young: '6.2 Bone Classification': 'Anatomy & Physiology' (OpenStax CNX, 2013)

[16]   J. Gordon Betts, P.D., Eddie Johnson,Jody E. Johnson,Oksana Korol,Dean Kruse,Brandon Poe,James A. Wise ,Mark Womble,Kelly A. Young: '6.3 Bone structure': 'Anatomy & Physiology' (OpenStax CNX, 2013)

[17]   Thomas, T., Martin, A., and Lafage-Proust, M.: 'Physiologie du tissu osseux', EMC - Appareil locomoteur, 2008, 3, pp. 1-16

[18]   Blausen.com staff (2014). "Medical gallery of Blausen Medical 2014". WikiJournal of Medicine 1 (2). DOI:10.15347/wjm/2014.010. ISSN 2002-4436

[19]   Florencio-Silva, R., Sasso, G.R.d.S., Sasso-Cerri, E., Simões, M.J., and Cerri, P.S.: 'Biology of Bone Tissue: Structure, Function, and Factors That Influence Bone Cells', BioMed Research International, 2015, 2015, pp. 421746

[20]   Everts, V., Delaissé, J.M., Korper, W., Jansen, D.C., Tigchelaar-Gutter, W., Saftig, P., and Beertsen, W.: 'The Bone Lining Cell: Its Role in Cleaning Howship's Lacunae and Initiating Bone Formation', Journal of Bone and Mineral Research, 2002, 17, (1), pp. 77-90

[21]   Miller, S.C., de Saint-Georges, L., Bowman, B.M., and Jee, W.S.: 'Bone lining cells: structure and function', Scanning microscopy, 1989, 3, (3), pp. 27

[22]   Ralston, S.H.: 'Bone structure and metabolism', Medicine, 2013, 41, (10), pp. 581-585

[23]   Gartner, L.P., and Hiatt, J.L.: '7 - Cartilage and Bone', in Gartner, L.P., and Hiatt, J.L. (Eds.): 'Concise Histology' (W.B. Saunders, 2011), pp. 74-93

[24]   SEER Training Modules, Anatomy & Physiology: Skeletal System:Structure of Bone Tissue. U. S. National Institutes of Health, National Cancer Institute. June 6 2020 <https://training.seer.cancer.gov/anatomy/skeletal/tissue.html>.

[25]   Lucchinetti, E., Thomann, D., and Danuser, G.: 'Review Micromechanical testing of bone trabeculae - potentials and limitations', Journal of Materials Science, 2000, 35, (24), pp. 6057-6065

[26]   Monier-Faugere, M.-C., Chris Langub, M., and Malluche, H.H.: 'Chapter 8 - Bone Biopsies: A Modern Approach', in Avioli, L.V., and Krane, S.M. (Eds.): 'Metabolic Bone Disease and Clinically Related Disorders (Third Edition)' (Academic Press, 1998), pp. 237-280e

[27]   Compston, J.: 'CHAPTER 23 - Histomorphometric Manifestations of Age-Related Bone Loss', in Rosen, C.J., Glowacki, J., and Bilezikian, J.P. (Eds.): 'The Aging Skeleton' (Academic Press, 1999), pp. 251-261

[28]   Health, U.D.o., and Services, H.: 'Bone health and osteoporosis: a report of the Surgeon General', Rockville, MD: US Department of Health and Human Services, Office of the Surgeon General, 2004, 87

[29]   Vidal, B., Pinto, A., Galvão, M., Santos, A., Rodrigues, A., Cascão, R., Abdulghani, S., Caetano-Lopes, J., Ferreira, A., and Fonseca, J.: 'Bone histomorphometry revisited', Acta reumatologica portuguesa, 2012, 37, (4)

[30]   Dalle Carbonare, L., Valenti, M., Bertoldo, F., Zanatta, M., Zenari, S., Realdi, G., Cascio, V.L., and Giannini, S.: 'Bone microarchitecture evaluated by histomorphometry', Micron, 2005, 36, (7-8), pp. 609-616

[31]   Kanis, J.A., Malluche, H., Meunier, P.J., and Ott, S.M.: 'Bone histomorphometry: standardization of nomenclature, symbols, and units', Journal of bone and mineral research, 1987, 2, (6)

[32]   Klintström, E., Smedby, O., Klintström, B., Brismar, T., and Moreno, R.: 'Trabecular bone histomorphometric measurements and contrast-to-noise ratio in CBCT', Dento maxillo facial radiology, 2014, 43, pp. 20140196

[33]   da Silva, A.M.H., Alves, J.M., da Silva, O.L., and da Silva Junior, N.F.: 'Two and three-dimensional morphometric analysis of trabecular bone using X-ray microtomography (μCT)', Rev. Bras. Eng. Bioméd, 2014, 30, (2), pp. 93-101

[34]   Toppets, V., Pastoret, V., De Behr, V., Antoine, N., Dessy, C., and Gabriel, A.: 'Morphologie, croissance et remaniement du tissu osseux', Ann Med Vet, 2004, 148, pp. 1-13

[35]   Ott, S.M.: 'Cortical or trabecular bone: what's the difference?', American journal of nephrology, 2018, 47, (6), pp. 373-376

[36]   Iyo, T., Maki, Y., Sasaki, N., and Nakata, M.: 'Anisotropic viscoelastic properties of cortical bone', Journal of Biomechanics, 2004, 37, (9), pp. 1433-1437

[37]   Morgan, E.F., Unnikrisnan, G.U., and Hussein, A.I.: 'Bone Mechanical Properties in Healthy and Diseased States', Annu Rev Biomed Eng, 2018, 20, pp. 119-143

[38]   Iwaniec, U.T., and Turner, R.T.: 'Chapter 39 - Animal Models for Osteoporosis', in Marcus, R., Feldman, D., Dempster, D.W., Luckey, M., and Cauley, J.A. (Eds.): 'Osteoporosis (Fourth Edition)' (Academic Press, 2013), pp. 939-961

[39]   Gunson, D., Gropp, K.E., and Varela, A.: 'Chapter 63 - Bone and Joints', in Haschek, W.M., Rousseaux, C.G., and Wallig, M.A. (Eds.): 'Haschek and Rousseaux's Handbook of Toxicologic Pathology (Third Edition)' (Academic Press, 2013), pp. 2761-2858

[40]   Vahle, J.L., Ma, Y.L., and Burr, D.B.: 'Chapter 32 - Skeletal Assessments in the Nonhuman Primate', in Bluemel, J., Korte, S., Schenck, E., and Weinbauer, G.F. (Eds.): 'The Nonhuman Primate in Nonclinical Drug Development and Safety Assessment' (Academic Press, 2015), pp. 605-625

[41]   Courtney, T.H.: 'Mechanical behavior of materials' (Waveland Press, 2005. 2005)

[42]   Noushini, A., Aslani, F., Castel, A., Gilbert, R.I., Uy, B., and Foster, S.: 'Compressive stress-strain model for low-calcium fly ash-based geopolymer and heat-cured Portland cement concrete', Cement and Concrete Composites, 2016, 73, pp. 136-146

[43]   Bankoff, A.D.P.: 'Biomechanical characteristics of the bone', Human musculoskeletal biomechanics, 2012, 61, pp. 86

[44]   Kim, D.-G., Jeong, Y.-H., Kosel, E., Agnew, A.M., McComb, D.W., Bodnyk, K., Hart, R.T., Kim, M.K., Han, S.Y., and Johnston, W.M.: 'Regional variation of bone tissue properties at the human mandibular condyle', Bone, 2015, 77, pp. 98-106

[45]   Doitpoms.ac.uk. 2022. DoITPoMS. ' Mechanical properties of bone'. [Online] Available: https://www.doitpoms.ac.uk/tlplib/bones/bone_mechanical.php. Accessed: november 2021.

[46]   Sedlin, E.D.: 'A Rheologic Model for Cortical Bone: A Study of the Physical Properties of Human Femoral Samples', Acta Orthopaedica Scandinavica, 1965, 36, (sup83), pp. 1-77

[47]   Piekarski, K.: 'Analysis of bone as a composite material', International Journal of Engineering Science, 1973, 11, (6), pp. 557-565

[48]   Pawlak, A., Rozanski, A., and Galeski, A.: 'Thermovision studies of plastic deformation and cavitation in polypropylene', Mechanics of Materials, 2013, 67, pp. 104-118

[49]   Hay, E.D.: 'Cell biology of extracellular matrix',Springer Science & Business Media, 1991

[50]   Abramowitch, S., and Easley, D.: 'Chapter Four - Introduction to Classical Mechanics', in Hoyte, L., and Damaser, M. (Eds.): 'Biomechanics of the Female Pelvic Floor' (Academic Press, 2016), pp. 89-107

[51]   Roylance, D.: 'Stress-strain curves', Massachusetts Institute of Technology study, Cambridge, 2001

[52]   Li, S., Demirci, E., and Silberschmidt, V.V.: 'Variability and anisotropy of mechanical behavior of cortical bone in tension and compression', J Mech Behav Biomed Mater, 2013, 21, pp. 109-120

[53]   Reilly, D.T., and Burstein, A.H.: 'The elastic and ultimate properties of compact bone tissue', Journal of biomechanics, 1975, 8, (6), pp. 393-405

[54]   McElhaney, J.H.: 'Dynamic response of bone and muscle tissue', Journal of applied physiology, 1966, 21, (4), pp. 1231-1236

[55]   Linde, F., Nørgaard, P., Hvid, I., Odgaard, A., and Søballe, K.: 'Mechanical properties of trabecular bone. Dependency on strain rate', Journal of Biomechanics, 1991, 24, (9), pp. 803-809

[56]   Schoenfeld, C.M., Lautenschlager, E.P., and Meyer, P.R.: 'Mechanical properties of human cancellous bone in the femoral head', Medical and biological engineering, 1974, 12, (3), pp. 313-317

[57]   Ambrosio, L., de Santis, R., Iannace, S., Netti, P.A., and Nicolais, L.: 'Viscoelastic behavior of composite ligament prostheses', J. Biomed. Mater. Res, 1998, 42

[58]   Johnson, T.P.M., Socrate, S., and Boyce, M.C.: 'A viscoelastic, viscoplastic model of cortical bone valid at low and high strain rates', Acta Biomaterialia, 2010, 6, (10), pp. 4073-4080

[59]   Horan, M.P., and An, Y.H.: 'Bone, Mechanical Testing of': 'Wiley Encyclopedia of Biomedical Engineering'

[60]   Sharir, A., Barak, M.M., and Shahar, R.: 'Whole bone mechanics and mechanical testing', The Veterinary Journal, 2008, 177, (1), pp. 8-17

[61]   Deng, H., Liu, Y., and Guo, C.Y.: 'Current Topics in Bone Biology' (World Scientific, 2005. 2005)

[62]   An, Y.H., and Draughn, R.A.: 'Mechanical properties and testing methods of bone': 'Animal models in orthopaedic research' (CRC Press, 2020), pp. 139-163

[63]   Adharapurapu, R.R., Jiang, F., and Vecchio, K.S.: 'Dynamic fracture of bovine bone', Materials Science and Engineering: C, 2006, 26, (8), pp. 1325-1332

[64]   Jones, S., Faulkner, G., Raboud, D., Fyfe, K., and Wolfaardt, J.: 'Simulation of Impact Test for Determining "Health" of Percutaneous Bone Anchored Implants', Journal of Biomechanical Engineering, 2006, 128, (5), pp. 647-653

[65]   Wang, X., Masse, D.B., Leng, H., Hess, K.P., Ross, R.D., Roeder, R.K., and Niebur, G.L.: 'Detection of trabecular bone microdamage by micro-computed tomography', Journal of Biomechanics, 2007, 40, (15), pp. 3397-3403

[66]   Lambers, F.M., Bouman, A.R., Rimnac, C.M., and Hernandez, C.J.: 'Microdamage caused by fatigue loading in human cancellous bone: relationship to reductions in bone biomechanical performance', PLoS One, 2013, 8, (12), pp. e83662-e83662

[67]   Bertollo, N., and Walsh, W.R.: 'Drilling of bone: practicality, limitations and complications associated with surgical drill-bits', Biomechanics in applications, 2011, 4, pp. 53-83

[68]   Davies, C., Jones, D., Stoddart, M., Koller, K., Smith, E., Archer, C., and Richards, R.: 'Mechanically loaded ex vivo bone culture system 'Zetos': systems and culture preparation', Eur Cell Mater, 2006, 11, pp. 57-75

[69]   Standard, A.: 'C39/C39M, Standard test method for compressive strength of cylindrical concrete specimens', ASTM International, 2005

[70]   Yu, Y.: 'Contributions of anisotropic and heterogeneous tissue modulus to apparent trabecular bone mechanical properties', Columbia University, 2017

[71]   Hernandez, C.J., Ramsey, D.S., Dux, S.J., Chu, E.H., and Rimnac, C.M.: 'Irradiation Does Not Modify Mechanical Properties of Cancellous Bone Under Compression', Clinical Orthopaedics and Related Research®, 2012, 470, (9), pp. 2488-2495

[72]   Feng, L., and Jasiuk, I.: 'Effect of specimen geometry on tensile strength of cortical bone', Journal of Biomedical Materials Research Part A, 2010, 95A, (2), pp. 580-587

[73]   Zheng, P., Chen, R., Liu, H., Chen, J., Zhang, Z., Liu, X., and Shen, Y.: 'On the standards and practices for miniaturized tensile test – A review', Fusion Engineering and Design, 2020, 161, pp. 112006

[74]   Sanchez-Molina, D., Velazquez-Ameijide, J., Quintana, V., Arregui-Dalmases, C., Crandall, J.R., Subit, D., and Kerrigan, J.R.: 'Fractal dimension and mechanical properties of human cortical bone', Medical Engineering & Physics, 2013, 35, (5), pp. 576-582

[75]   Pettarin, V., Churruca, M., Felhos, D., Karger-Kocsis, J., and Frontini, P.: 'Changes in tribological performance of high molecular weight high density polyethylene induced by the addition of molybdenum disulphide particles', Wear, 2010, 269, pp. 31-45

[76]   Carriero, A., Bruse, J., Suchacki, K., Millán, J., Farquharson, C., and Shefelbine, S.: 'Reference point indentation is not indicative of whole bone stress intensity fracture toughness', Bone, 2014, 69, pp. 174–179

[77]   Willett, T., Josey, D., Lu, R.X.Z., Minhas, G., and Montesano, J.: 'The micro-damage process zone during transverse cortical bone fracture: No ears at crack growth initiation', J Mech Behav Biomed Mater, 2017, 74, pp. 371-382

[78]   Burr, D.B., Turner, C.H., Naick, P., Forwood, M.R., Ambrosius, W., Sayeed Hasan, M., and Pidaparti, R.: 'Does microdamage accumulation affect the mechanical properties of bone?', Journal of Biomechanics, 1998, 31, (4), pp. 337-345

[79]   Brancheriau, L., Bailleres, H., and Guitard, D.: 'Comparison between modulus of elasticity values calculated using 3 and 4 point bending tests on wooden samples', Wood Science and Technology, 2002, 36, (5), pp. 367-383

[80]   Babiak, M., Gaff, M., Sikora, A., and Hysek, Š.: 'Modulus of elasticity in three- and four-point bending of wood', Composite Structures, 2018, 204, pp. 454-465

[81]   Temenoff, J., and Mikos, A.: 'Chapter 4. Mechanical properties of biomaterials', Biomaterials: the intersection of biology and material science. Upper Saddle River (NJ): Pearson Prentice Hall Bioengineering, 2008, pp. 152

[82]   Gherardi Hein, P.R., and Brancheriau, L.: 'Comparison between three-point and four-point flexural tests to determine wood strength of Eucalyptus specimens', Maderas: Ciencia y Tecnología, 2018, 20

[83]   Oksztulska-Kolanek, E., Znorko, B., Michałowska, M., and Pawlak, K.: 'The Biomechanical Testing for the Assessment of Bone Quality in an Experimental Model of Chronic Kidney Disease', Nephron, 2016, 132, (1), pp. 51-58

[84]   Camp, M.: 'A biomechanical investigation of torsion and classic metaphyseal lesions', Boston University, 2020

[85]   Gaware, S.S., and Khan, S.N.: 'Torsion Value Assessment of Human Humerus Bone', International Journal of Engineering Sciences, 2020, pp. 146-151

[86]   Mirzaali, M.J., Libonati, F., Böhm, C., Rinaudo, L., Cesana, B.M., Ulivieri, F.M., and Vergani, L.: 'Fatigue-caused damage in trabecular bone from clinical, morphological and mechanical perspectives', International Journal of Fatigue, 2020, 133, pp. 105451

[87]   Wakayama, S., and Suemune, T.: 'Characterization of Fracture Process in Bovine Bones under Static and Cyclic Loading', Journal of Biomechanical Science and Engineering, 2008, 3, (4), pp. 490-498

[88]   Gagnon, C., and Lafrance, M.: 'Prévention des chutes auprès des personnes âgées vivant à domicile. Analyse des données scientifiques et recommandations préliminaires à l'élaboration d'un guide de pratique clinique', in Editor (Ed.)^(Eds.): 'Book Prévention des chutes auprès des personnes âgées vivant à domicile. Analyse des données scientifiques et recommandations préliminaires à l'élaboration d'un guide de pratique clinique' (Institut national de santé publique du Québec, 2011, edn.), pp.

[89]   Warriner, A.H., Patkar, N.M., Curtis, J.R., Delzell, E., Gary, L., Kilgore, M., and Saag, K.: 'Which fractures are most attributable to osteoporosis?', Journal of clinical epidemiology, 2011, 64, (1), pp. 46-53

[90]   Osterhoff, G., Morgan, E.F., Shefelbine, S.J., Karim, L., McNamara, L.M., and Augat, P.: 'Bone mechanical properties and changes with osteoporosis', Injury, 2016, 47 Suppl 2, (Suppl 2), pp. S11-S20

[91]   Chen, H., Zhou, X., Fujita, H., Onozuka, M., and Kubo, K.Y.: 'Age-related changes in trabecular and cortical bone microstructure', Int J Endocrinol, 2013, 2013, pp. 213234

[92]   Dorset, D.L.: 'X-ray Diffraction: A Practical Approach', Microsc Microanal, 1998, 4, (5), pp. 513-515

[93]   Mihailidis, D.: 'Computed Tomography From Photon Statistics to Modern Cone-Beam CT', Medical Physics, 2009, 36, (8), pp. 3858-3858

[94]   Prince, J.L., and Links, J.M.: 'Medical imaging signals and systems' (Pearson Prentice Hall Upper Saddle River, 2006)

[95]   Britannica, The Editors of Encyclopaedia. "delta ray". Encyclopedia Britannica, 2 Dec. 2014, https://www.britannica.com/science/delta-ray. accessed july 24 2020

[96]   Mudgal, P., Moore, C. 'Characteristic radiation'. Reference article, Radiopaedia.org. https://doi.org/10.53347/rID-25429, accessed july 2020

[97]   Andersen, J., and Laegsgaard, E.: 'Characteristic radiation from channeled electrons', Physical Review Letters, 1980, 44, (16), pp. 1079

[98]   L'Annunziata, M.F.: '1 - NUCLEAR RADIATION, ITS INTERACTION WITH MATTER AND RADIOISOTOPE DECAY', in L'Annunziata, M.F. (Ed.): 'Handbook of Radioactivity Analysis (Second Edition)' (Academic Press, 2003), pp. 1-121

[99]   Marghany, M.: 'Chapter 3 - Quantization of Maxwell's equations', in Marghany, M. (Ed.): 'Synthetic Aperture Radar Imaging Mechanism for Oil Spills' (Gulf Professional Publishing, 2020), pp. 41-60

[100]   Mijnarends, P.E., and Bansil, A.: 'Compton Scattering Techniques': 'Reference Module in Materials Science and Materials Engineering' (Elsevier, 2016)

[101]   Landis, E.N., and Keane, D.T.: 'X-ray microtomography', Materials Characterization, 2010, 61, (12), pp. 1305-1316

[102]   Jiroušek, O., Jandejsek, I., and Vavřík, D.: 'Evaluation of strain field in microstructures using micro-CT and digital volume correlation', Journal of Instrumentation, 2011, 6, (01), pp. C01039

[103]   Ashton, J.R., West, J.L., and Badea, C.T.: 'In vivo small animal micro-CT using nanoparticle contrast agents', Frontiers in Pharmacology, 2015, 6

[104]   Poundarik, A.A., and Vashishth, D.: 'Multiscale imaging of bone microdamage', Connective Tissue Research, 2015, 56, (2), pp. 87-98

[105]   Hernandez, C.J., Lambers, F.M., Widjaja, J., Chapa, C., and Rimnac, C.M.: 'Quantitative relationships between microdamage and cancellous bone strength and stiffness', Bone, 2014, 66, pp. 205-213

[106]   Karim, L., and Vashishth, D.: 'Role of trabecular microarchitecture in the formation, accumulation, and morphology of microdamage in human cancellous bone', J Orthop Res, 2011, 29, (11), pp. 1739-1744

[107]   Landrigan, M.D., Li, J., Turnbull, T.L., Burr, D.B., Niebur, G.L., and Roeder, R.K.: 'Contrast-enhanced micro-computed tomography of fatigue microdamage accumulation in human cortical bone', Bone, 2011, 48, (3), pp. 443-450

[108]   Herman, B.C., Cardoso, L., Majeska, R.J., Jepsen, K.J., and Schaffler, M.B.: 'Activation of bone remodeling after fatigue: Differential response to linear microcracks and diffuse damage', Bone, 2010, 47, (4), pp. 766-772

[109]   Zhang, X., Liu, X., Yan, Z., Cai, J., Kang, F., Shan, S., Wang, P., Zhai, M., Edward Guo, X., Luo, E., and Jing, D.: 'Spatiotemporal characterization of microdamage accumulation in rat ulnae in response to uniaxial compressive fatigue loading', Bone, 2018, 108, pp. 156-164

[110]   Seref-Ferlengez, Z., Kennedy, O.D., and Schaffler, M.B.: 'Bone microdamage, remodeling and bone fragility: how much damage is too much damage?', Bonekey Rep, 2015, 4, pp. 644-644

[111]   Seref-Ferlengez, Z., Basta-Pljakic, J., Kennedy, O.D., Philemon, C.J., and Schaffler, M.B.: 'Structural and mechanical repair of diffuse damage in cortical bone in vivo', Journal of bone and mineral research : the official journal of the American Society for Bone and Mineral Research, 2014, 29, (12), pp. 2537-2544

[112]   Diab, T., Condon, K.W., Burr, D.B., and Vashishth, D.: 'Age-related change in the damage morphology of human cortical bone and its role in bone fragility', Bone, 2006, 38, (3), pp. 427-431

[113]   Diab, T., and Vashishth, D.: 'Morphology, localization and accumulation of in vivo microdamage in human cortical bone', Bone, 2007, 40, (3), pp. 612-618

[114]   Diab, T., Sit, S., Kim, D., Rho, J., and Vashishth, D.: 'Age-dependent fatigue behaviour of human cortical bone', Eur J Morphol, 2005, 42, (1-2), pp. 53-59

[115]   Fila, T., Kytýř, D., Zlamal, P., Kumpova, I., Doktor, T., Koudelka, P., and Jiroušek, O.: 'High-resolution time-lapse tomography of rat vertebrae during compressive loading: Deformation response analysis', Journal of Instrumentation, 2014, 9, (05), pp. C05054

[116]   Hambli, R.: 'Multiscale prediction of crack density and crack length accumulation in trabecular bone based on neural networks and finite element simulation', International Journal for Numerical Methods in Biomedical Engineering, 2011, 27, (4), pp. 461-475

[117]   Donnelly, E.: 'Methods for Assessing Bone Quality: A Review', Clinical Orthopaedics and Related Research®, 2011, 469, (8), pp. 2128-2138

[118]   Presbitero, G., Vopálenský, M., Kumpová, I., and Pithartova, K.: 'Analysis of bone microdamage with X-ray microtomography towards fatigue fracture prevention', 2019

[119]   Leng, H., Wang, X., Niebur, G.L., and Roeder, R.K.: 'Synthesis of a Barium Sulfate Nanoparticle Contrast Agent for Micro-Computed Tomography of Bone Microstructure': 'Ceramic Nanomaterials and Nanotechnology III' (2006), pp. 217-229

[120]   Leng, H., Wang, X., Ross, R.D., Niebur, G.L., and Roeder, R.K.: 'Micro-computed tomography of fatigue microdamage in cortical bone using a barium sulfate contrast agent', Journal of the mechanical behavior of biomedical materials, 2008, 1, (1), pp. 68-75

[121]   Aguet, F., Jacob, M., and Unser, M.: 'Three-dimensional feature detection using optimal steerable filters', in Editor (Ed.)^(Eds.): 'Book Three-dimensional feature detection using optimal steerable filters' (2005, edn.), pp. II-1158

[122]   Xin, Y., Kong, L., Liu, Z., Chen, Y., Li, Y., Zhu, H., Gao, M., Hou, H., and Wang, C.: 'Machine Learning and Deep Learning Methods for Cybersecurity', IEEE Access, 2018, 6, pp. 35365-35381

[123]   Ongsulee, P.: 'Artificial intelligence, machine learning and deep learning', in Editor (Ed.)^(Eds.): 'Book Artificial intelligence, machine learning and deep learning' (2017, edn.), pp. 1-6

[124]   Levitan, I.B., Levitan, I.B., and Kaczmarek, L.K.: 'The neuron: cell and molecular biology' (Oxford University Press, USA, 2002. 2002)

[125] Chojaczyk, A.A., Teixeira, A.P., Neves, L.C., Cardoso, J.B., and Guedes Soares, C.: 'Review and application of Artificial Neural Networks models in reliability analysis of steel structures', Structural Safety, 2015, 52, pp. 78-89

[126] 'Biological neuron model', in Editor (Ed.)^(Eds.): 'Book Biological neuron model' (2022, edn.), pp.

[127] Emmert-Streib, F., Yang, Z., Feng, H., Tripathi, S., and Dehmer, M.: 'An Introductory Review of Deep Learning for Prediction Models With Big Data', Frontiers in Artificial Intelligence, 2020, 3

[128] Goodfellow, I., Bengio, Y., and Courville, A.: 'Deep learning' (MIT press, 2016. 2016)

[129] Valueva, M.V., Nagornov, N.N., Lyakhov, P.A., Valuev, G.V., and Chervyakov, N.I.: 'Application of the residue number system to reduce hardware costs of the convolutional neural network implementation', Mathematics and Computers in Simulation, 2020, 177, pp. 232-243

[130] Saha, S.: 'A Comprehensive Guide to Convolutional Neural Networks — the ELI5 way', Towards Data Science, 2018

[131] Aloysius, N., and Geetha, M.: 'A review on deep convolutional neural networks', in Editor (Ed.)^(Eds.): 'Book A review on deep convolutional neural networks' (2017, edn.), pp. 0588-0592

[132] Alzubaidi, L., Zhang, J., Humaidi, A.J., Al-Dujaili, A., Duan, Y., Al-Shamma, O., Santamaría, J., Fadhel, M.A., Al-Amidie, M., and Farhan, L.: 'Review of deep learning: concepts, CNN architectures, challenges, applications, future directions', Journal of Big Data, 2021, 8, (1), pp. 53

[133] Ahmad, E., Goyal, M., McPhee, J.S., Degens, H., and Yap, M.H.: 'Semantic segmentation of human thigh quadriceps muscle in magnetic resonance images', arXiv preprint arXiv:1801.00415, 2018

[134] Park, H., Shin, Y., Park, J., Kim, H., Lee, I.-S., Seo, D., Huh, J., Lee, T., Park, T., Lee, J., and Kim, K.: 'Development and Validation of a Deep Learning System for Segmentation of Abdominal Muscle and Fat on Computed Tomography', Korean journal of radiology, 2020, 21, pp. 88-100

[135] Piramanayagam, S., Saber, E., Schwartzkopf, W., and Koehler, F.W.: 'Supervised classification of multisensor remotely sensed images using a deep learning framework', Remote sensing, 2018, 10, (9), pp. 1429

[136] Jayanthi, P., and V. Murali Krishna, I.: '2 - A comparative study on fully convolutional networks—FCN-8, FCN-16, and FCN-32: A case of brain tumor', in Gupta, D., Kose, U., Khanna, A., and Balas, V.E. (Eds.): 'Deep Learning for Medical Applications with Unique Data' (Academic Press, 2022), pp. 19-30

[137] Piramanayagam, S., Saber, E., Schwartzkopf, W., and Koehler, F.: 'Supervised Classification of Multisensor Remotely Sensed Images Using a Deep Learning Framework', Remote Sensing, 2018, 10, pp. 1429

[138] Shelhamer, E., Long, J., and Darrell, T.: 'Fully convolutional networks for semantic segmentation', IEEE transactions on pattern analysis and machine intelligence, 2016, 39, (4), pp. 640-651

[139] Deng, J., Dong, W., Socher, R., Li, L.J., Kai, L., and Li, F.-F.: 'ImageNet: A large-scale hierarchical image database', in Editor (Ed.)^(Eds.): 'Book ImageNet: A large-scale hierarchical image database' (2009, edn.), pp. 248-255

[140] Wortsman, M., Ilharco, G., Gadre, S.Y., Roelofs, R., Gontijo-Lopes, R., Morcos, A.S., Namkoong, H., Farhadi, A., Carmon, Y., and Kornblith, S.: 'Model soups: averaging weights of multiple fine-tuned models improves accuracy without increasing inference time', arXiv preprint arXiv:2203.05482, 2022

[141]   Ding, M., Xiao, B., Codella, N., Luo, P., Wang, J., and Yuan, L.: 'DaViT: Dual Attention Vision Transformers', arXiv preprint arXiv:2204.03645, 2022

[142]   Odabai Fard, S.H.: 'Efficient multi-class objet detection with a hierarchy of classes'. Theses, Université Blaise Pascal - Clermont-Ferrand II, 2015

[143]   Sultana, F., Sufian, A., and Dutta, P.: 'A review of object detection models based on convolutional neural network', Intelligent computing: image processing based applications, 2020, pp. 1-16

[144]   Zhu, M.: 'Recall, precision and average precision', Department of Statistics and Actuarial Science, University of Waterloo, Waterloo, 2004, 2, (30), pp. 6

[145]   Torgo, L., and Ribeiro, R.: 'Precision and Recall for Regression', in Editor (Ed.)^(Eds.): 'Book Precision and Recall for Regression' (Springer Berlin Heidelberg, 2009, edn.), pp. 332-346

[146]   Henderson, P., and Ferrari, V.: 'End-to-end training of object class detectors for mean average precision', in Editor (Ed.)^(Eds.): 'Book End-to-end training of object class detectors for mean average precision' (Springer, 2016, edn.), pp. 198-213

[147]   Girshick, R., Donahue, J., Darrell, T., and Malik, J.: 'Rich feature hierarchies for accurate object detection and semantic segmentation', in Editor (Ed.)^(Eds.): 'Book Rich feature hierarchies for accurate object detection and semantic segmentation' (2014, edn.), pp. 580-587

[148]   Ren, S., He, K., Girshick, R., and Sun, J.: 'Faster r-cnn: Towards real-time object detection with region proposal networks', Advances in neural information processing systems, 2015, 28

[149]   Magalhães, R., and Peixoto, H.: 'Object Recognition Using Convolutional Neural Networks' (2019)

[150]   Redmon, J., Divvala, S., Girshick, R., and Farhadi, A.: 'You only look once: Unified, real-time object detection', in Editor (Ed.)^(Eds.): 'Book You only look once: Unified, real-time object detection' (2016, edn.), pp. 779-788

[151]   Liu, J., Yang, X., Lau, S., Wang, X., Luo, S., Lee, V.C.-S., and Ding, L.: 'Automated pavement crack detection and segmentation based on two-step convolutional neural network', Computer-Aided Civil and Infrastructure Engineering, 2020, 35, (11), pp. 1291-1305

[152]   Minaee, S., Boykov, Y.Y., Porikli, F., Plaza, A.J., Kehtarnavaz, N., and Terzopoulos, D.: 'Image segmentation using deep learning: A survey', IEEE transactions on pattern analysis and machine intelligence, 2021

[153]   Huang, Q., Sun, J., Ding, H., Wang, X., and Wang, G.: 'Robust liver vessel extraction using 3D U-Net with variant dice loss function', Computers in Biology and Medicine, 2018, 101, pp. 153-162

[154]   Ronneberger, O., Fischer, P., and Brox, T.: 'U-net: Convolutional networks for biomedical image segmentatié', in Editor (Ed.)^(Eds.): 'Book U-net: Convolutional networks for biomedical image segmentation' (Springer, 2015, edn.), pp. 234-241

[155]   Jiang, L., Xie, Y., and Ren, T.: 'A deep neural networks approach for pixel-level runway pavement crack segmentation using drone-captured images', arXiv preprint arXiv:2001.03257, 2020

[156]   Munawar, H.S., Ullah, F., Heravi, A., Thaheem, M.J., and Maqsoom, A.: 'Inspecting Buildings Using Drones and Computer Vision: A Machine Learning Approach to Detect Cracks and Damages', Drones, 2022, 6, (1), pp. 5

[157]   Liu, F., and Wang, L.: 'UNet-based model for crack detection integrating visual explanations', Construction and Building Materials, 2022, 322, pp. 126265

[158]   Wang, L., MA, X.h., and Ye, Y.: 'Computer vision-based Road Crack Detection Using an Improved I-UNet Convolutional Networks', in Editor (Ed.)^(Eds.): 'Book Computer vision-based

Road Crack Detection Using an Improved I-UNet Convolutional Networks' (2020, edn.), pp. 539-543

[159]   Zhang, L., Shen, J., and Zhu, B.: 'A research on an improved Unet-based concrete crack detection algorithm', Structural Health Monitoring, 2021, 20, (4), pp. 1864-1879

[160]   Bezerra, E.T.V., Augusto, K.S., and Paciornik, S.: 'Discrimination of pores and cracks in iron ore pellets using deep learning neural networks', REM-International Engineering Journal, 2020, 73, pp. 197-203

[161]   Shi, Y., Cui, L., Qi, Z., Meng, F., and Chen, Z.: 'Automatic road crack detection using random structured forests', IEEE Transactions on Intelligent Transportation Systems, 2016, 17, (12), pp. 3434-3445

[162]   Liu, Y., Yao, J., Lu, X., Xie, R., and Li, L.: 'DeepCrack: A deep hierarchical feature learning architecture for crack segmentation', Neurocomputing, 2019, 338, pp. 139-153

[163]   Zhang, A., Wang, K.C.P., Fei, Y., Liu, Y., Tao, S., Chen, C., Li, J.Q., and Li, B.: 'Deep Learning–Based Fully Automated Pavement Crack Detection on 3D Asphalt Surfaces with an Improved CrackNet', Journal of Computing in Civil Engineering, 2018, 32, (5), pp. 04018041

[164]   Huang, H., Zhao, S., Zhang, D., and Chen, J.: 'Deep learning-based instance segmentation of cracks from shield tunnel lining images', Structure and Infrastructure Engineering, 2022, 18, (2), pp. 183-196

[165]   Chen, K., Reichard, G., Xu, X., and Akanmu, A.: 'Automated crack segmentation in close-range building façade inspection images using deep learning techniques', Journal of Building Engineering, 2021, 43, pp. 102913

[166]   Xiao, C., and Buffiere, J.-Y.: 'Neural network segmentation methods for fatigue crack images obtained with X-ray tomography', Engineering Fracture Mechanics, 2021, 252, pp. 107823

[167]   Hong, L., Zhang, P., Liu, D., Gao, P., Zhan, B., Yu, Q., and Sun, L.: 'Effective segmentation of short fibers in glass fiber reinforced concrete's X-ray images using deep learning technology', Materials & Design, 2021, 210, pp. 110024

[168]   Turunen, M.J., Le Cann, S., Tudisco, E., Lovric, G., Patera, A., Hall, S.A., and Isaksson, H.: 'Sub-trabecular strain evolution in human trabecular bone', Scientific Reports, 2020, 10, (1), pp. 13788

[169]   Peters, W., and Ranson, W.: 'Digital imaging techniques in experimental stress analysis', Optical engineering, 1982, 21, (3), pp. 427-431

[170]   Sutton, M.A., Wolters, W.J., Peters, W.H., Ranson, W.F., and McNeill, S.R.: 'Determination of displacements using an improved digital correlation method', Image and Vision Computing, 1983, 1, (3), pp. 133-139

[171]   Mobasher, B.: '5 - Textile fiber composites: Testing and mechanical behavior', in Triantafillou, T. (Ed.): 'Textile Fibre Composites in Civil Engineering' (Woodhead Publishing, 2016), pp. 101-150

[172]   Rankin, K., Steer, J., Paton, J., Mavrogordato, M., Marter, A., Worsley, P., Browne, M., and Dickinson, A.: 'Developing an Analogue Residual Limb for Comparative DVC Analysis of Transtibial Prosthetic Socket Designs', Materials (Basel, Switzerland), 2020, 13

[173]   McCormick, N., and Lord, J.: 'Digital Image Correlation', Materials Today, 2010, 13, (12), pp. 52-54

[174]   Peña Fernández, M., Black, C., Dawson, J., Gibbs, D., Kanczler, J., Oreffo, R.O., and Tozzi, G.: 'Exploratory full-field strain analysis of regenerated bone tissue from osteoinductive biomaterials', Materials, 2020, 13, (1), pp. 168

[175]   Hussein, A.I., and Morgan, E.F.: 'Direct visualization of the initiation and progression of vertebral fractures', in Editor (Ed.)^(Eds.): 'Book Direct visualization of the initiation and progression of vertebral fractures' (American Society of Mechanical Engineers, 2010, edn.), pp. 509-510

[176]   Madi, K., Staines, K.A., Bay, B.K., Javaheri, B., Geng, H., Bodey, A.J., Cartmell, S., Pitsillides, A.A., and Lee, P.D.: 'In situ characterization of nanoscale strains in loaded whole joints via synchrotron X-ray tomography', Nature biomedical engineering, 2020, 4, (3), pp. 343-354

[177]   Peña Fernández, M., Cipiccia, S., Dall'Ara, E., Bodey, A.J., Parwani, R., Pani, M., Blunn, G.W., Barber, A.H., and Tozzi, G.: 'Effect of SR-microCT radiation on the mechanical integrity of trabecular bone using in situ mechanical testing and digital volume correlation', Journal of the Mechanical Behavior of Biomedical Materials, 2018, 88, pp. 109-119

[178]   Tozzi, G., Danesi, V., Palanca, M., and Cristofolini, L.: 'Elastic Full-Field Strain Analysis and Microdamage Progression in the Vertebral Body from Digital Volume Correlation', Strain, 2016, 52, (5), pp. 446-455

[179]   Kogawa, M., Khalid, K.A., Wijenayaka, A.R., Ormsby, R.T., Evdokiou, A., Anderson, P.H., Findlay, D.M., and Atkins, G.J.: 'Recombinant sclerostin antagonizes effects of ex vivo mechanical loading in trabecular bone and increases osteocyte lacunar size', Am J Physiol Cell Physiol, 2018, 314, (1), pp. C53-C61

[180]   Bar-Kochba, E., Toyjanova, J., Andrews, E., Kim, K.S., and Franck, C.: 'A Fast Iterative Digital Volume Correlation Algorithm for Large Deformations', Experimental Mechanics, 2015, 55, (1), pp. 261-274

[181]   Fíla, T., Kytýř, D., Zlámal, P., Kumpová, I., Doktor, T., Koudelka, P., and Jiroušek, O.: 'High-resolution time-lapse tomography of rat vertebrae during compressive loading: deformation response analysis', Journal of Instrumentation, 2014, 9, (05), pp. C05054-C05054

[181]   Zhao, H.-l., Qin, G., and Wang, X.-j.: 'Improvement of canny algorithm based on pavement edge detection', 2010 3rd International Congress on Image and Signal Processing, 2010, 2, pp. 964-967

[182]   Sun, C., Shrivastava, A., Singh, S., and Gupta, A.: 'Revisiting unreasonable effectiveness of data in deep learning era', in Editor (Ed.)^(Eds.): 'Book Revisiting unreasonable effectiveness of data in deep learning era' (2017, edn.), pp. 843-852

[183]   Fíla, T., Kytýř, D., Zlámal, P., Kumpová, I., Doktor, T., Koudelka, P., and Jiroušek, O.: 'High-resolution time-lapse tomography of rat vertebrae during compressive loading: deformation response analysis', Journal of Instrumentation, 2014, 9, (05), pp. C05054-C05054